2007-03-14

A High-Resolution Microscopic Electrical Impedance Imaging Modality: Scanning Impedance Imaging

Hongze Liu
Brigham Young University - Provo

A HIGH-RESOLUTION MICROSCOPIC ELECTRICAL IMPEDANCE IMAGING MODALITY: SCANNING IMPEDANCE IMAGING

by

Hongze Liu

A dissertation submitted to the faculty of

Brigham Young University

in partial fulfillment of the requirements for the degree of

Doctor of Philosophy

Department of Electrical and Computer Engineering

Brigham Young University

April 2007

BRIGHAM YOUNG UNIVERSITY

GRADUATE COMMITTEE APPROVAL

of a dissertation submitted by

Hongze Liu

This dissertation has been read by each member of the following graduate committee and by majority vote has been found to be satisfactory.

Date	Travis E. Oliphant, Chair
Date	Aaron R. Hawkins
Date	Stephen M. Schultz
Date	Dah-Jye Lee
Date	Brian D. Jeffs

BRIGHAM YOUNG UNIVERSITY

As chair of the candidate's graduate committee, I have read the dissertation of Hongze Liu in its final form and have found that (1) its format, citations, and bibliographical style are consistent and acceptable and fulfill university and department style requirements; (2) its illustrative materials including figures, tables, and charts are in place; and (3) the final manuscript is satisfactory to the graduate committee and is ready for submission to the university library.

Date

Travis E. Oliphant
Chair, Graduate Committee

Accepted for the Department

Michael Wirthlin
Graduate Coordinator

Accepted for the College

Alan R. Parkinson
Dean, Ira A. Fulton College of
Engineering and Technology

ABSTRACT

A HIGH-RESOLUTION MICROSCOPIC ELECTRICAL IMPEDANCE IMAGING MODALITY: SCANNING IMPEDANCE IMAGING

Hongze Liu

Department of Electrical and Computer Engineering

Doctor of Philosophy

Electrical impedance imaging is an imaging technique which has the capability of revealing the spatial distribution of the electrical impedance inside biological tissues. Classical electrical impedance imaging including Electrical Impedance Tomography (EIT) typically has low resolution. Advances in electrical impedance imaging typically involve methods that either increase image resolution or image contrast. This study investigates the possibility of the resolution improvement for electrical impedance imaging using motion, and presents a novel high-resolution and calibrated impedance imaging method called Scanning electrical Impedance Imaging (SII). SII uses an electrical probe held at a known voltage and scanned over a thin sample immersed in a conductive medium on a grounded conducting plane to obtain high-resolution calibrated impedance images of samples.

For system improvement and image reconstruction, a numerical model is developed to describe the SII system. This model simulates the measurement process by solving a 3-D electrostatic field at each scanning position using a modified approach

of the finite difference method (FDM). The simulation consists of a quasi-statics problem involving inhomogeneous media with a complicated boundary condition. This 3-D model is used to optimize both the probe height and the shield-spacing for probe fabrication and also to evaluate system parameters including the frequency and the resistor in the peripheral circuit. Based on this model, an approach is also developed to quantifying conductivity values using the SII system. However, a large computational cost due to the motion involved in SII leads to challenges for a fast and accurate image reconstruction based on this 3-D model.

Alternative fast models are derived as a replacement of the 3-D model for quick image reconstruction. In particular, the Modified Linear Approximation (MLA) involving two conductivity-weighted convolutions based on the reciprocity principle, explains the function of the special shield design introduced in the SII system reasonably well. Based on the MLA a nonlinear inverse method using total variation regularization and the Polak-Ribiére variant of the nonlinear conjugate-gradient method is developed for fast image reconstruction of the SII system. The inverse method is accelerated using convolution which eliminates the requirement of a numerical solver for the 3-D electrostatic field. 2-D images of small biological tissues and cells are measured using the SII system. The corresponding conductivity images are reconstructed using the MLA method. The successful improvement of resolution shown in both simulation and experimental results demonstrates that the idea of this approach can potentially be expanded to other imaging modalities for resolution improvement using motion.

ACKNOWLEDGMENTS

I would like to express my sincerest appreciation to my advisor, Dr. Travis Oliphant, for his support and guidance throughout the past four years. He has been a great mentor, teaching me about research and life. I am indebted to him for all his guidance and assistance. This work would not have been possible without his help and instruction, and I am truly grateful. I am also thankful to all of my committee members: Dr. Aaron Hawkins for his support, Dr. Stephen Schultz for his assistance, Dr. Dah-Jye Lee for his encouragement and understanding, and Dr. Brian Jeffs for his help. I also appreciate all the other professors who have helped me in my study and research.

Many thanks to all my colleagues for their advice and friendship. I am also grateful to my friends for their emotional support and inspiration. And finally, my special gratitude goes to my family in China. There are not enough words to express my appreciation to them. I want to thank my mother, father and sister for their endless love and support.

Table of Contents

List of Tables

List of Figures

Chapter 1

Introduction

1.1 General background

The evolution of science often parallels the invention of instruments that extend human senses to new limits. Although cells were first discovered by Robert Hooke in 1665, the geography of the cell was largely uncharted until the past few decades as microscopic imaging techniques has become commonplace. By using microscopes, these techniques provide us a way to view the microscopic world of the fundamental units (cells) that make up all living organisms. Microscopes can largely be separated into two classes, optical microscopes and scanning probe microscopes. Optical microscopes are microscopes which function through the optical theory of lenses in order to magnify the image generated by the passage of a wave through the sample. The waves used are either electromagnetic in optical microscopes or electron beams in electron microscopes. The types of microscopes are the compound light, stereo, and the electron microscope. The most common type of microscope-and the first to be invented-is the optical microscope. Based on it, the optical microscopy is a high-frequency far field imaging method with very small wavelength. The ob-

served structures are much larger than the wavelength used in experiments. Optical microscopy has proven to be very useful to image the cell anatomy with very high resolution.

Beyond the curiosity of cell anatomy, cell function is another important property of a cell. Unlike cell anatomy, cell function is not a structure that can be imaged; however, it can be observed by imaging the protein shape and the interaction and exchange of ions because we now know that cell function relies heavily on these two. In fact, life is literally teeming with polar molecules (water), inhomogeneous charge distributions (DNA, proteins), and ions (H^+, K^+, Na^+, Cl^-). The alteration of ion concentrations, charge distributions (e.g. during enzymatic activity), and polarizability of water (i.e. protein hydration state) are all natural, inherent markers of cellular function. In other words, the cell function can be revealed by imaging these markers. However, as a high-frequency far field imaging modality, conventional optical microscopy does not provide the ability to image these markers.

Both cell anatomy and the function are the objectives of imaging biological cells. The advent of the optical microscope allowed great advances in the first of these two objectives. Simply describing the diverse organelles within the cells aided greatly to our overall understanding of the biological organization, but revealed little about their function. Consequently, current medicine focus on the structure of the cell but has a more difficult job in determining cell function. However, cell function plays an important role in the biological world. A advancement that takes into account these ionic and electrical properties could enhance the ability to understand cell function. Cell function could potentially be visualized dynamically if high-resolution (in both time and space) images of electrical properties of matter could be made.

Electrical impedance imaging is a near-field modality that has potential to visualize the electrical properties in an object by measuring electrical response on the surface. The impedance information could reveal information about ion concentrations and their distributions, and even charge distribution, etc. Ideally, this technique could be applied throughout a cellular volume. Although measuring information about the electrical properties within living cells holds endless possibilities for advancing biology, an effective method for doing this has not yet been fully developed. Some methods such as electrical impedance tomography have obtained crude images of biological tissues based on electrical properties, but with nowhere near the resolution required to explore individual cells. This thesis explores a new method of electrical impedance imaging called Scanning Impedance Imaging (SII) that has vastly improved resolutions close to the cellular scale. At the current stage, the targets of scanning impedance imaging focus on the concentrations of ions although it has the potential to image all the electrical properties including charge distributions for protein shapes.

1.2 General concepts and methods

Electrical impedance imaging is a non-invasive imaging modality that estimates the electrical properties at the interior of an object from measurements made on its surface. Typically, currents are generated within the objects, and the resulting effects are measured. There are several ways to produce currents inside the objects. One possible approach is direct current injection using electrodes placed on the surface. Measurements can also be obtained using electrical probes on the surface. Based

on the measurements, the impedance distribution can be reconstructed everywhere in the object. This idea is illustrated in Figure 1.1

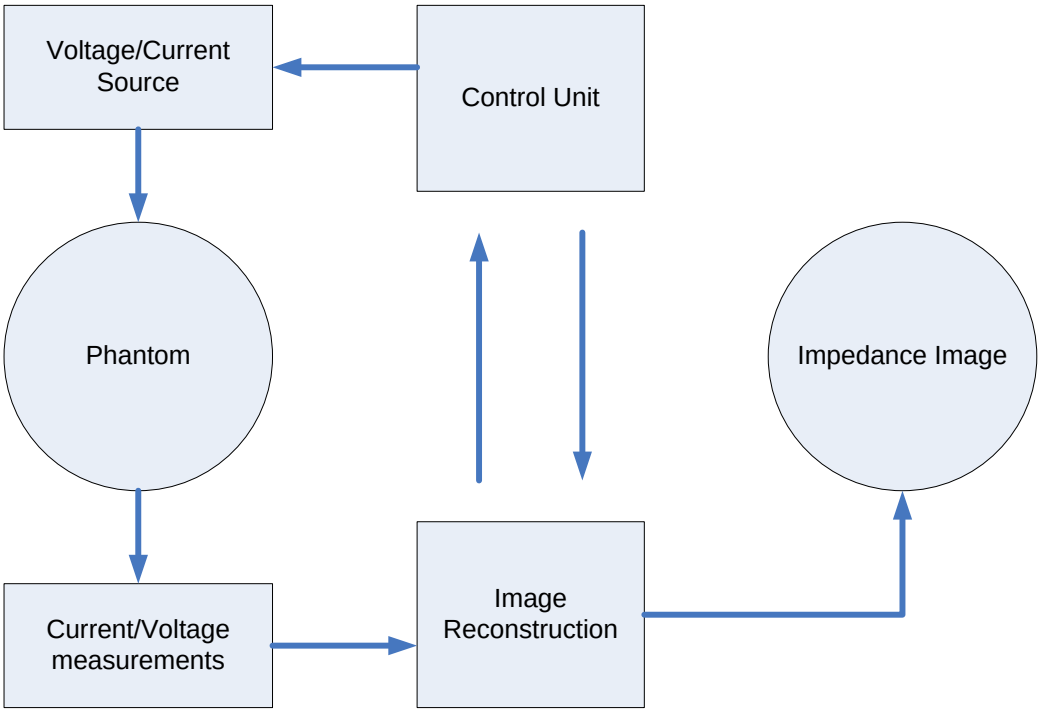

Figure 1.1: General Electrical Impedance Imaging System

In the literature, this basic idea is implemented in limited ways. Most studies apply tomographic reconstruction calling the modality Electrical Impedance Tomography (EIT). In EIT, electrodes are placed around an object forming a ring with two for current injection and voltages are measured on the other electrodes. Recently, measurements are sometimes collected using Magnetic Resonance (MR), which is called MR-EIT. In this work, a different approach is developed using a high-resolution scanning technique. Even though based on the same general idea, the new approach uses motion to produce the measurements which requires different image reconstruction from tomography.

1.3 Significance and clinical applications

Although currently the resolution of the technology proposed in this thesis is not high enough to image a single cell, the successful construction and use of this technology would potentially lead to a new imaging tool that could greatly expand the information scientists can obtain about cellular structure and function. By providing rapid two-dimensional information regarding the conductivity and dielectric permeability of cell samples, greatly improved understanding of cellular processes could be obtained. For example, a high-resolution conductivity image could show the direction and orientation of nano-tubes used for intra-cellular trafficking as well as average activity of ion channels in the cell membrane. An image of dielectric permeability could show protein folding activity as well as reveal the average rotational mobility of water molecules in different regions of the cell during different physiological processes. The nature of the proposed technique enables the monitoring of in-vitro biochemical processes and therapeutic action of pharmaceutical agents.

In addition to the scientific applications, electrical impedance at multiple frequencies has already shown clinical utility in distinguishing between active and inactive white blood cells [1]. In addition, cancerous tissue has already been shown to have an increased conductivity. As a result, an example application of the device to biopsy samples could assist the pathologist in distinguishing between malignant and benign neoplastic growth. While some of the scientific applications are admittedly ambitious, successful clinical applications would require far less resolution than will be shown in this thesis.

1.4 Thesis objectives

The primary aim of this study is the design of a microscopic electrical impedance imaging system that applies electrical impedance imaging to small tissues and even cells. It has the potential to image cells or a single cell with sufficient resolution at different frequencies. The imaging system consists of a micro-scale measuring instrument and a reconstruction process to create an image of the impedance of a sample from the measurements based on physical modeling. In this thesis, a feasible design of microscopic electrical impedance imaging that could be applied to cellular level measurements: scanning impedance imaging (SII) is developed, modeled, and tested. SII uses a non-contact electrical probe held at a known voltage and scanned in tiny steps over a thin sample in a conductive aqueous medium.

1.5 Contributions

The major contributions of this thesis are system design, modeling work and image reconstruction of the novel scanning electrical impedance imaging modality. The specific contributions of this thesis can be outlines as follows:

- Design and development of the scanning impedance imaging system using a novel shielded impedance probe with a coaxial geometry and liquid-contact configuration for the connection between the probe and the sample[2, 3, 4, 5]
- Development and implementation of the experimental setup of the scanning impedance imaging system

- Development of the LabView programs for the scanning stage control, function generator control and data acquisition using ADC card and lock-in amplifier
- Test and debugging of the whole experimental system
- Experiments of line-scans and 2d image scans for both artificial samples of composite material and biological samples including leaves, flower petals, cells etc.
- Experiments of system performance: resolution and signal-to-noise ratio for comparison of unshielded probes and shielded probes.
- Explanation and formulation of the electromagnetic field problem in the region of interest for the electrical impedance imaging, especially for the scanning impedance imaging with hypotheses of low frequency, low contribution of magnetic field, and complex combination of conductivity and permittivity[6]
- 2-D modeling of the electrical impedance tomography and the scanning impedance imaging using MATLAB partial differential equation (pde) toolbox
- Development and verification of a 3-D finite difference model for the scanning impedance imaging using a half-shifted mesh of a 7-point cubic structure[7, 8]
- Prediction and optimization of both the probe design and system parameters using the 3-D finite difference model
- System performance analysis including resolution, signal-to-noise ratio and etc using the 3-D finite difference model
- Impedance quantification of the scanning impedance imaging using the 3-D finite difference model for both the artificial and biological samples[9]

- Development of 2-D fast alternative models based on the reciprocity principle and convolution for the scanning impedance imaging[10]
- Development of a fast nonlinear 2-D Image reconstruction of scanning impedance imaging based on the Modified Linear Approximation (MLA) model using the Polak-Ribiére variant of the nonlinear conjugate-gradient method[11]
- Comparison and performance analysis of 2-D and 3-D models for image reconstruction of the scanning impedance imaging
- Implementation and experimental data reconstruction using the 2-D MLA method for different biological samples

Chapter 2

Related work

The ultimate objective of this thesis is to image the electrical properties including charge distribution and ions inside a single cell. This study involves two main areas: cellular imaging and electrical impedance imaging. The design of the scanning impedance imaging benefits from previous studies in both areas. This chapter will go through the literature in the cellular imaging area first and then review the electrical impedance imaging. For imaging cells, microscopes of different types are employed in order to view the microscopic world inside cells. The key challenge of the cellular imaging is the high resolution. However, current electrical impedance imaging targets big tissues or human bodies due to its low resolution. The scanning impedance imaging in this study solves this problem by introducing high resolution scanning techniques and indirect contact configuration. Because the scanning impedance imaging is a low-frequency near field imaging modality, the image reconstruction is a complex inverse problem. Thus, popular approaches of inverse problem are also shown in this chapter.

2.1 Cellular imaging

Currently, cellular studies are limited by the ability of microscopes and markers such as dyes that allow scientists to visualize the contents and structure of the cell. However, cells are literally teeming with polar molecules (water), inhomogeneous charge distributions (DNA, proteins), and ions (H^+, K^+, Na^+, Cl^-). Table 2.1 shows ion concentrations of the intracellular liquid (ICL) [12]. The alteration of ion concentrations, charge distributions (e.g. during enzymatic activity), and polarizability of water (i.e. protein hydration state) are all natural, inherent markers of cellular function. The electrical activity of these markers in living cells is responsible for much of the complex behavior of organisms. Sensory processing, cardiac function, muscle control, thought, etc. are all partially controlled and regulated by this electrical activity and response of different cells in the body. Even though there are a plethora of different cell types, the fundamental mechanisms for electrical activity are quite similar. Structurally, cells are composed of a lipid bilayer membrane enclosing an intracellular ionic solution. This membrane contains numerous proteins, receptors, ionic channels, and ionic pumps which are responsible for maintaining the ionic concentrations within the cell and the intracellular potential relative to the extracellular. Thus, cellular anatomy and function could be potentially visualized dynamically if high-resolution (in both time and space) images of electrical properties of matter could be made at appropriate frequencies. Among electrical properties, electrical impedance consisting of conductivity and permittivity is a good essential indicator for the inner electrical status of cellular contents.

There are several nano-scale imaging modalities using the scanning probe microscopy including the well-known atomic force microscopy (AFM) [13, 14], etc. These

Table 2.1: The ion concentrations of the intracellular liquid (ICL)

Ions	ICL (mM)
K^+	125
Na^+	12
Cl^-	5
$A^{-1.223}$ (organic anions)	108
H_2O	55000

standard nano-scale imaging techniques are used to produce surface profiles and have been applied to the area of cellular imaging.

The atomic force microscope is one of about two dozen types of scanned-proximity probe microscopes. All of these microscopes work by measuring a local property - such as height, optical absorption, or magnetism - with a probe or "tip" placed very close to the sample. Figure 2.1 shows the concept of a typical AFM. The small probe-sample separation (on the order of the instrument's resolution) makes it possible to take measurements over a small area. To acquire an image the microscope raster-scans the probe over the sample while measuring the local property in question. The resulting image resembles an image on a television screen in that both consist of many rows or lines of information placed one above the other. Pioneering work and instrumental development of AFM were carried out by the groups of Paul Hansma, University of California, Santa Barbara; and Gerd Binnig, IBM Physics, Munich. Meanwhile, many other groups contributed exciting new insights at the cellular and molecular levels using the AFM. The essential part of an AFM, as for all scanning probe microscopes, is the tip that determines by its structure the type of interaction with a surface; and by its geometry, the area of interaction. The original idea for the AFM was to measure the van der Waals interaction of an atom at the very end of the tip with atoms at a surface of a solid substrate. To bring a single atom at a tip

close to within angstrom distance toward a surface is only possible if the surface is atomically flat, such as, for example, the crystalline surface of mica. The ability of AFM to image at atomic resolution, combined with its ability to image a wide variety of samples under a wide variety of conditions, has created a great deal of interest in applying it to the study of biological structures. For the first time, in 1989, Binnig visualized the process of pox virus release on living cells. Images have appeared in the literature showing DNA, single proteins, structures such as gap junctions, and living cells (for a review see Hoh and Hansma, 1992). Unfortunately, AFM cannot image all samples at atomic resolution. The end radii of available tips confines atomic resolution to flat, periodic samples such as graphite. In addition, because biological structures are soft, the tip-sample interaction tends to distort or destroy them.

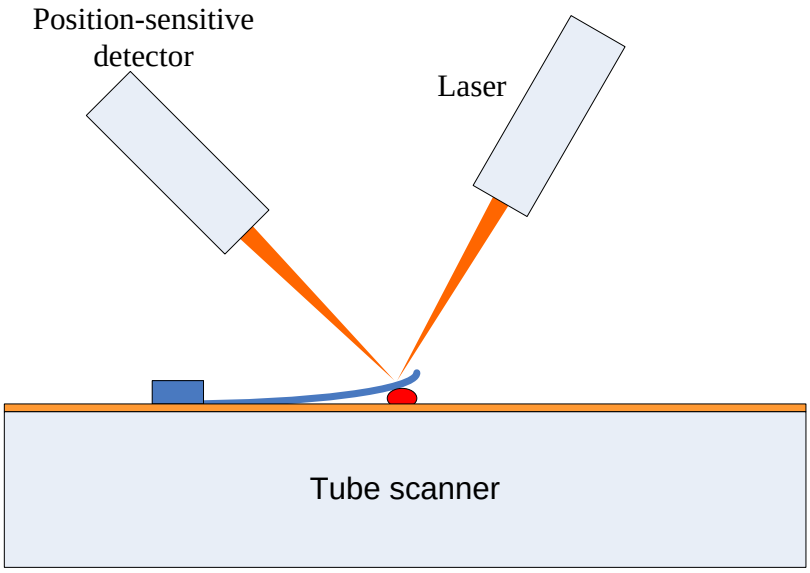

Figure 2.1: Concept of AFM and the optical lever. Scale drawing; the tube scanner measures 24 mm in diameter, while the cantilever is 100 μm long.

Even though these high resolution imaging methods have proved to be very advantageous to biology, they do not use the natural contrast that exists in the elec-

trical properties of biological material. Further, the resolution is too high to image big shapes of proteins or ion concentrations. Thus, it is hardly feasible to obtain an image of detailed electrical information using these surface imaging modalities. However, these methods provide a way into high-resolution imaging using high-resolution scanning techniques and micro-(nano-)probes.

2.2 Electrical impedance measurements

2.2.1 Impedance measurements of biological tissues

As early as the 1900s, scientists and researchers have shown the interest in measuring electrical impedance of tissues within the human body. Galeotti in 1902 was probably the first to note the changes in resistivity which accompany the death of cells[15]. In freshly excised tissues he observed an initial increase followed by a considerable decrease in resistivity. In 1967, Geddes and Baker reported the specific resistance of biological tissues including body fluids, blood, cardiac muscle, skeletal muscle, lung, kidney, liver, spleen, pancreas, nerve tissue, fat, and bone, nearly covering all the main organs within human body[16]. It has also been shown that electrical properties of malignant tissues are significantly different from those of normal and benign tissues. Surowiec et al. have reported that the electrical resistance of malignant tumors decreases by a factor of 20 to 40 with respect to normal or benign tissues [17]. It is therefore hoped that such information may be used in tumor detection and diagnosis by means of the spatial distribution of conductivity measurements (inversely related to resistance). It is also clear that such information may be used in conjunction with other imaging modalities to identify tumors and achieve higher

specificity rates, compared with current techniques. To exploit this finding, scientists have reported several methods that can reveal the conductivity information inside tissues, which will be discussed in Section 2.3.

2.2.2 Impedance measurements of cells

As early as 1923, Grant found that cancer cells have a lower resistivity that normal cells at low frequency [18]. Since then, scientists have shown their interest in cellular resistivity besides the interest in tissue resistivity. In 1981, Hause, et al. proposed impedance measurement for bacterial growth monitoring [19].

Giaever was the first to monitor the impedance of populations (20 to 80) of cultured cell using electrodes significantly larger than the cells to be studied. In 1984 he described a system where standard polystyrene tissue culture dishes were modified to include a large reference electrode (2 cm^2) and 4 smaller electrodes ($3\times cm^2$) [20]. Giaever and Keese cultured human lung fibroblasts (WI-38 and WI-38/VA-13) cells on the modified cell culture dishes and applied an AC voltage through a resistor to a single small electrode in the dish. The result was a near constant current source which enabled the impedance to be determined by measurement of the resulting voltage. Using a lock-in amplifier, they were able to observe the effects of cell proliferation (impedance increase) as well as micro-motion of the cells (fluctuations in observed impedance). This was the first demonstration of a system capable of monitoring proliferation and motion of a population of cells cultured *in vitro*. Giaever and Keese continued their work in the years that followed, examining the effects of different proteins on cell adhesion, spreading, and motility [21]. Giaever, et al. also showed this impedance technique was capable of resolving cellular movement at the nanome-

ter level, something which previously was impossible using conventional time lapse microscopy [22].

Recently, impedance studies of anchorage dependent cultured cells have been performed by three other groups using different electrode structures. In 1995 Hagedorn, et al. utilized a perforated silicon membrane structure to examine the motion of fibroblasts cultured on the surface [23]. The upper and lower electrolytes were separated by the silicon membrane so that current flowing from the upper electrode to the lower electrode passed through the pore. Given large electrodes, the 10-micron diameter pore could be made to dominate the measured impedance. In 1996, Wegener, et al. described an electrode system similar to that of Giaever, et al. which utilized a voltage divider technique for determination of the unknown impedance across a range of frequencies (1 Hz to 10 kHz) [24]. In 1997, Ehret, et al. described an interdigitated electrode structure with electrodes of 50 micron in width separated by 50 micron in a 5 mm $\times$ 5 mm active area [25].

The development of a cellular imaging system that allows the measurement of impedance across the cell will provide important information for monitoring cell activation and valuable cellular mechanisms and increasing our understanding of the internal electrical structure of the cell. However, there are few projects proposed in the literature which attempt to obtain an image of the impedance distribution of cells, even though many studies reported different approaches to measure the electrical impedance. The current electrical impedance imaging is limited by its low resolution and is not able to be used in cellular imaging. The history and detail of this technique that motivate the basic idea of the new scanning impedance imaging modality will be discussed in the following section.

2.3 Electrical impedance imaging

In 1895, Roentgen's discovery of X rays flung open a door that led to a new dimension in the medicine–the ability to look within a patient's body without having to slice it open. After these initial advances, medical imaging evolved steadily but slowly until the 1970s. Driven largely by the availability of powerful computers, several medical imaging modalities have rapidly altered patient diagnosis and treatment in the past few decades. Computed tomography (CT), magnetic resonance imaging (MRI), ultrasound and positron emission tomography (PET) have all changed the ways in which physicians practice their art.

In 1978, Henderson and Webster designed and built an impedance camera to generate electrical impedance images of the thorax[26]. The instrument makes 100 spatially specific admittance measurements per frame at rates up to 32 frames per second. They used this camera to study pulmonary edema. They applied a 100KHz AC voltage signal to a large electrode on the chest, and measured the current through an array of 100 small electrodes on the opposite side using a single channel. However, the assumption they made was not valid because they assumed electric currents traveled in straight lines, which is not true. This work was probably the first attempt at electrical impedance imaging. Since then, many studies have been focused on the area of electrical impedance imaging, and many feasible approaches have been proposed including electrical impedance tomography, magnetic resonance electrical impedance tomography, and magnetic induction tomography.

Electrical impedance measurements of tissues or cells in the previous section are measures of a whole object. The electrical impedance Z is a complex number

$$Z = R + jX, \tag{2.1}$$

where R is the electrical resistance and X is the electrical reactance. It can be seen that the electrical impedance Z is an integral measure that is not applicable for imaging. In the electrical impedance imaging, an image of the ability to conduct an electric current needs to be measured for the material inside an object. Thus, the electrical properties measured in the electrical impedance imaging are conductivity σ and permittivity ϵ. The conductivity is defined as the ratio of the current density J to the electric field E:

$$J = \sigma E. \tag{2.2}$$

The permittivity is defined as the ratio of the electric displacement field D to the electric field E:

$$D = \epsilon E. \tag{2.3}$$

Both σ and ϵ are measures of materials and may vary inside the object. For a regular conductor and a parallel-plate capacitor of homogeneous materials (σ and ϵ are constant), there is an explicit relationship between the electrical impedance Z and σ and ϵ. The electrical resistance is

$$R = \frac{L}{\sigma A}, \tag{2.4}$$

where L is the length of the conductor and A is the cross-sectional area. The electrical capacitance is

$$C = \frac{\epsilon A}{d}, \tag{2.5}$$

where A is the area covered by the capacitor, and d is the distance between the plates. Thus, the electrical impedance Z can be obtained as

$$Z = R + \frac{1}{j\omega C}. \tag{2.6}$$

There are several methods reported in the literature which image the electrical impedance in an object. Among them, the most popular modality is Electrical Impedance Tomography (EIT) that involves the tomographic reconstruction. In the electrical impedance imaging, most literature work focused on EIT in both hardware design and image reconstruction.

2.3.1 Electrical impedance tomography

In 1983, Barber and Brown suggested the first system of electrical impedance tomography that produced a tomographic image using electrical resistivity[27]. Their system used measurements of voltage difference on the periphery of the region to be imaged, and used the backprojection method for image reconstruction. There were 16 electrodes placed in a plane around an object. The Applied Potential Tomography (APT) they proposed sequentially applied electrical currents to the body using a pair of opposite electrodes. While current was flowing, voltages between adjacent noncurrent-carrying electrodes were measured. In 1987, Brown and Seagar reported

on a practical system they built. They called this setup the Sheffield scheme and it is now the most widely used electrode configuration for current injection and measurement in conventional EIT[28]. In the same year, Kim and Woo proposed a similar system except that they applied a constant voltage source instead of current injection and measured currents on the surface. A typical EIT system is shown in Figure 2.2.

Besides APT, adaptive current tomography (ACT) was suggested as an alternative type of EIT system[29, 30]. In an ACT system, currents are simultaneously applied to all electrodes while voltages on each electrode are measured. For a N-electrode system, N-1 linearly independent current patterns are applied to the object and the electrode voltages are measured. One advantage of the ACT system is the ability to make static images, i.e., estimates of the absolute impedance, as well as dynamic images which show only changes in impedance. In addition, it has been shown both analytically and experimentally that an ACT system produces greater distinguishability [31, 32] than an APT system, meaning that, for a given amount of applied power, larger electrode voltage changes are produced for a given change in impedance within the object [29, 33]. Experimental results verifying this property are provided in [29]. Also, the distinguishability in ACT systems improves with an increase in the number of electrodes in contrast to APT systems in which distinguishability decreases with a larger number of electrodes[29]. Due to limited precision in measuring these voltages, improved distinguishability corresponds to the ability to detect smaller impedance variations within the object, effectively providing greater resolution. The disadvantage of ACT-type systems is increased hardware complexity, since they require a current source for each electrode rather than a single source driving one pair of electrodes at a time.

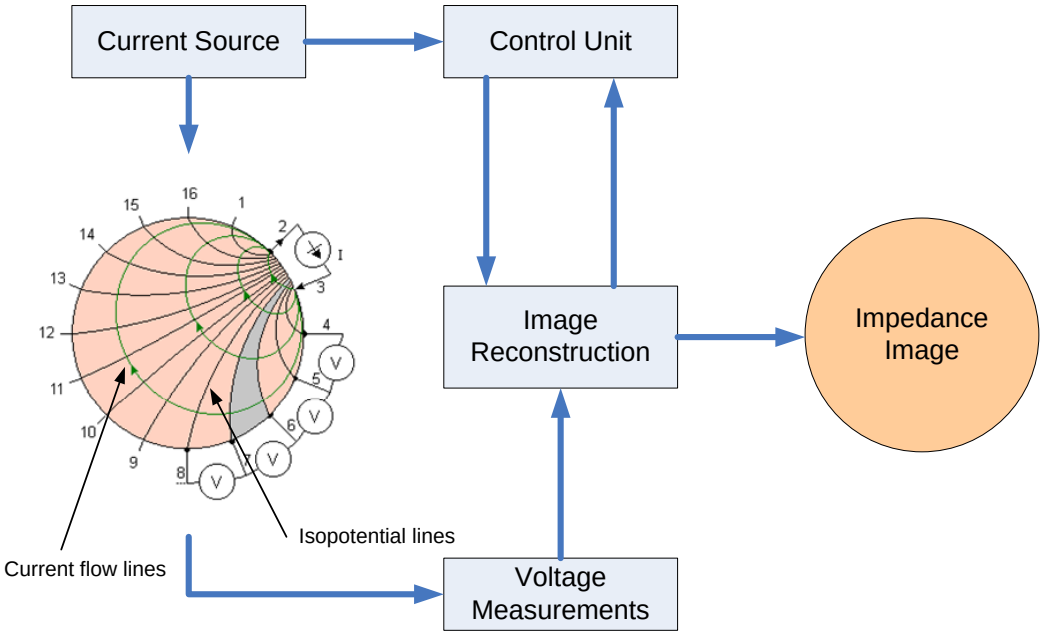

(a)

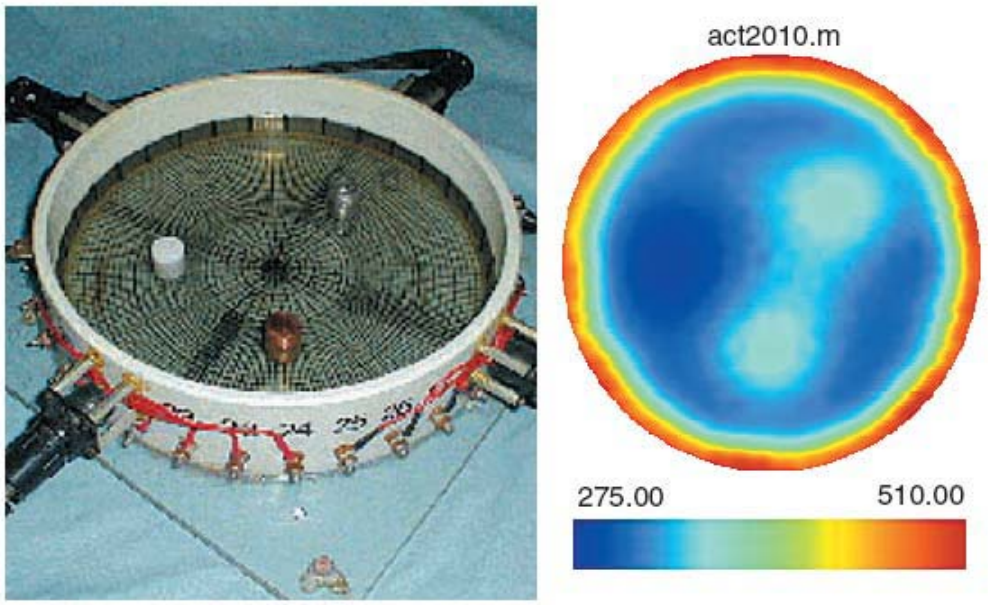

(b)

Figure 2.2: Electrical Impedance Tomography
(a) Diagram of a typical EIT system. (b) A real phantom tank and static impedance image with an insulator and two metal objects in a saline bath.

The measurement system of EIT usually has 8, 16, 32 or even 64, 128 electrodes, however, due to space and interference condition and data collection limitation, it is nearly impossible to have more than 256 electrodes in an EIT system. Thus, the number of independent measurements is limited and therefore the resolution is low. This will be further discussed in the following section. EIT introduces minimal electrical risk to the patient, since it uses a low frequency AC signal and the amplitude of the source signal is very low. Because no radiation nor dyes are required, EIT system can be used for long term monitoring of a patient or analysis of biological tissues *in vivo*.

2.3.2 Other approaches

Many researchers put efforts into integrating EIT with other techniques such as Current Density Imaging (CDI) . CDI uses Magnetic Resonance Imaging (MRI) techniques to measure the magnetic flux density generated by the current density distribution within an object. Thus, it can reconstruct the interior current density without placing electrodes on the surface. By combining CDI and EIT, Magnetic Resonance Electrical Impedance Tomography (MREIT) has been emerging as a new conductivity imaging modality [34]. MR-EIT uses the magnetic flux density measurements acquired from MR phase images to reconstruct conductivity distribution. Magnetic flux density generated by applied currents can be measured with high spatial resolution using MRI. It should be noted that only the component of the magnetic flux density in the direction of the main field of the MRI system can be measured. Therefore, a reconstruction technique must be developed in order to solve the inverse problem of finding the conductivity or current density from only one component of

magnetic flux density. In 2002, Kwon *et al* proposed the J-substitution algorithm and presented simulation results [35].

Another related technique is Magnetic Induction Tomography (MIT). MIT applies a magnetic field from an excitation coil to induce eddy currents in the material and the magnetic field from these is then detected by sensing coils. The technique has been variously named mutual inductance tomography (also MIT) and electromagnetic tomography (EMT). MIT is sensitive to all three passive electromagnetic properties: conductivity, permittivity and permeability. The development of MIT for biomedical use presents formidable difficulties because the conductivities of biological tissues are many orders of magnitude lower than those of metals and they have no appreciable permeability above that of free space. This means that the secondary signals to be measured are very weak. These difficulties might also be experienced in industrial applications involving the imaging of ionized water. The first report of MIT for biomedical use was by Al-Zeibak and Saunders [36]. An excitation and a sensing coil operating at 2 MHz were scanned past a tank of tissue equivalent saline solution, with immersed metallic objects, in a translate-rotate manner. Images were reconstructed by filtered backprojection and showed the outline of the tank and the internal features.

Recently, interest in electrical impedance measurements on a smaller scale for *in-vitro* work has been receiving some attention. For example, Lacy, et. al have developed a cellular impedance spectroscopy device which can detect *in-vitro* the activated state of eosinophils (white blood cells involved in the asthma response) [1]. Using micro-fabricated electrodes these researchers have shown differences in the impedance spectrum of activated and non-activated eosinophil cells. In a related

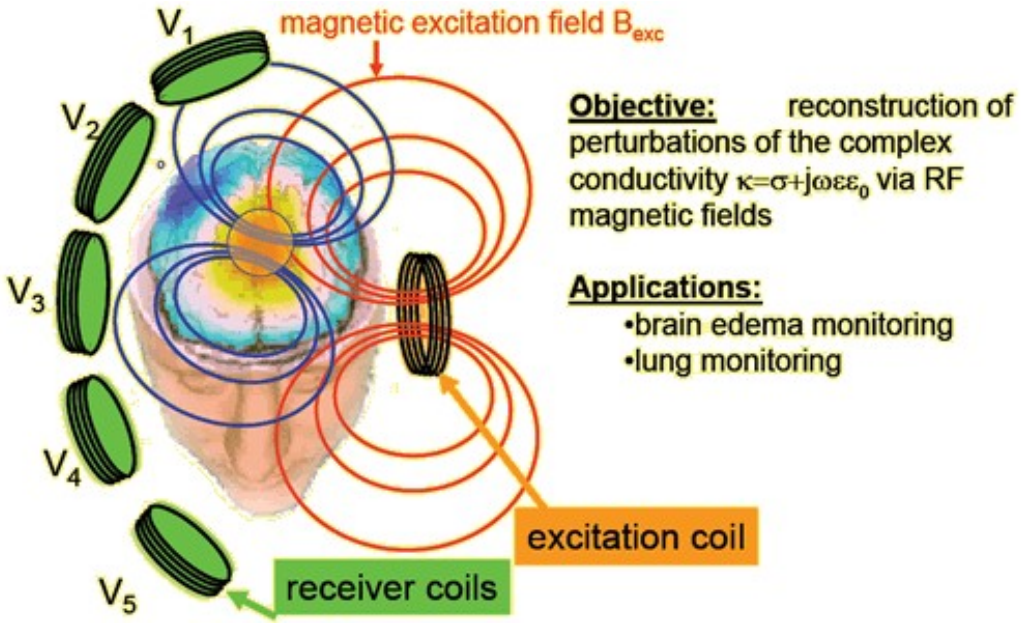

Figure 2.3: Principle diagram of magnetic induction tomography

technique, Shao et. al have shown that a conducting tip attached to the controller of an atomic force microscope can make images of (surface) electrical impedance [37].

2.3.3 Limitations of current modalities

The most important challenge facing current EIT systems is to improve the spatial resolution. For a typical EIT configuration with 16 electrodes, there are only 16 projections and 104 independent measurements that can be obtained for image reconstruction. Compared to several hundreds of projections and tens of thousands of measurements in CT system, the measurements in conventional EIT system are physically limited by the number of electrodes that can be placed on the surface. Further, these measurements are obtained on the surface and therefore lead to a lower sensitivity for the conductivity perturbations at the center, which results in a nonuniform spatial resolution: it is better at the edge and falls gradually toward the

center [38]. It is estimated that in the center, the spatial resolution is only about 10% of the measured region [39]. The image resolution may be improved by increasing the number of electrodes placed on the boundary. However, the fabrication and the size of electrodes limit this approach. The interference from other electrodes may also generate unpredictable noise. Furthermore, more electrodes lead to difficulty of the placement and implementation in clinical applications.

Another challenging issue in EIT systems is to obtain the absolute value of conductivity images. Many researches have reported attempts to reconstruct the absolute impedance image. Korjenevsky et. al. represented that static images of resistivity distribution can be achieved using a modified version of the backprojection method [40]. In computer simulations, due to the perfect data with known parameters in a perfect coordinate system, the absolute image can be obtained more easily. However, in practice, the location errors of electrode placement can be very problematic especially in clinical applications. For example, it could be very difficult to form a rigid ring of electrodes around the non-regular shape of the body. Scientists have also found that contact resistance is another source of error for an EIT system.

One big challenge in MREIT and MIT is the use of MR that introduce more electrical risks, lots of radiations and even dyes to patients. It should also be emphasized that with MREIT, only the relative conductivity values can be reconstructed using the magnetic flux density measurements alone. In order to find the absolute conductivity values, at least one voltage measurement from the boundary is required. For the recent modalities with AFM, the efforts to increase the resolution have concentrated primarily on the miniaturization of the excitation probe. Even though this

miniaturization has resulted in an increase in the resolution, the spreading of the field limits this improvement.

2.4 Inverse problems

The scanning impedance imaging is a low-frequency near field imaging modality similar to electrical impedance tomography. As we know, the near field imaging resolves sub-wavelength structures in the near field which leads to a complex inverse problem of its image reconstruction. In this section, the definition and popular approaches of inverse problems are discussed for the near field imaging.

Inverse problems are related to the forward (or direct) problems by exchanging the knowns with the unknowns by mathematical definition:

1. typically one problem is designated the forward while the other is designated the inverse

2. the forward problem is often the one which has been more thoroughly explored.

On the other hand, for practical applications, we can state that: in an inverse problem we solve for the cause given an observed effect while the forward problem is the calculation of effects from causes. Basically, we solve for an unobservable space, dimension or earlier time from observable data. Bertero and Bocca gave a more insightful description of inverse problems as those problems which result from a loss of information in the forward problem[41]. It can be considered in this way: a small amount of noise in the data can lead to enormous errors in the estimates. This instability phenomenon is sometimes due to ill-posedness. Hadamard [42] gave a

Table 2.2: Example forward and inverse problems

Problems	Given	Compute
Forward	Electromagnetic sources	Electromagnetic fields
Inverse	Electromagnetic fields	Electromagnetic sources
Forward	Sharp image	Blurred image
Inverse	Blurred image	Sharp image
Forward	Conductivity distribution	EIT measured data
Inverse	EIT measured data	Conductivity distribution

precise definition of ill-posedness by defining well-posedness. An inverse problem is well-posed if:

1. A solution exists for any data d in the data space
2. A unique solution f exists in the image space
3. The inverse mapping $d- > f$ is continuous

A problem is ill-posed if one of the above three conditions is not satisfied.

Inverse problem arise in a variety of important applications in science and industry, especially biomedical and geophysical imaging. Table 2.2 shows a series of common inverse problems along with corresponding forward problems. Generally, inverse problems can be classified to two major groups, inverse problems for linear and nonlinear systems. Figure 2.4 shows a diagram of typical inverse problems. It can be seen that for this system,

$$g = A(f),$$

the inverse process performs the estimation of f from the observation g. From the probability theory, the solution of this inverse problem is the Maximum a Posteriori

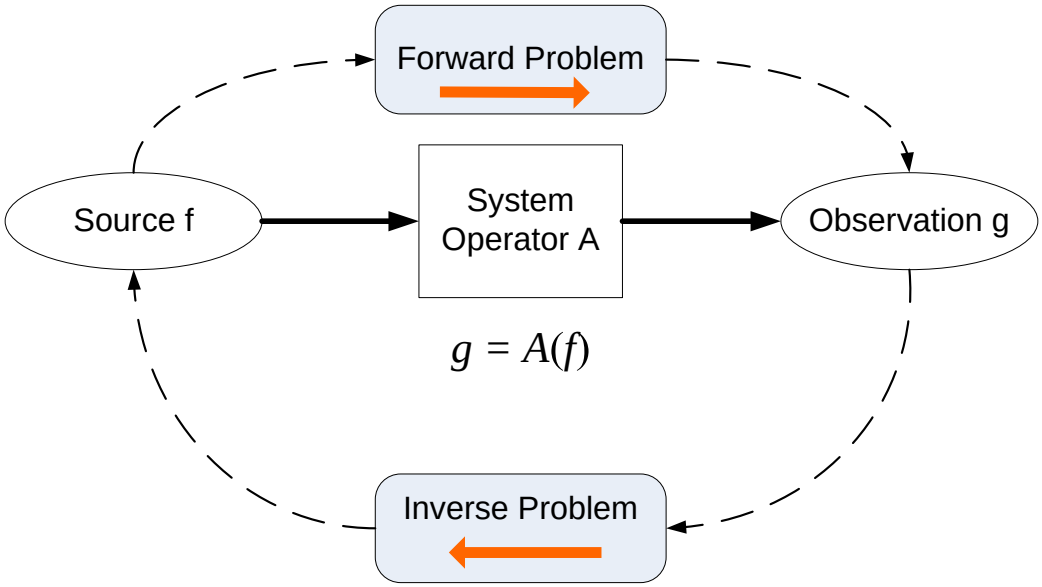

Figure 2.4: Diagram of a typical inverse problem

(MAP) estimation:

$$\hat{f} = \arg\max_f p(f|g), \tag{2.7}$$

where $p(f|g)$ is the conditional probability of f given g. The MAP method estimates f as the mode of the posterior distribution of g. From Bayes theory, the conditional probability $p(f|g)$ satisfies

$$p(f|g) = \frac{p(g|f)p(f)}{p(g)}, \tag{2.8}$$

where $p(f)$ and $p(g)$ are the marginal probability of f and g, and $p(g|f)$ is the conditional probability of g given f. The denominator $p(g)$ of the posterior distribution does not depend on f and therefore plays no role in the optimization. Thus, the MAP estimator is

$$\hat{f} = \arg\max_f p(g|f)p(f) \tag{2.9}$$

or,

$$\hat{f} = \arg\min_f -\log p(g|f) - \log p(f). \tag{2.10}$$

The conditional probability $p(g|f)$ is known as the likelihood function and can be obtained from the sample distribution of g given f in the forward problem. The probability of f, $p(f)$, however, cannot be obtained from the observation g and therefore demands additional information in many inverse problems. Providing additional information of $p(f)$ to the optimization in the solution of an inverse problem is the motivation of regularization.

2.4.1 Regularization

As mentioned above, inverse problems are often ill-posed. To solve these problems numerically one must introduce some additional information about the solution, such as an assumption on the smoothness or a bound on the norm. The same idea arose in many fields of science. A simple form of regularization applied to integral equations, generally termed Tikhonov regularization after Andrey Nikolayevich Tychonoff, is essentially a trade-off between fitting the data and reducing a norm of the solution. More recently, non-linear regularization methods, including total variation regularization have become popular.

Tikhonov regularization

Tikhonov regularization is the most commonly used method of regularization of ill-posed problems. In some fields, it is also known as ridge regression.

For a system,

$$g = A(f),$$

the generalized Tikhonov regularization is

$$f_\lambda = \arg\min_f T_\lambda(f;g) = \arg\min_f ||A(f) - g||_2^2 + \lambda||f||_2^2. \tag{2.11}$$

where $||\cdot||_2^2$ is the Euclidean norm and $||A(f)-g||_2^2$ is the term that represents the error between g and $A(f)$. $||f||_2^2$ is the regularization term (sometimes called as penalty term) where $\lambda > 0$ is the regularization parameter. Although at first the choice of the solution to this regularized problem may look artificial, and indeed the parameter λ seems rather arbitrary, the process can be justified in a Bayesian point of view. Note that for an ill-posed problem one must necessarily introduce some additional assumptions in order to get a stable solution. Statistically we might assume that a priori we know that x is a random variable with a multivariate normal distribution. For simplicity we take the mean to be zero and assume that each component is independent with standard deviation σ_f. Our data is also subject to errors, and we take the errors in g to be also independently multivariate normal distributed with zero mean and standard deviation σ_g. Under these assumptions the Tikhonov-regularized solution is the most probable solution given the data and the a priori distribution of x, according to Bayes' theorem. The regularization parameter is then $\lambda = \frac{\sigma_g}{\sigma_f}$. Comparing Equation (2.11) to Equation (2.10), the following relationship can be established

$$||A(f) - g||_2^2 = -\log(p(g|f)), \lambda||f||_2^2 = -\log(p(f)). \tag{2.12}$$

Notice that this relationship is valid only if the noise has the normal distribution.

The purpose of Tikhonov regularization is to find a balanced point between the resolution and signal-to-noise ratio (SNR). If we do not have much prior infor-

mation, due to the noise, we cannot obtain original data from what we observe. An unregularized inverse system amplifies noise for nodes corresponding to small singular values. So the better resolution we get, the worse SNR we get at the output of the inverse system. In other words, there is a trade-off between resolution and SNR that we want to optimize. The Tikhonov regularization is the method for balancing the penalty term (SNR) and discrepancy term (resolution). There are several detail definitions for both resolution and SNR in various cases. Now, one general set of definitions is applied to a linear shift-invariant system,

$$g(x) = (h_A * f)(x) + \sigma\zeta(x)$$

where $\zeta(x)$ is unit variance noise, $f(x)$ is the original vectorized image, h_A is the kernel function of the linear shift-invariant operator A. The corresponding generalized Tikhonov regularization is

$$f_\lambda(x) = (h_\lambda * h_A * f)(x) + \sigma h_\lambda * \zeta(x).$$

It is useful for estimating the noise effect of a filter by measuring the change of SNR when the noise pass through a filter. It is called SNR gain of the filter defined as

$$\tau = \frac{SNR_{out}}{SNR_{in}}$$

and for resolution

$$\Delta = 2\pi\sqrt{\frac{\sum \sigma_i^2}{n}}$$

where

$$\sigma_i^2 = \frac{2\int (x_i - \mu_i)^2 |h(x)|^2 dx}{\int |h(x)|^2 dx}.$$

Assuming that the noise $\sigma\zeta(x)$ is white and the regularized deblurring filter h_λ is symmetric in frequency domain, we can obtain the SNR of the whole regularization system.

$$\tau = \frac{SNR_{out}}{SNR_{in}} = \frac{\int |\hat{h_A}\hat{f}|^2 d\omega}{|\hat{h_\lambda}(0)|^2 \int |\hat{h_A}\hat{f}|^2 d\omega}$$

and

$$\Delta = 2\pi \sqrt{\frac{2}{n} \frac{\int \sum |\frac{\partial \hat{h_A}}{\partial \omega_i}|^2 d\omega}{\int |\hat{h_A}|^2 d\omega}}.$$

The Tikhonov filter h_λ is a function of the parameter λ, therefore, the resolution and SNR gain are also the functions of λ. By varying λ, the L-curve can be obtained for $\tau(\lambda)$ vs $\Delta(\lambda)$. It is usually like a decreasing curve with a corner point. Hence, that corner point is the best point for balancing the resolution and noise. This is the basic idea of Tikhonov regularization: due to the noise, it is impossible to obtain the original image, even with an invertible blurring filter, hence the only thing we can do is regularization with limited deblurring.

Total variation regularization

The Total Variation functional is assuming an important role in the regularization of inverse problems belonging to many disciplines, after its first introduction by Rudin, Osher and Fatemi (1992) [43] in the image restoration context. Total variation is a regularization technique that takes into consideration the information that the data set is blocky and discontinuous. Most of the regularization methods assume

the data sets to be smooth and continuous, but total variation does not assume the same. It measures the discontinuities in the image data set. Since a smooth solution is desirable in many applications while others require discontinuity or steep gradient to be computed. One approach is to replace norm l_2 in Tikhonov regularization with the norm l_1 , i.e., the 1-norm of the first spatial derivative of the solution. This is called the total variation (TV) regularization. This method will help to obtain the discontinuities or steep gradients in the restored image. The total variation can be expressed as

$$T(f) = ||A(f) - g||_2^2 + \lambda TV(f).$$

where λ is the regularization parameter and $TV(f)$ is the penalty term for the total variation regularization which is defined as

$$TV(f) = ||\nabla f||_1 = \int_\Omega |\nabla f| d\Omega.$$

Here more details about the norm need to be discussed to distinguish Tikhonov and total variation regularizations. The norm can be given by a general expression,

$$||x||_p = \left(\sum_i |x_i|^p \right)^{\frac{1}{p}}.$$

Some cases have special meaning and names:

1. p=1, $||x||_1 = \sum_i |x_i|$ is known as Manhattan norm because it corresponds to the sum of the distances along the coordinate axes.

2. p=2, $||x||_2 = \sqrt{\sum_i |x_i^2|}$ is known as Euclidean norm, or the vector length. In this thesis, $||x||$ represents Euclidean norm if no specification.

The change to the 1-norm has a dramatic effect on the computation of the solution. It has been proved by P.C.Hansen that the solution consists of polynomial pieces, and the degree of polynomials is p-1. However, $TV(f)$ is not differentiable at zero. So in order to avoid this difficulty a small positive constant value is added,

$$TV(f) = \int_{\Omega} \sqrt{|\nabla f|^2 + \beta^2} d\Omega.$$

Thus the total variation expression can now be expressed as

$$T(f) = ||A(f) - g||_2^2 + \lambda \int_{\Omega} \sqrt{|\nabla f|^2 + \beta^2} d\Omega.$$

The quantity $\sqrt{|\nabla f|^2 + \beta^2}$ is known as the gradient magnitude. In the image cases, this provides us with the information about the discontinuities in the image.

The minimization of the total variation functional is a penalty approach to the solution of the constrained problem. There are various methods to obtain this minimization:

1. Time Marching [43]
2. Steepest Descent and Newton's method
3. Lagged diffusivity fixed point iterative method
4. Primal-Dual Method

2.4.2 Some iterative methods for solving inverse problems

Steepest descent algorithm

Steepest Descent method can be interpreted as an improved Landweber method by choosing τ for every iteration. The fix-point equation is

$$f_{k+1} = f_k + \tau_k[\bar{g} - \bar{A}(f)].$$

The function that this iteration was attempting to minimize is defined under mean square concept,

$$J(f; g) = ||g - A(f)||^2.$$

Hence, for steepest descent algorithm, we choose τ_k so that $J(f; g)$ is as small as possible.

$$\tau_k = \arg\min_{\tau} J(f_k + \tau_k[\bar{g} - \bar{A}(f)]; g).$$

From geometrical view, the steep descent method starts from an initial point, moves in the orthogonal direction of the tangent plane until reaching a new tangent plane parallel to the moving direction, then repeats this process with the new point as the initial point. It is like going as far as possible in the gradient that is the quickest decreasing direction to the center in some sense.

Conjugate gradient algorithm

The Conjugate Gradient algorithm reduces the problem from k-dimension to (k-1)-dimension for each step with the residual error orthogonal to the space,

$$f_k = \arg \min_{f \in K^{(k)}(\bar{A};g)} J(f;g),$$

where

$$J(f;g) = ||g - A(f)||^2,$$

and $K^{(k)}(\bar{A};g)$ is the Krylov subspace,

$$K^{(k)}(\bar{A};g) = span\{\bar{g}, \bar{A}\bar{g}, ..., \bar{A}^{k-1}\bar{g}\}.$$

The update equation is

$$f_{k+1} = f_k + \alpha_k p_k$$

where p_k is the conjugate gradient direction with the following constraint,

$$(p_{k+1}, \bar{A}p_k) = 0,$$

which means the successive conjugate gradients are orthogonal with respect to $\bar{A}$. And also the successive residuals are orthogonal,

$$(\bar{r}_{k+1}, \bar{r}_k) = 0.$$

Non-linear conjugate gradient

The Non-linear Conjugate Gradient algorithm is an extension of the linear CG algorithm with a little change,

$$\bar{r}_k = -\nabla J(f_k)$$

and

$$\alpha_k = \arg\min_{\alpha>0} J(f_k + \alpha_k p_k).$$

The update equation for f_k is the same as the linear form,

$$f_{k+1} = f_k + \alpha_k p_k,$$

but, the update equation for p_k is different,

$$p_{k+1} = -\nabla J_{k+1} + \beta_k p_k.$$

For the calculation of β_k, there are several variations of non-linear conjugate gradient method. The Fletcher-Reeves variant of the nonlinear conjugate algorithm generates p_{k+1} from the simple recursion by calculating β_k as

$$\beta_k = \frac{||\nabla J_{k+1}||_2^2}{||\nabla J_k||_2^2}.$$

The method's performance is sometimes enhanced by re-starting, that is, periodically setting β_k to zero. The Polak-Ribiére variant of conjugate gradient defines β_k as

$$\beta_k = \frac{(\nabla J_{k+1} - \nabla J_k, \nabla J_{k+1})}{(\nabla J_k, \nabla J_k)}.$$

These two definitions of β_k are equivalent when J is quadratic, but not otherwise. Numerical testing suggests that the Polak-Ribiére method tends to be more efficient than the Fletcher-Reeves method.

2.4.3 Impedance image reconstruction

The problem of reconstructing impedance images from electrical measurements on the surface of tissues or the body of a patient belong to the class of inverse problems. This inverse problem is challenging and has received quite a bit of attention in the literature. The imaging device (the impedance electrodes) provides measurements of a transformation of the impedance information. In practice, these measurements are both incomplete (sampling) and inaccurate (statistical noise), which means that one must give up recovering the exact image. Indeed, aiming for full recovery of the impedance information usually results in unstable solutions. This means that the reconstructed image is very sensitive to inevitable measurement error. Otherwise expressed, slightly different data would have produced a significantly different image. Hence, image reconstruction in electrical impedance imaging is a complex ill-posed inverse process.

Most techniques of image reconstruction in electrical impedance imaging have been focused on EIT systems.

For EIT, image reconstructions are developed for static and difference imaging techniques. Static image reconstruction uses one set of data to carry out the image reconstruction. Unfortunately, this type of image reconstruction suffers from sensitivity to errors in positioning electrodes on the surface of the body. Variations

in electrode positioning significantly affects the impedance distribution in center of the object, since EIT is more sensitive to changes on the boundary of the medium than changes within the medium[40]. Difference image reconstruction uses two sets of data and calculates a difference in conductivity. Barber has shown that difference imaging is relatively insensitive to errors in electrode placements as long as these remain constant during the experiment[44]. Generally, the existing algorithms of image reconstruction can be classified into two categories: non-iterative linearization based algorithms, and true iterative algorithms solving the full problem.

2.4.4 Non-iterative algorithms

Non-iterative algorithms usually require linearization and some assumptions for approximation. One assumption is that the conductivity differs only slightly from a known conductivity[45]. Sometimes, homogeneous assumption is also claimed. Among these linearization non-iterative methods are back-projection methods [46, 26, 47]. The backprojection method for image reconstruction used in Barber and Brown's original work is popular in X-ray tomography systems and has enjoyed great success in this field[48]. It has been used in multi-frequency systems to image change of conductivity with respect to excitation frequencies. However, backprojection methods are generally used with APT systems and are limited to producing dynamic images for difference imaging techniques. The basic projection method is based on back projecting the potential difference between two equipotential lines on the surface to the impedance value between those two equipotential lines. Then, all the impedance values are averaged over the entire image after all projection angles. They also premised that there is an approximately linear relationship between the perturbations of the

measured voltage gradients and those of the reference distribution; and there is an approximately linear logarithm of the conductivity perturbation from the reference distribution.

In [49], Barber and Brwon's backprojection algorithm was explained as an approximate inverse of Beylkin's generalized Radon transform [50] and it was used as a preconditioner in an iterative, conjugate residual method for the numerical solution of linearized system. Berenstein and Tarabusi gave a more precise characterization [51]. They showed that the linearized impedance imaging problem in a unit disc can be interpreted exactly in terms of the Radon transform with respect to the Poincare metric and a convolution operator. Barber and Brown's turns out to be a crude approximation of the exact representation in [51], which works best for smooth the gradient of impedance and for points near the surface. Finally, as expected, the inversion of the convolution operator in [51] is unstable and, so far. there is no known exact (or fully satisfactory) reconstruction of the gradient of impedance inside the region of interest.

Cohen-Bacrie developed an algorithm with linearization assumption using a variance uniformization constraint. The goal is to improve the tradeoff between the quality of the images and the numerical complexity of the reconstruction method. In order to reduce the computational load, they adopted a linearized approximation to the forward problem that describes the relationship between the unknown conductivity and the measurements. In this framework, they proposed a proper way to cope with the ill-posed nature of the problem, mainly caused by strong attenuation phenomena; this was done by devising regularization techniques well suited to this particular problem. They proposed a solution which is based on Tikhonov regular-

ization of the problem. Then, they introduce an original regularized reconstruction method in which the regularization matrix is determined by space-uniformization of the variance of the reconstructed conductivities. Both methods were nonsupervised, i.e., all tuning parameters were automatically determined from the measured data. They used a variance uniformization constraint in the regularization that yielded further improvements, particularly in the central region of the unknown object where attenuation is most severe.

Some nonlinear non-iterative algorithm have also been developed in recent decades. Cheney et. al. were the first to propose the layer stripping method[52]. Layer stripping algorithms recover the unknown impedance distribution, layer by layer, starting from the surface and progressing inside the region[53, 54]. They used the measurements on the surface to estimate the impedance of the outermost layer and then performed the next layer with this layer along with all the measurements. This process continued until the center of the region was reached. Cheney claimed that this method could produce a higher contrast of the impedance image. However, this method is extremely unstable and, as such, it cannot be used for imaging, even for noiseless data, due to round-off errors[55]. In general, it is not known how to stabilize the layer stripping approach, but there exists a stable algorithm, developed by Sylvester in [54] for one dimensional EIT. Ikehata and Siltanen proposed a similar algorithm[56]. Note that this algorithm is inspired by the ideas of Kirsch for shape characterization of obstacles in inverse scattering[57]. In fact, Kirsch's approach is quite similar to a well known signal processing method called as multiple signal classification (MUSIC)[58, 59], as is pointed out by Cheney[60]. Finally, another very promising approach for locating interfaces of jump discontinuity of the impedance was proposed as level set method, as shown for example in [61, 62, 63, 64].

2.4.5 Iterative algorithms

Iterative algorithms involve in solving the full nonlinear problem with a true forward model that can describe the implicitly nonlinear relationship between the impedance inside and the measurements on the surface. Usually, they can be separated into two steps as general inverse problems.

- The first step, the forward problem, involves in modeling the measuring process and establishing the relationship between the impedance distribution of the internal and the measurements (currents or voltages) on the surface. Basically, the forward problem tries to interpret the measurements as a function of impedance. Many methods can be used to solve the forward problem such as the finite difference method (FDM), the finite element method (FEM), a direct solution, and a simulation of an equivalent network of resistors.

- The second step, the inverse problem, performs the inverse process of the relationship in the forward problem in order to retrieve the impedance. This algorithm must be initialized with a first guess of the impedance distribution, usually taken as uniform. Next, a forward problem simulates the measuring process. By comparing the simulated currents to the data, one update the impedance estimation until they agree. It can be noticed that in each iteration, the simulation of the measuring process requires the computation of the forward problem at least once. Hence, the complexity of the inverse problem depends largely on how the forward problem is modeled.

These approaches are often given by output least squares methods[65][66][67][68]. In the least-squares method, an objective function is selected, and the residuals of this

function are minimized in the least-squares sense [69, 70, 71]. As mentioned above, a forward solver is used to determine the boundary voltages that would be produced given the applied current vectors and the present estimate of the impedance distribution as part of each iteration in the minimization. In general, the computational complexity of the forward solver is much greater than that of the least-squares minimization. All nonlinear output least squares algorithms minimize some least-square cost functional with some Newton-type method [72].

Many studies based on the Newton's optimization method have been done for electrical impedance imaging, especially for EIT. The perturbation method [73] was an early attempt to apply Newton's method to EIT. A sensitivity matrix was constructed by changing the resistivity of one element at a time and forward modeling. This was then used as the derivative matrix of the boundary voltages with respect to the element resistivities. The measured boundary data was applied to the sensitivity matrix to determine a new set of resistivity values. The process was then repeated iteratively. The perturbation method produces accurate images in simulations but convergence is slow in comparison with other methods because the sensitivity matrix is computationally intensive to calculate and must be calculated for each iteration. This technique is important historically as one of the first iterative methods to be used in EIT but is no longer in use.

Afterwards, other Newton's methods were proposed for impedance imaging by seeking to minimize the mean squares of the voltage/current difference between those generated by a model and those measured from the observed region. The difference between the two values is sometimes termed the objective function. The minimization is achieved by obtaining the derivatives of the objective function with

respect to impedance. This derivative is assigned to zero, which corresponds to a local minimum of objective function. This would correspond to the impedance which produces the boundary voltages/currents closest to the measured voltages/currents in the least-squares sense. A system of equations is therefore generated which when solved will give the closest approximation of impedance in terms of the objective function. Since the inverse problem of EIT is ill-posed, recent Newton's methods seek to minimize a total cost functional including both objective functional and a regularization term instead of the objective functional itself.

Yorkey et al. was one of the first to use an iterative method for impedance image reconstruction [74]. He used a modified Newton-Raphson method to compute the conductivity distribution. He demonstrated that this reconstruction method converged faster than any of the other contemporary methods (the layer stripping algorithm was published later) and that the first iteration produced less error than the backprojection method. Yorkey found that this method is ill-posed because of the high condition number of the Hessian matrix. Thus, he used a Levenberg-Marquardt [75, 76] regularization technique to overcome this problem.

Similarly to Yorkey's method, Newton's one-step error reconstructor (NOSER) [70] algorithm and its functionally equivalent, but computationally streamlined version, fast NOSER (FNOSER) [77], performs 2-D reconstructions using only one step of least-squares minimization. The forward solver in FNOSER is relatively simple because it is used to predict the boundary voltages only for the case when the impedance distribution in the region is homogeneous and isotropic and the shape of the region is known. The boundary voltages can then be directly computed from the current vectors and this impedance value. Essentially, the FNOSER algorithm first finds the

value of the homogeneous impedance that minimizes the error functional and then performs one additional iteration of the minimization. As a further simplification, FNOSER operates on the in-phase and quadrature voltage measurements independently, as opposed to using the complex voltage values. The real-valued results from these individual reconstructions are then combined to estimate the components of the complex impedance.

The Newton method for more than one iteration requires the solution of the forward problem and the computation of the derivatives of the cost functional for each iteration. This leads to a considerable amount of computation time. Comparing to the conventional back-projection method, the Newton's method is more accurate and has less sensitivity to noise. Another iterative approach was developed by Muria and Kagawa [69]. They used a theorem called Geselowitz Sensitivity to relate the changes of conductivity within the object to the differential voltage measured between two electrodes on the surface of the object. Wexler [78] proposed a different method that starts the algorithm with an initial value of the conductivity and solves for the distribution of current flow within the object, given a known pattern of current flow into the object.

In order to reduce the computation time, an iterative algorithm POMPUS [79] was developed by Paulson which uses optimal current patterns and considerably reduces the computational complexity required for multiple iterations of Newton's method. This method greatly reduces the time needed to produce images and hence considerably eases the problem of performing iterative reconstruction in real-time.

2.5 Summary

In this chapter, current studies of cellular imaging was reviewed and related to the electrical impedance imaging. Optical microscopy is the most widely used imaging modality of cellular imaging. However, it does not provide much contrast of the natural markers of electrical properties such as charge distribution and ion concentrations even though these electrical properties relate closely to cell function. On the other hand, electrical impedance imaging could reveal the distribution of these electrical properties from the image data of the electrical impedance. Although many studies have reported for the electrical impedance measurements of cells, few could image the electrical impedance of cells due to the low resolution of current modalities of the electrical impedance imaging. In the next chapter, the scanning impedance imaging that could potentially provide high-resolution electrical impedance images of cells will be presented. This new technique uses high resolution scanning techniques similarly to the scanning probe microscopy. Its indirect contact configuration and shielded probe design result in high resolution near field imaging of electrical impedance where the image reconstruction is a complex inverse problem. Due to the similarity in physics, scanning impedance imaging has similar image reconstruction as electrical impedance tomography. The review in this chapter of inverse problems and their relationship to the image reconstruction of electrical impedance tomography provide the basis of the development of the image reconstruction for scanning impedance imaging. In later chapters, we will discuss the details of image reconstruction of scanning impedance imaging.

Chapter 3

Scanning electrical impedance imaging

3.1 Motivations and theory

This thesis is motivated by the idea of applying the modalities of electrical impedance imaging to microscopic tissue imaging, ultimately cellular imaging. This idea is shown in Figure 3.1. It could be possible to provide more information for both cell anatomy and cell function if a high resolution image of some electrical properties rather than an optical image or a SEM image could be produced for cells. Among the electrical properties, the conductivity and permittivity are essential indicators that only depend on the ions, polar molecules and charge distributions inside a cell. As reviewed in the previous chapter, electrical impedance imaging has been developed

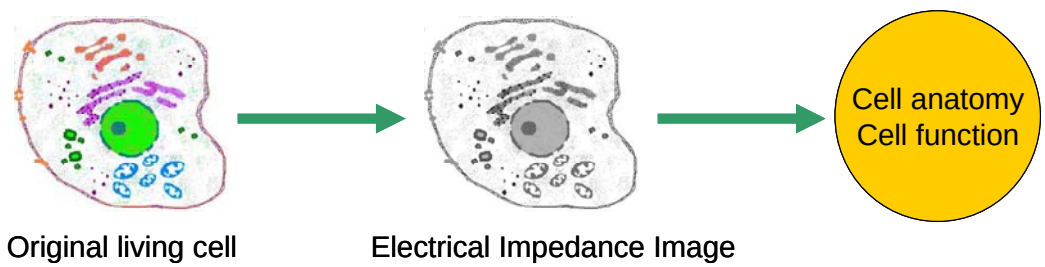

Figure 3.1: Motivation of Scanning Electrical Impedance Imaging.

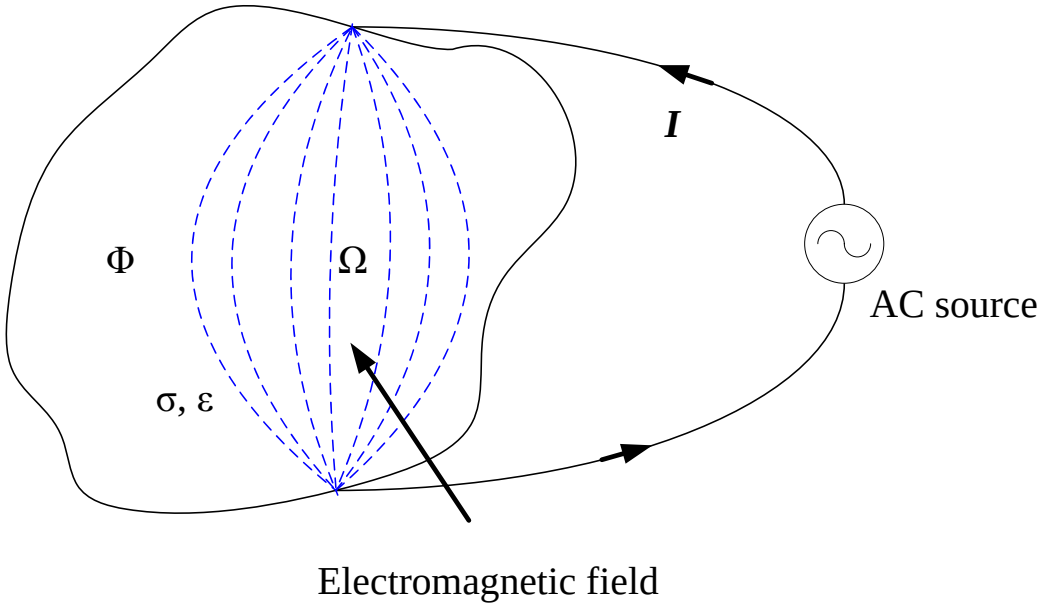

Figure 3.2: An AC source signal is applied to an object. Electromagnetic field is generated inside the object. The voltage on the surface and the current through the surface are related to the electromagnetic field, which reflects the essential electrical parameters of the object: conductivity σ and permittivityϵ.

as an interesting area of biomedical image process for researchers. It has been shown that measurements of internal electrical impedance of tissues could play a useful role in several medical applications such as cancer diagnosis. One distinction of electrical impedance imaging is the capability of imaging in vivo. However, most efforts in this area are oriented to large scale objects. Thus, a methodology that allows scientists observe the cell anatomy and function from the view of impedance is very promising.

Electrical impedance (or admittance) refers in general to the relationship between both conduction current and displacement current and an imposed electric field. All the methods applied to measure the electrical impedance are based on Ohm's Law. The basic idea is shown in Figure 3.2. A source (usually AC signal) is applied to the boundary of an object and the measurements of currents and voltages on the boundary are taken as an output of the internal electromagnetic field shown

in Figure 3.2. Then the impedance can be obtained by Ohm's Law,

$$Z = U/I \tag{3.1}$$

where Z is the total impedance, U is the voltage and I is the current. If the object is non-regular shape or inhomogeneous or both, then Equation (3.1) is not able to describe the concept of impedance reasonably well. Two essential parameters of materials: conductivity σ and permittivity ϵ are much better related to the imposed electric field and the total impedance Z can be seen as an integral of σ and ϵ in some sense. The general idea of electrical impedance imaging is to obtain a map of σ and ϵ distributions of the sample based on the measurements on the boundary.

When known voltages/currents are applied to the surface of an object, an electromagnetic field of E and B is excited with a distribution of the potential ϕ established as shown in Figure 3.2. Since the interested frequencies are in very low range, it is common to ignore the magnetic field B and redefine σ as the complex conductivity including the conductivity and permittivity for the impedance. If the distribution of the complex conductivity σ is known, the potential ϕ and the electric field E can be determined for all positions in the object with known voltages and currents on the surface. Then the current through the surface can be achieved by integrating the current density J over that surface. J can be obtained from impedance and the electric field. This can be considered as a forward problem with a nonlinear operator A,

$$I = A(\sigma). \tag{3.2}$$

Thus, the approach of impedance imaging is an inverse problem. Though this inverse problem is very complex and ill-posed, it is feasible to estimate the internal impedance distribution from the measurements of currents and voltages on the surface. Under this consideration, a novel approach for impedance measurements of small tissues and cells, named as Scanning Impedance Imaging (SII), is illustrated in Figure 3.3.

Scanning Impedance Imaging alters the geometry that is used in existing electrical impedance tomography systems. In SII, the probe is held above a conducting plane with the sample in between. The sample and probe are immersed in a conducting liquid that provides the electrical connection between the probe, the sample, and the ground plane. Because of this geometry, this technique is best applied to thin samples that can be placed on a flat surface - very suitable for cells or thin tissue samples. Figure 3.3 shows a representation of an SII system being implemented to provide an impedance map of a single cell. Here a small oscillating voltage (which could easily be varied in frequency) is applied between a probe and a conducting plane, and the impedance is calculated from the current through the sample. The probe is placed in a solution matching the cell's natural environment. The probe is moved over the cell in very small increments providing an impedance map of its entire area.

3.2 Imaging system setup

A typical SII system consists of several key elements that can be classified to three functional modules:

1. an impedance probe immersed in a a conducting solution with a sample inside

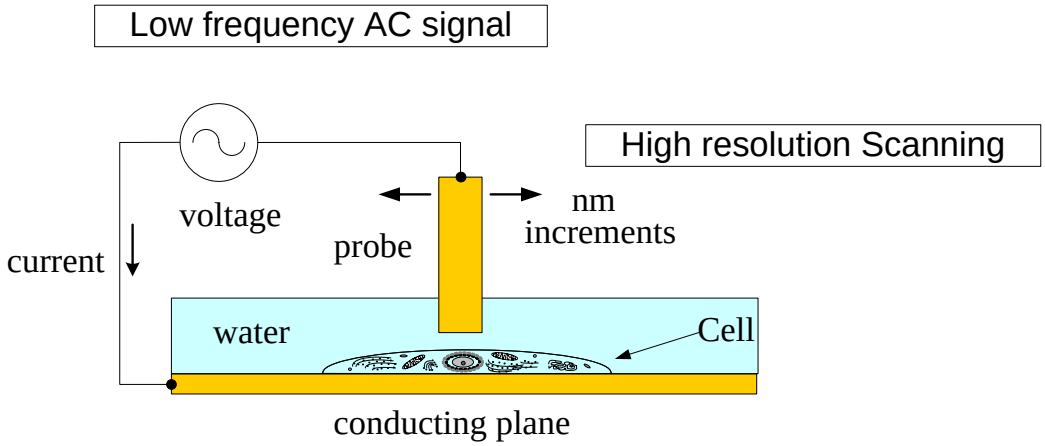

Figure 3.3: Basic idea of a Scanning Impedance Imaging system configured to measure the impedance of a single cell. A cell sample is placed between a conducting plane and a sensitive probe. An AC source with known voltage is applied to the probe and the current through it is measured. Measurements are taken on a 2-D horizontal plane by scanning the probe above the sample. It can be noticed that a fairly good impedance image can be obtained of the sample if the sample is pretty thin. High resolution even down to nanometer range can be expected with the micro-step scanning technique.

2. scanning control system

3. data acquisition and storage

Immersion of the probe in a conductive solution allows for innovative probe design without the constraint of making reliable electrical contacts directly between the probe and the material under test. Given that the electrical conductivity of the liquid inside and outside of the cell are approximately equal, changes in conductivity (impedance) will be due primarily to structures internal to the cell - resulting in a true volumetric measurement. Although only a single probe is shown in Figure 3.4, arrays of parallel probes could also be used allowing for high speed imaging with times limited only by the movement of the probe tips. In this way changes in cellular function could be monitored in real time with several updated images made each

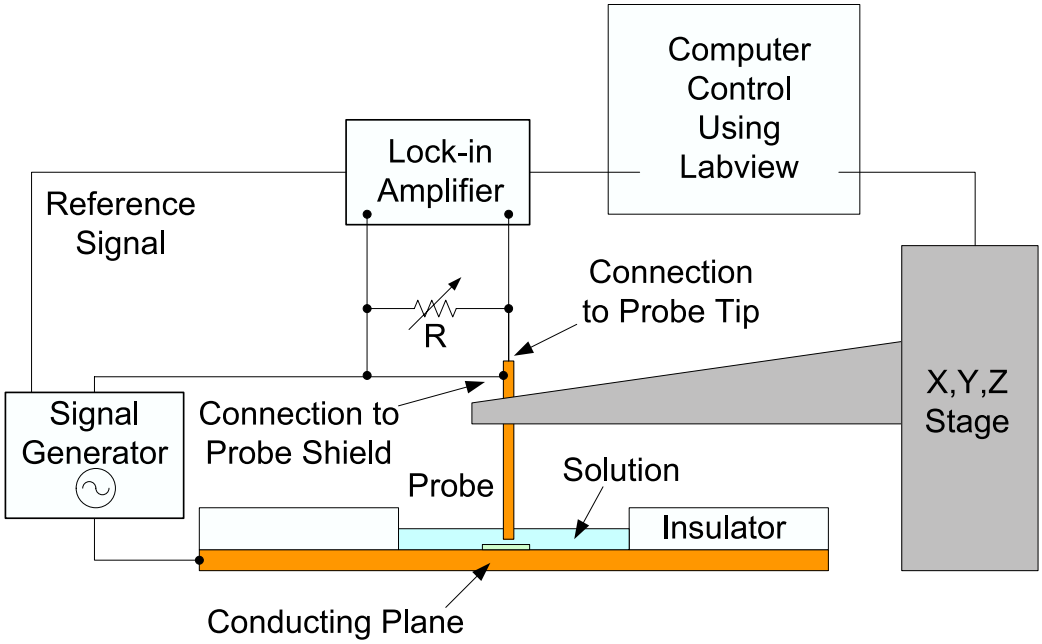

Figure 3.4: Experimental configuration of a typical SII system

second. Because the method is a non-contact measurement technique, it can be used for non-destructive testing of a wide variety of materials.

The realization of a scanning impedance imaging system is illustrated in Figure 3.4. As shown in the figure, a sample is placed between the end of a probe and a conducting plane. A conducting solution is filled in the space between the sample and the probe. A stage controller is used to move the probe, which has a minimum step increment around micron range. An AC signal generated by a programmable frequency generator is used to drive current through the probe and sample under test with a resistor (R) used for conversion to a voltage signal. A lock-in amplifier is used to measure voltage across the resistor and referenced to the signal generator. For current scale range, the use of a lock-in amplifier is not necessary because the signal-to-noise ratios produced in the system are very high. As probe geometry shrinks in the future and signal magnitude decreases and as phase shifts are evaluated in return

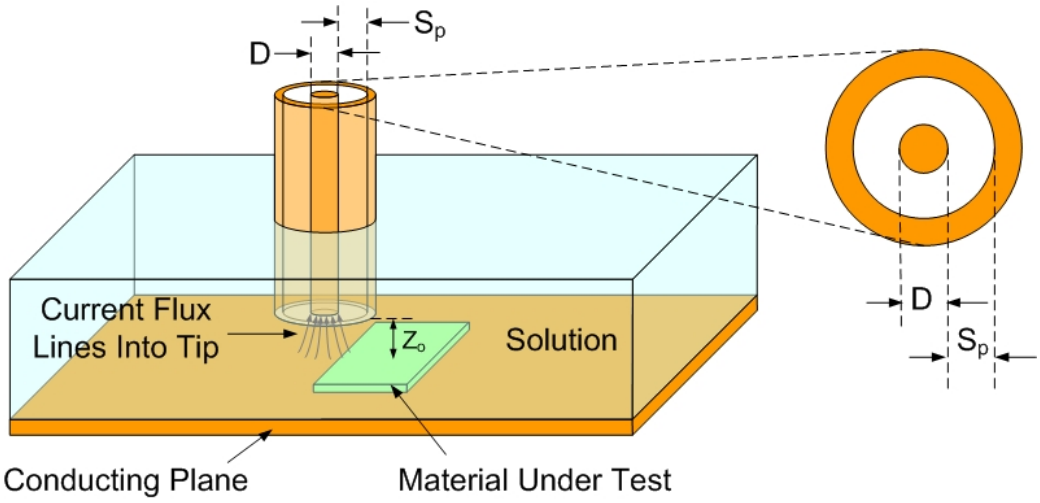

Figure 3.5: 3-D close up view of the probe area and a 2-D cross section view of the shielded probe

signals, this amplifier will likely be useful however. The AC drive voltage could also be lowered from 2.5 V to hundreds of millivolts in the current configuration without a significant loss in signal to noise ratio. This could be significant if it were desirable to minimize voltage across a sample like a cell wall or thin tissue. Finally, a computer running LabView controlled probe movement, data gathering, and storage.

Measurements of different horizontal positions above the sample are taken at a certain level to produce a current image. A simple impedance image can be obtained from the current image using a basic application of Ohm's Law wherein the impedance at each position can be calculated from the current through the tip and a fixed source voltage. However, this simple impedance image is not exact impedance distribution, which is blurred due to the current contributions from the neighborhood of the probe's measurement position. A shielded probe design with a coaxial geometry is introduced to help reduce this blurring effect. Figure 3.5 illustrates the structure of this novel probe design, where a central wire (tip) embedded in an insulator is surrounded by a conducting shield. Due to the immersion of the probe in the conducting solution,

this innovative probe design can be used without the constraint of a reliable electrical contact directly to the sample. The motivation of this new probe design is to eliminate the effects of the current flux from the region not directly under the end of the probe. This idea can be seen in the 3-D view in Figure [51]. Further, the shield can help to eliminate the noise generated by the entire conducting plane. The resistor ensures that the shield is at a higher potential than the central tip so that there is no capacity effect though the path of the tip, the shield, and the conducting plane. Therefore, most of the current flux through the tip comes from the sample area beneath the probe of total diameter no more than the tip diameter plus twice the shield spacing (S_p). Experimental evidence shows that the high resolution with high signal-to-noise ratio cannot be obtained using the simple unshielded point-source, no matter how small the diameter of the tip. The reason is that the measured current is affected by the entire plane. However, for our shielded tip, a higher resolution is reached with the same tip diameter as the simple one. In addition, a much higher contrast is also achieved.

3.2.1 System control and data acquisition

The whole system is controlled by a computer running LabView program. The program mainly performs two functions:

1. stage control - communication with stage controller
2. data acquisition - communication with lock-in amplifier or spectrum analyzer

Figure 3.6 shows that the process of the stage control in the SII system. The scanning is performed in three directions, thus, there are three independent channels for three

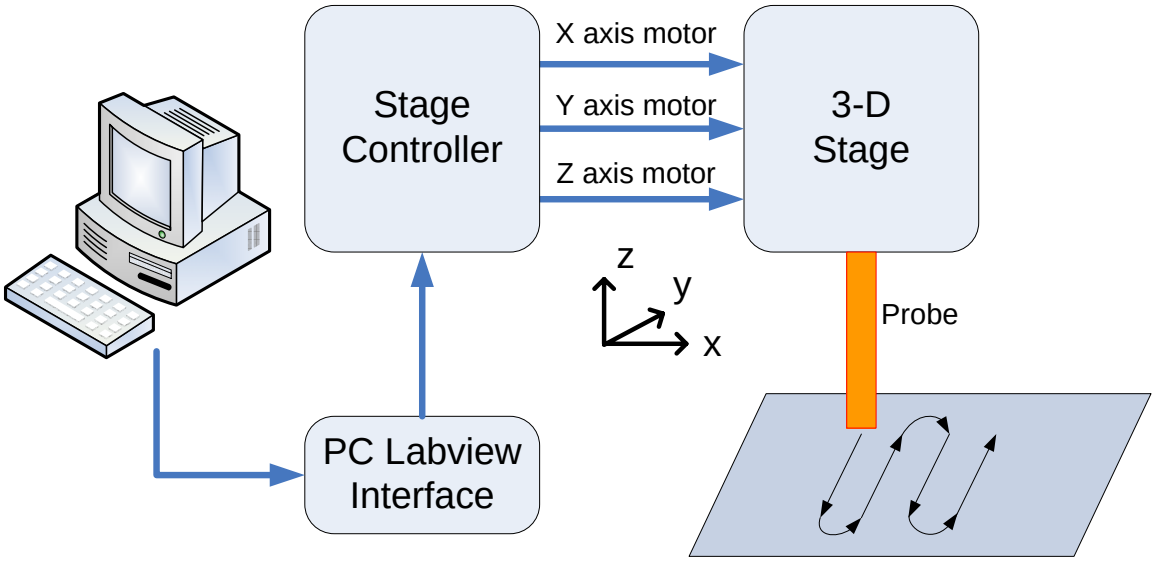

Figure 3.6: Diagram of the stage control using a computer in the SII sytem

motors of the XYZ stage. The moving process is implemented in the following way. A formatted command including the axis name such as 'x' or 'y' and the moving distance is generated using Labview and then transfered to the stage controller via serial port RS-232. The moving distance is translated to the number of smallest rotation degrees of the motor. After received, the stage controller interprets the command and sends voltages driving corresponding motors to move the stage in certain directions. For 2-D scanning process, a s-scan is used to produce a 2-D image for the impedance measurements as shown in Figure 3.6. An algorithm is integrated in the LabView for this special movement.

A Newmark Systems linear XYZ stage (model NLS4-4-16) is used for the high resolution scanning. Figure 3.7 shows the XYZ assembly configuration (a) for the stage and the internal structure for the motion control (b). The design of the NLS4 series stages is optimized for maximum stability and performance with the use of FEA analysis and incorporates the best in materials and component selection. The drive

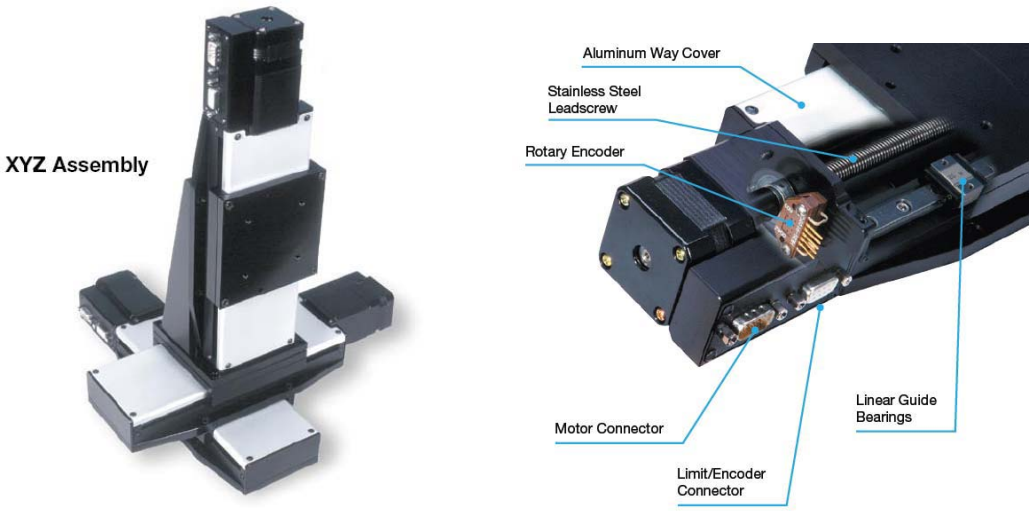

(a) (b)

Figure 3.7: The linear XYZ stage: Newmark Systems Model NLS4-4-16 (a) XYZ assembly configuration. (b)

system utilizes a stainless steel ACME leadscrew with internally lubricated plastic drive nut. The drive nut offers zero backlash operation that automatically adjusts for wear to insure zero backlash. The specifications lists in Table 3.1. It can be noticed that the resolution is very high up to 0.1 micron range. In practice, it is easier for the resolution around micron range, which is suitable for our requirements. The speed is fast enough to perform a 2-D s-scan in a reasonable time period.

Table 3.1: Specifications for the XYZ stage Model: Newmark Systems NLS 4-4-16

Resolution (0.250 in/rev lead)	0.13 μm @ 50,000 steps/rev motor resolution
Maximum Travel Speed (0.250 in/rev lead)	2 inches/second
Maximum Load	Horizontal: 50 lbs; Vertical: 15 lbs; Side: 40 lbs;

For the data acquisition, a lock-in amplifier is used to measure the voltage across the resistor R as shown in Figure 3.4. The shield is connected to the source directly while the central tip is connected to the source through the resistor R. The resistor R can be considered as a current to voltage transmitter. It provides the signal that is easy to be measured using a lock-in amplifier. It can be noticed that the voltage of the shield is a little bit higher than the voltage of the tip that buys enhancement of the shield function. Figure 3.8 shows this configuration clearly with a diagram of equivalent circuit. It can be observed that Z_4 has no effect on this circuit with known source voltage, and Z_3 is the impedance sought by the SII system. One important issue emerged here is the increased difficulty of the modeling work with this introduced resistor, since the voltage of the tip may vary depending on the current through it. Thus, neither the voltage or the current on the tip surface is not known, which need to be considered together with the modeling work of the internal electromagnetic field. This issue will be discussed more with the modeling work in Chapter 4. The lock-in amplifier used in the experiments is manufactured by EG&G Instruments. The Model No. is 7265. Besides the stage and the lock-in amplifier, the source generator (Agilent 33250A 80 MHz function/arbitrary waveform generator) is also controlled by the LabView program so that certain pattern signals can be generated as expected.

The control program including a loop procedure shown in Figure 3.9 is developed on LabView 7.0. First, the source generator, the stage and the lock-in amplifier are initialized to communicated with the computer. Then, a moving command is sent from the computer to the stage to move to the next position. After a response received, measuring commands are sent to the source generator and the lock-in amplifier to test the voltage across the resistor and the data is received and stored. This

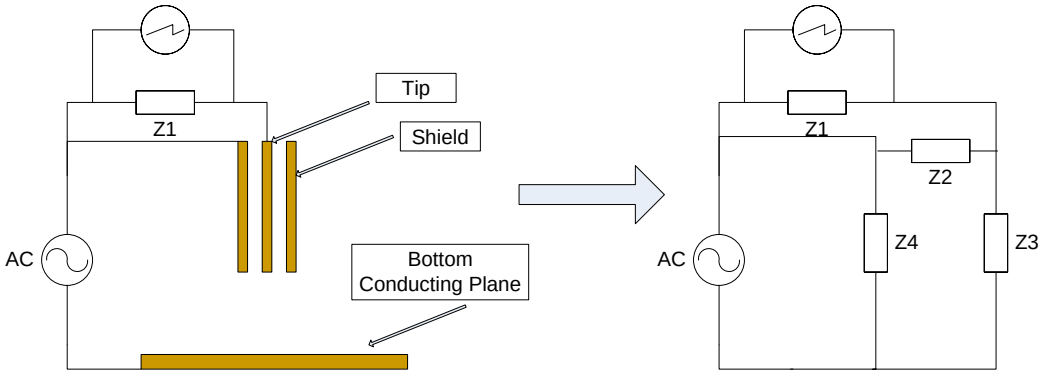

Figure 3.8: Equivalent circuit for the SII system. Z_1 is the feedback resistor, Z_2 is the equivalent impedance between the shield and the tip, Z_3 is the equivalent impedance between the tip and the ground-plane at each position, and Z_4 is the equivalent impedance between the shield and the ground-plane.

process is repeated until a scan is finished. All the communications are performed using VISA I/O control VIs. Figure 3.10 shows the implementation of the LabView program with both the front panel layout and the block diagram. It can be seen that there are stepsizes and ranges for scanning movements in the x,y,z directions and a waveform display for the receiving signals on the front panel. In the block diagram, there is a logic block coded in C that performs the controls of different scans. The data is stored orderly in a file after scanning. Matlab is used for data post-processing including display, resolution calculation, model matching and etc.

3.2.2 Probe design and fabrication

Of course the most critical component in the imaging system is the impedance probe. Impedance measurements are drastically different depending on the probe used. In order to improve the resolution and signal-to-noise ratio, a few probe designs are proposed, implemented and tested. Among them, a novel shielded design of the

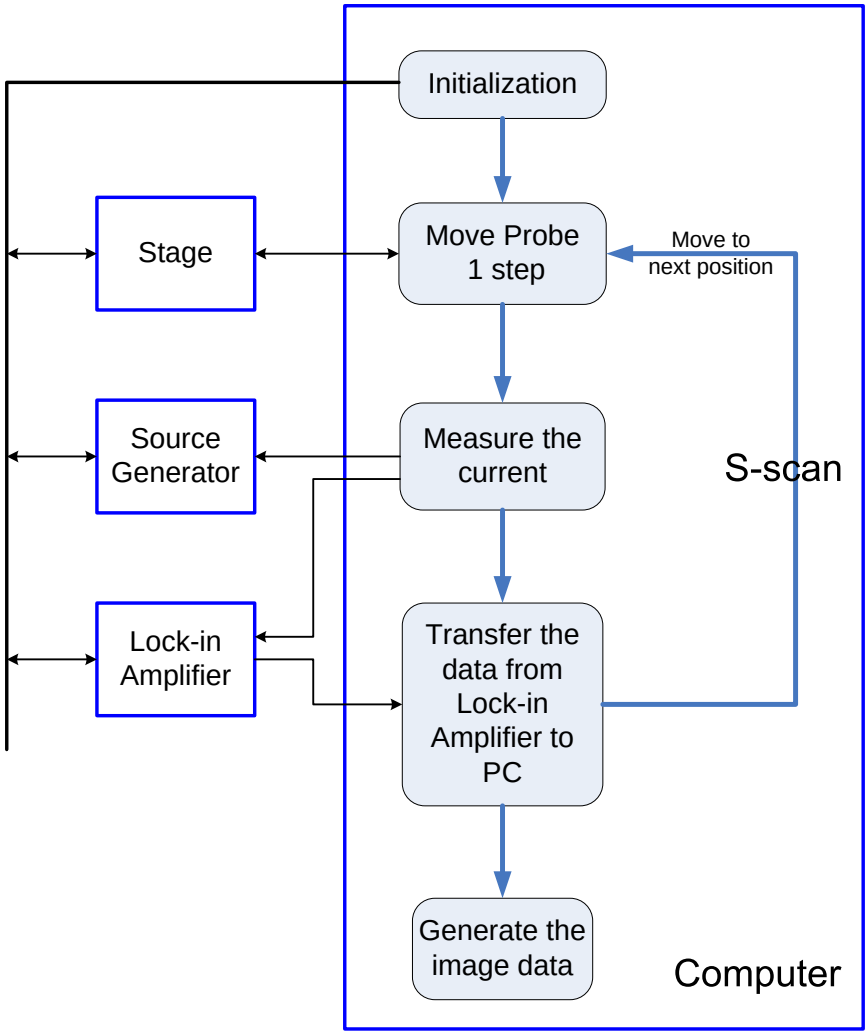

Figure 3.9: Flow diagram of the LabView program

impedance probe demonstrates great enhancement on both the resolution and the signal-to-noise ratio.

Shielded probe

The shielded probe is based on an inner conductor surrounded by an outer conductor as illustrated in Figure 3.5. The idea behind this design is to bias the outer conductor at a higher voltage than (or same voltage as) the inner conductor,

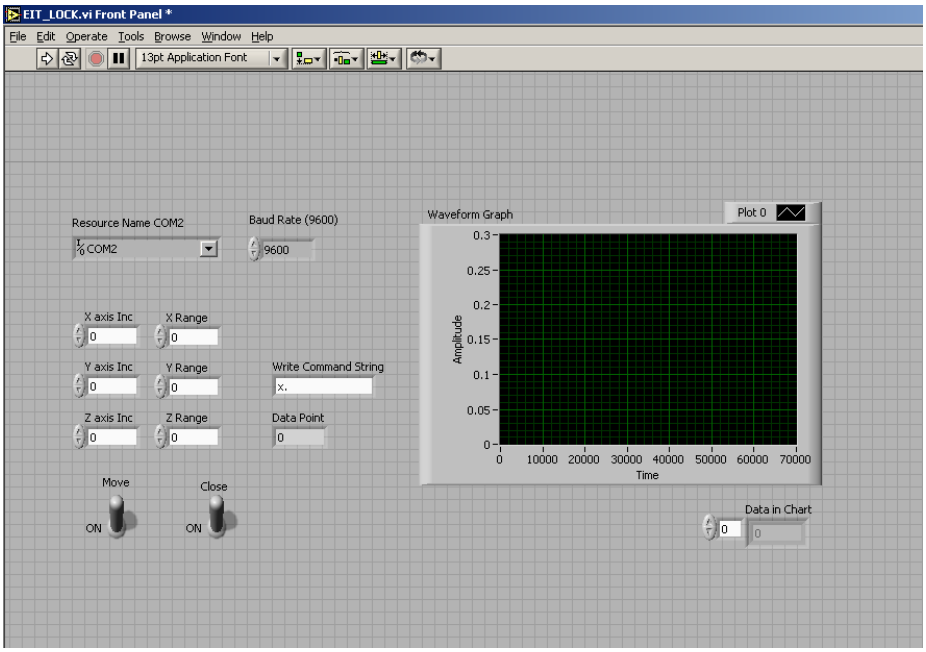

(a)

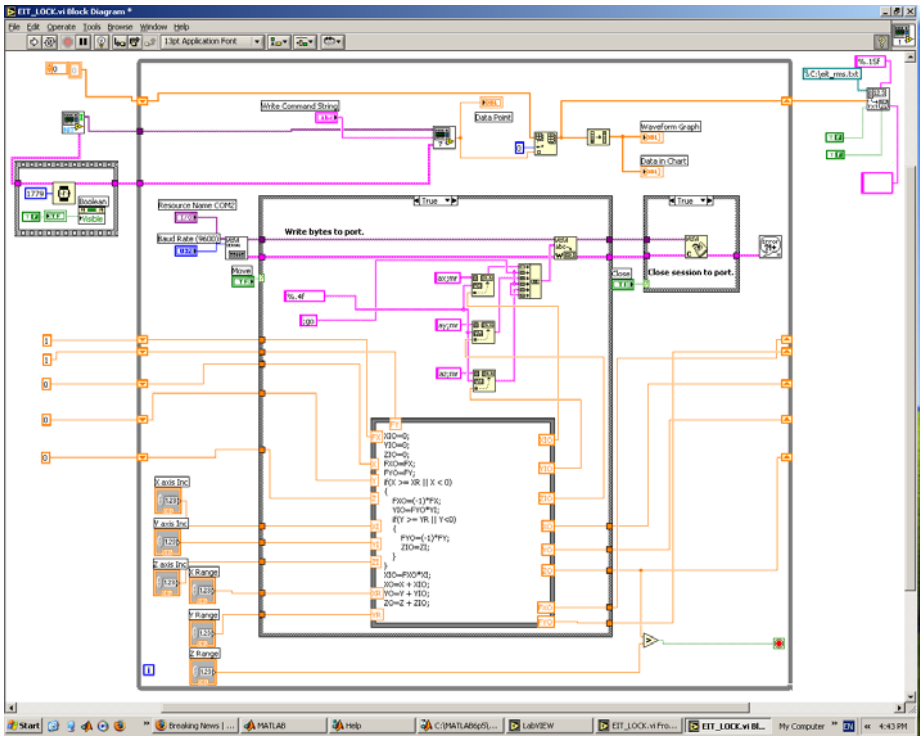

(b)

Figure 3.10: LabView program for the SII system
(a) Front panel layout. (b) Block diagram of the design.

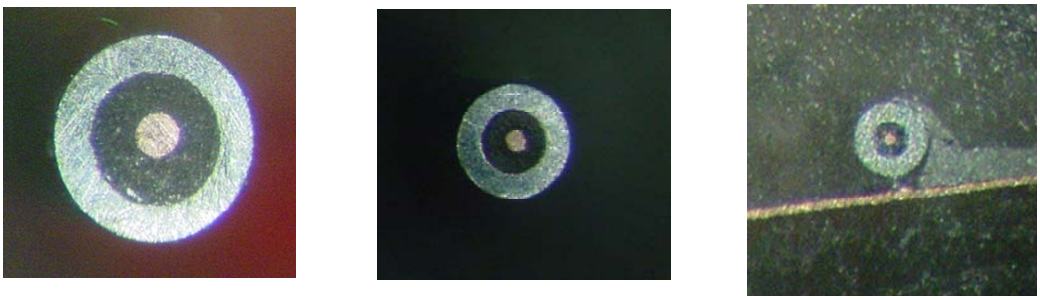

(a) (b) (c)

Figure 3.11: (a)180 μm tip diameter, 550 μm shield inner diameter;(b)100 μm tip diameter, 300 μm shield inner diameter;(c)30 μm tip diameter, 100 μm shield inner diameter

preventing unwanted current flux generated over the entire surface of the bottom conducting plane from being directed toward the inner conductor. The inner conductor called the "tip" of diameter D is separated from the outer conductor or "shield" by an insulator. The spacing between the tip and the shield is given by S_p as illustrated in Figure 3.5. When used in the imaging system illustrated in Figure 3.4, the resistor R ensures that the shield is at a higher voltage potential than the tip so that current flux to the tip can come only from an area beneath the probe of total diameter less than or equal to the tip diameter (D) plus twice the shield spacing (S_p). Small diameter shielded probes were constructed using insulated copper wire with metal diameters of 30, 100, and 180 microns. The wire is threaded into a stainless steel tube of inner diameters of 100, 300, and 550 microns respectively and embedded in non-conductive epoxy. The stainless steel tube serves as the shield and the metal core of the wire is the tip for the probes. The intention is to keep the diameter D equal to the shield spacing S_p as the probe sizes are scaled. Figure 3.11 shows digital photographs taken through an optical microscope showing the cross section of constructed probes.

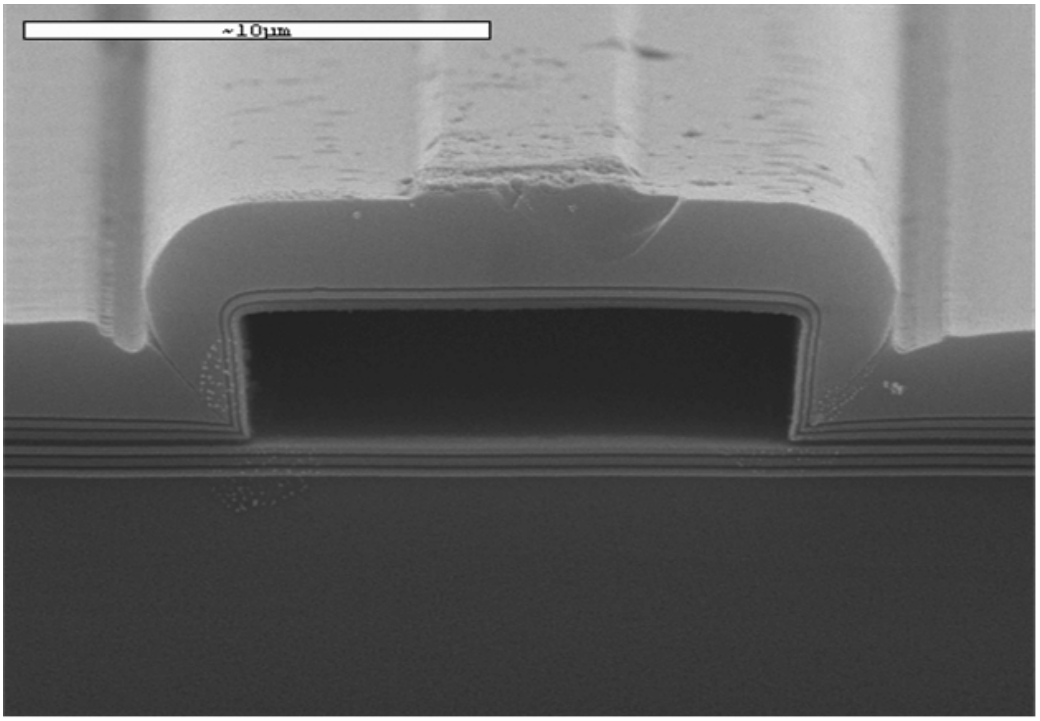

Figure 3.12: Scanning electron microscope picture shown the cross section of a hollow optical waveguide made at BYU using a procedure similar to that outlined in 3.13. In this case, however, a sacrificial layer was removed leaving a hollow core in the center of the structure.

Microprobe

Critical to making SII work on a scale capable of imaging at the cellular level, is the fabrication of the shielded probes in micron scales, which can be challenging. Micro-fabrication methods using clean room techniques are used here. The probe construction is based on the modification of a process currently used at BYU for the fabrication of hollow optical waveguides and fluid channels - an example of which is shown in Figure 10. In this process, a long metallic strip is surrounded by insulating materials and then removed with acid to produce a hollow core. In the production of microprobes, the same type of metal strip is surrounded by insulators, and then recoated in metal to form the shield for the microprobe.

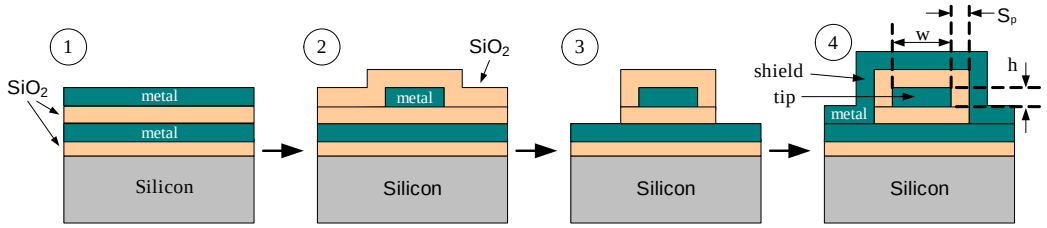

Figure 3.13: Processing flowchart for the construction of microprobes: 1. PECVD deposition of insulating layers (SiO_2) and evaporation of metal layers. 2. The top metal layer is patterned using lithography to define the tip dimensions then SiO_2 is deposited over the surface. 3. The SiO_2 is patterned using lithography to define the shield spacing. 4. Metal is coated over the surface to complete the outer shield.

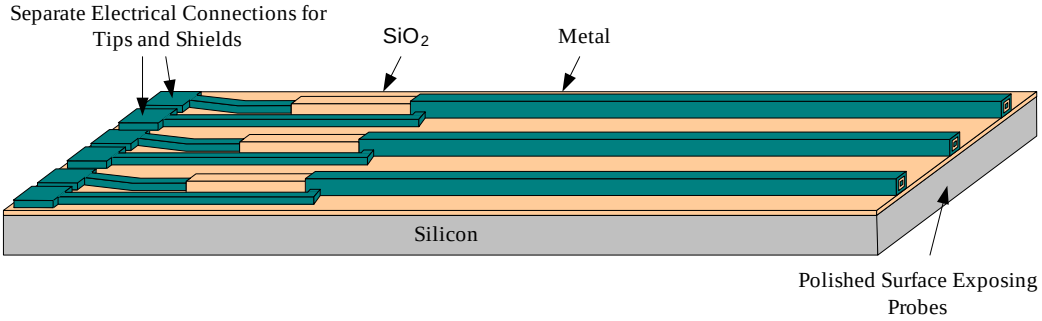

Figure 3.14: Illustration of several microprobes fabricated on a silicon substrate. The ends of the probes are formed by cleaving and then polishing the silicon - achieving a very flat surface. Separate connections to the probe tip and shield are made on the silicon using standard lithography and etch techniques.

The microprobe process is diagrammed in Figure 3.13. It begins with the deposition of alternating layers of silicon dioxide and metal on a silicon substrate. The top metal layer will determine the tip thickness (h). Various metal layers can be used including aluminum, gold, nickel, and tungsten. As part of the process development, several metals are used to find which produces the best probe geometries and impedance measurements. Thin metallic strips are then formed using standard photolithography techniques and metal etching determining our tip width (w). These metal strips are then coated in another insulating layer. This insulating layer is etched to define the shield separation, S_p, for the microprobe. A final metallic coating is applied over the insulator to form the outer shield. Using lithographic techniques,

very high precision features can be made and the dimensions h, w, and S_p varied simply by changing lithographic photomasks.

Upon completion of the deposition and etching steps described in Figure 3.13, the silicon wafer is cleaved perpendicular to the length of the microprobe and the cleaved surface polished. The tip, insulator, and shield are then exposed and this polished end is the one used in a solution to scan over a sample. Figure 3.14 illustrates three parallel microprobes on the same silicon substrate fabricated in parallel. The number of probes on a substrate could obviously be increased substantially with no increase in fabrication complexity. With multiple parallel microprobes, total scan times over a sample could be significantly decreased. Of course each microprobe would require separate connections to its metallic tip and its metallic shield. This is illustrated in Figure 3.14 with the connections ending simply in bonding pads at the edge of the silicon substrate.

Based on this process, some microprobes are made in the BYU Integrated Microfabrication Lab (IML). The diameter of the tip is down to 5 micron.

3.3 Alternative configuration for imaging setup

Besides the original setup of the SII system, another configuration was also implemented. The key difference is that the alternative setup seeks a way to measure the current through the tip without introducing the resistor R. Thus, the voltage of the tip keeps the same voltage as the voltage of the shield instead of a lower one. Figure 3.15 shows the diagram of the imaging system for this idea. The system is done by applying a known voltage to the base plane and simultaneously measuring

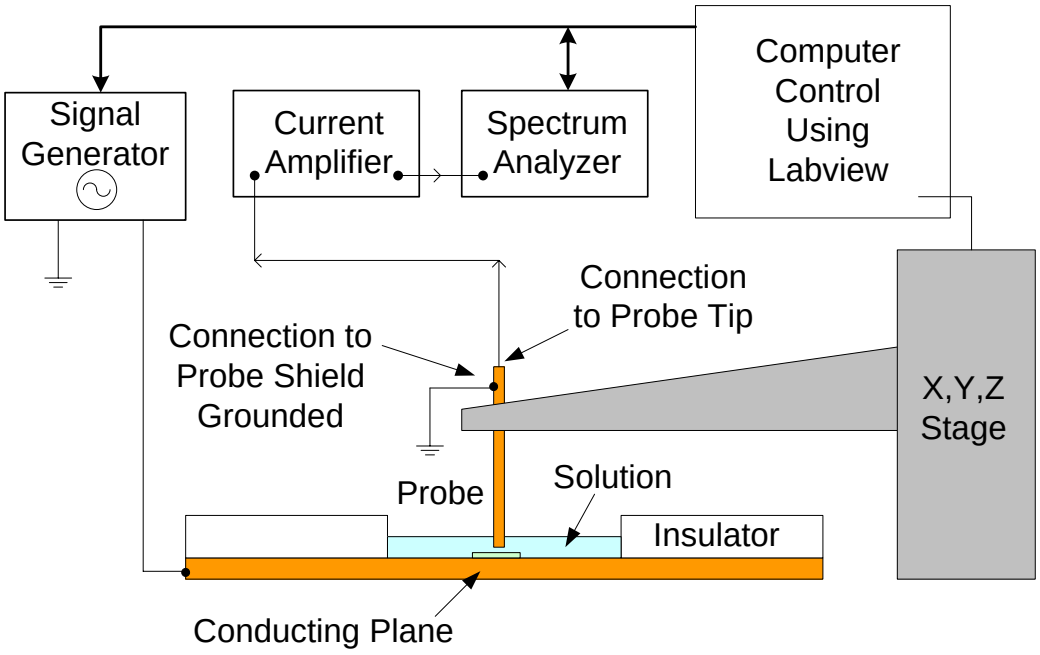

Figure 3.15: Alternative experimental configuration of SII system

the current flux into the probe. The current is buffered and amplified with a trans-impedance amplifier (Princeton Applied Research Model 181), then measured with a fast-Fourier transform spectrum analyzer (Stanford Research 760). Digital filtering in the spectrum analyzer eliminates the need for analog filter stages and results in a higher signal-to-noise ratio compared to data measured using an oscilloscope or voltmeter.

Figure 3.16 provides a clear view of the differences between two setups due to the use of a transimpedance current amplifier. Using this simple element has allowed for a dramatic improvement in measurement accuracy because it allows for the tip and the shield to always be biased at the same voltage - preventing current flow between them through the conducting water solution above a sample. Earlier system incarnations ground the conducting base plane, and apply bias to the tip and shield that have a resistor between them. Current through the tip is calculated from

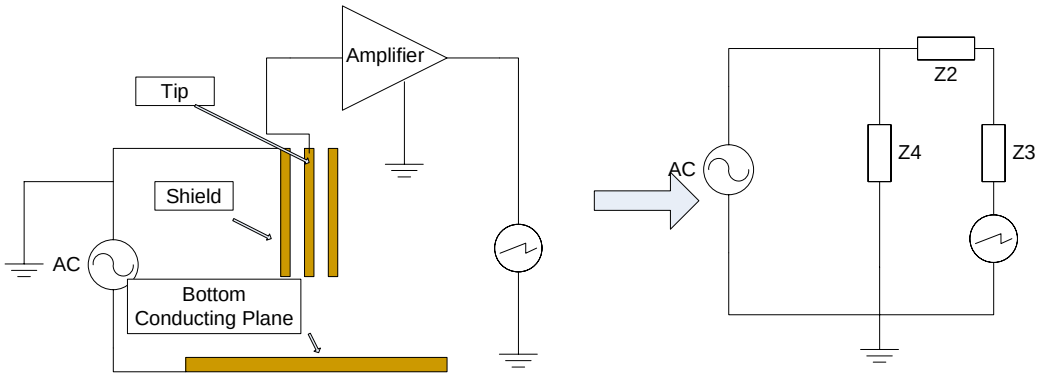

Figure 3.16: Equivalent circuit for the alternative setup shown in Figure 3.15. Z_2 is the equivalent impedance between the shield and the tip, Z_3 is the equivalent impedance between the tip and the ground-plane at each position, and Z_4 is the equivalent impedance between the shield and the ground-plane.

a measured voltage drop across this feedback resistor. This meant that the tip and shield are at different biases and the measured current is a combination of current due to the tip and shield bias difference and current due to the tip and bottom conducting plane bias difference, the latter being the current through the sample that is intended to measure. Determining the portion of the current only due to the sample is a very complex problem, given that the impedance between the tip and shield could vary with probe height and sample conductivity. Attempts are made to approximate this impedance or determine it by making multiple tests at different frequencies, but satisfactory accuracy is never obtained in this way. The setup shown in Figure 3.15 directly connects the shield to ground and the tip to the virtual ground created at the input of the current amplifier. Using this arrangement, the voltage on the tip is same as the one on the shield and both are fixed to zero. This results in less noise generated in the measurements. Further, all of the current flowing into the probe's tip is insured to arise only from the electric field applied between the tip and the conducting plane beneath the sample.

The disadvantages of this setup compared to the original one are higher complexity and non-grounding of the conducting plane. This non-grounding issue refers to the source voltage on the conducting plane that has a much larger area than the probe does. This could be a relatively larger source for other effects such as chemical effects.

3.4 Measurement strategy

Using the SII system, two types experiments are performed: 1-D line scan and 2-D image scan. A line scan is defined as a line profile scanned across in abrupt change conductivity in one horizontal direction. It is a simple test that is used to evaluate the performance of the SII system. Figure 3.17 illustrates a common setup for a line scan. A thin insulator is placed on top of the conducting plane in the imaging system. The probe is then inserted into the system and positioned above the insulator. The probe is then moved from a position directly over the insulator to one directly over the uncovered conducting plane in small scan increments with the current through the tip measured at each increment. The resulting line scan indicates the probe's ability to respond to the drastic change in impedance provided by the insulator. For very high resolution, a very sharp change in current would be expected at the abrupt junction created by the insulator. In order to quantify the resolution, the distance between the positions with 30% and 70% of the maximum current for the whole line scan is used to indicate the slope of the change for line scan. This distance, d_{res}, is shown on Figure 3.17. The smaller d_{res}, the better the resolution for a particular probe and scan condition. The automated XYZ stage allows for making line scan measurements at controlled variations of height above the insulator.

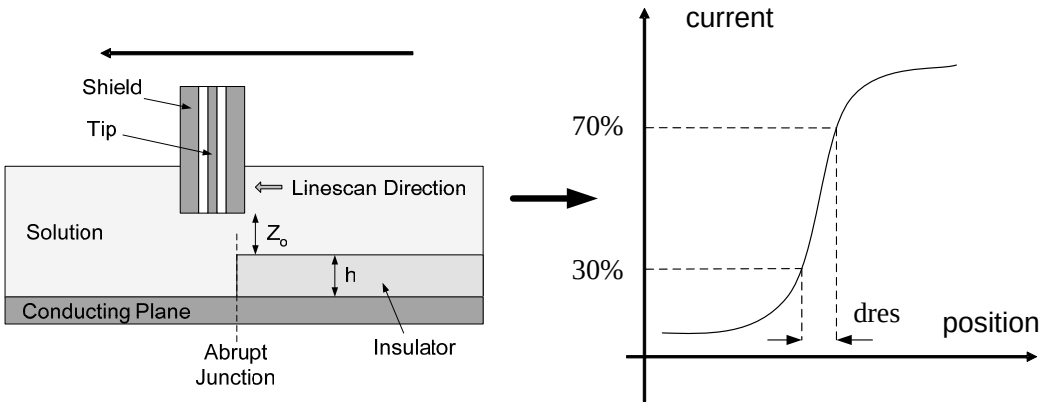

Figure 3.17: Illustration of line scan measurement used to characterize resolution in scanning impedance imaging system

A 2-D image scan is performed using s-scan in a horizontal plane. A 2-D image related to impedance distribution can be obtained for a thin sample. Each pixel of the image is the current measurement of a scanning position. The pixel resolution depends on the step size, usually 10 μm, 25 μm. As mentioned above, the image is not the exact impedance distribution due to the complex electric field there. However, this image can be considered as a coarse or blurred image of the exact impedance image.

Chapter 4

System modeling

In this chapter, an accurate 3-D numerical model for the forward problem to solve the current through the central tip with known conductivity distribution based on a finite-difference solution to the (quasi-)electrostatic field equations has been developed. This model can help illustrate the relationship between system parameters and measurements. It is also an important forward solution which is necessary to improve data resolution through image reconstruction. It has been also used to understand and improve the SII system design.

The basic numerical problem is to calculate the current flowing through the probe tip for a particular inhomogeneous sample between the probe and a conducting plane. The analysis requires the calculation of the electromagnetic fields between the probe and the conducting plane. However, the simple quasi-electrostatic calculation is complicated because the voltage on the tip and the current through the tip both vary depending on the driving circuit shown in Figure 3.4. Simply put, the model of the SII system is a quasi-statics problem involving inhomogeneous media with a complicated boundary condition. The modifier "quasi-" refers to the fact that the capacitance of the sample is considered through a complex-valued conductivity.

4.1 Electromagnetic background information

Using our measuring instrument a current map can be obtained at a particular distance above the sample. As mentioned above, the corresponding simple impedance image is a blurred image of the exact impedance distribution of the sample. The measurements take into account everything (no approximation, all field perturbations, noise, etc.) but do not provide details on the cause of impedance image blurring, or how to account for it. Thus, an important task is to develop a detailed physical model of the SII system to describe the relationship between the measured current and the exact impedance distribution. For a linearly-conductive material, a basic equation of the electrical field can be derived from Maxwell's equations (specifically Gauss's law and continuity of charge) and Ohm's law,

$$\bigtriangledown \cdot(\epsilon E) = -\frac{1}{j\omega} \bigtriangledown \cdot(\sigma' E) \tag{4.1}$$

where E is the electric field, ϵ is the permittivity of the material, σ' is the conductivity, and ω is the frequency. If introducing the complex conductivity as $\sigma = \sigma' + j\omega\epsilon$ then Equation (4.1) becomes

$$\bigtriangledown \cdot(\sigma E) = 0. \tag{4.2}$$

The electric and magnetic fields can be always written in terms of a scalar potential, ϕ, and a vector potential, A:

$$E = -\bigtriangledown \phi - j\omega A \tag{4.3}$$

and

$$B = \bigtriangledown \times A \tag{4.4}$$

where, $\bigtriangledown \cdot A$ can be arbitrarily chosen. When the wavelength of electromagnetic field is much longer than the dimensions of the experimental setup such as this case, it is common to ignore the small contribution from A and write $E = -\bigtriangledown \phi$. The fundamental equation for the potential inside the region of interest is therefore

$$\bigtriangledown \cdot(\sigma \bigtriangledown \phi) = 0. \tag{4.5}$$

Briefly, this equation specifies that no source resides in the body and that charge is not allowed to accumulate in the object.

For the completeness of the problem, the relationship of the voltage and current to ϕ must be established for the boundary conditions. Voltage is a path integral of electrical field:

$$V = -\int_P E \cdot dl = \int_P \bigtriangledown \phi \cdot dl = \phi. \tag{4.6}$$

The current density (including displacement current) is $J = \sigma E$ from Ohm's Law and the total current is an integral of current density over a surface,

$$I = \int_S J \cdot ds = -\int_S \sigma \bigtriangledown \phi \cdot \hat{n} ds \tag{4.7}$$

where $\hat{n}$ is a normal vector to the surface S.

The forward problem of the SII system is to simulate the current given conductivity distribution for scans. Figure 4.1 shows the diagram of the whole forward problem. For example, a 2-D image scan produces a 2-D current image. Each pixel in

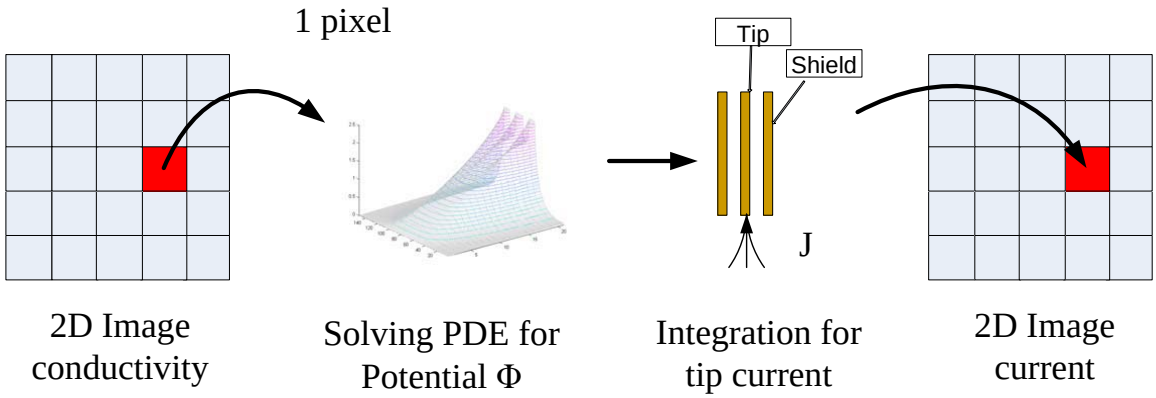

Figure 4.1: Diagram of the whole forward problem

this image corresponding a scan position leads to a setup of electric field in the region of interest. The electric field would change due to the boundary condition variation caused by moving the probe. Thus, each pixel in the current map results in a complete PDE (Equation (4.5)) problem solving the electric field. Hence, a 2-D 100×100 image scan consists of 10000 PDE problems that need to be solved with different boundary conditions. It can be noticed that this process requires huge computational resources both in time and memory storage.

4.2 Solution of the numerical problem

If the conductivity is known, the potential ϕ can be determined for all positions in the object by establishing the boundary conditions using known voltages and currents on the surface. Then, the current through the tip is an integral of the current density over the surface of the tip. Therefore, in order to find the current through the tip at each scanning position, solving the differential equation in Equation (4.5) for ϕ is demanded. The central purpose of this chapter is to construct a numerical method for solving this problem with acceptable precision and demonstrate how this

method can be used to illuminate how the probe is working and provide insight into improving probe design.

Since the sample of interest is inhomogeneous media and the ultimate micro-probe will be built with clean-room techniques that lead to an irregular shape of the probe, it is common to use Cartesian coordinates for the analysis of this problem. In three-dimensional Cartesian coordinates, the fundamental differential equation (Equation (4.5)) expands to

$$\frac{\partial}{\partial x}(\sigma\frac{\partial\phi}{\partial x}) + \frac{\partial}{\partial y}(\sigma\frac{\partial\phi}{\partial y}) + \frac{\partial}{\partial z}(\sigma\frac{\partial\phi}{\partial z}) = 0 \tag{4.8}$$

with $\nabla = \left(\frac{\partial}{\partial x}, \frac{\partial}{\partial y}, \frac{\partial}{\partial z}\right)$. It can be written in the following form,

$$\sum_{w=x,y,z} \frac{\partial}{\partial w}(\sigma\frac{\partial\phi}{\partial w}) = 0. \tag{4.9}$$

In order to solve this equation, the region of interest (including the sample and liquid) is broken into discrete points forming a rectangular mesh. Fig. 4.2 shows the details of one cube in the rectangular mesh. The complex conductivity σ is defined on a half-centered grid to the one ϕ is defined on. Using central differences the discretized equation becomes

$$\sum_{w=x,y,z} \frac{1}{\triangle w}\left\{\sigma_{w^+}\frac{\phi_{w^+}-\phi}{\triangle w} - \sigma_{w^-}\frac{\phi-\phi_{w^-}}{\triangle w}\right\} = 0, \tag{4.10}$$

or

$$\sum_{w=x,y,z} \frac{1}{\triangle w^2}\left\{\sigma_{w^-}\phi_{w^-} + \sigma_{w^+}\phi_{w^+} - (\sigma_{w^-}+\sigma_{w^+})\phi\right\} = 0, \tag{4.11}$$

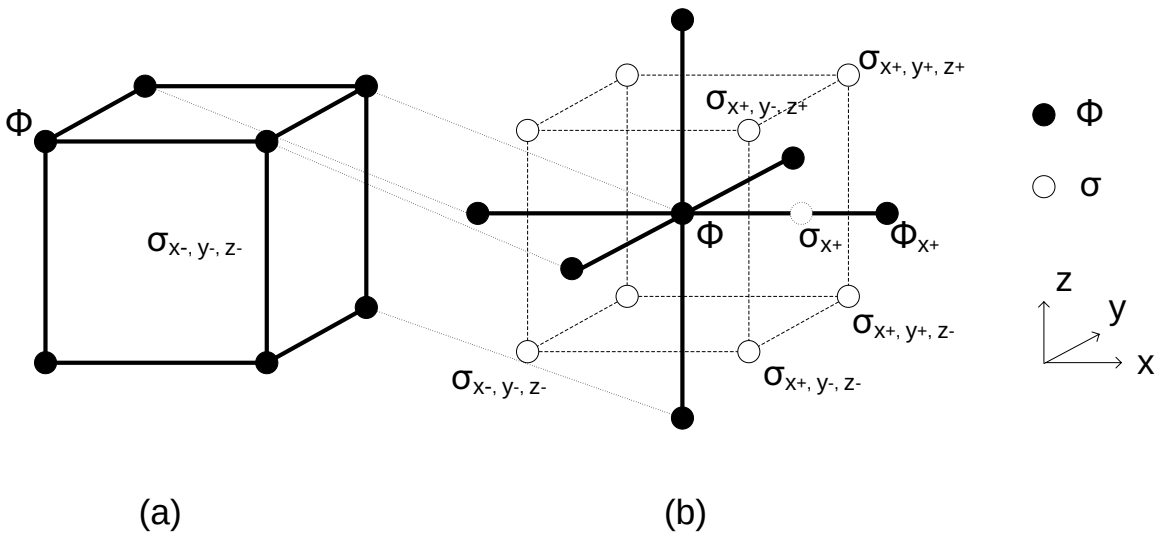

Figure 4.2: Diagram of the rectangular mesh

where the ghost point of conductivity $\sigma_{w^{\pm}}$ is an average of the four neighboring points. For example, Fig. 4.2 shows the ghost point σ_{x^+} in the x^+ direction which is calculated as

$$\sigma_{x^+} = \frac{1}{4}\left(\sigma_{x^+,y^-,z^+} + \sigma_{x^+,y^-,z^-} + \sigma_{x^+,y^+,z^-} + \sigma_{x^+,y^+,z^+}\right). \tag{4.12}$$

Basically, Equation (4.11) shows that the potential ϕ of a measured point (x, y, z), $\phi(x, y, z)$, is the conductivity-weighted average of its six adjacent points in three dimensions. According to the discrete approximations of the gradient and the integral, the discretized form of the current is

$$I = \sum \sigma_{z^-} \frac{\phi_z - \phi_{z^-}}{\triangle z} \triangle x \triangle y, \tag{4.13}$$

where assuming that the current through the tip flows along the z direction. Figure 4.3 shows the assumptions on the boundary conditions. The bottom conducting

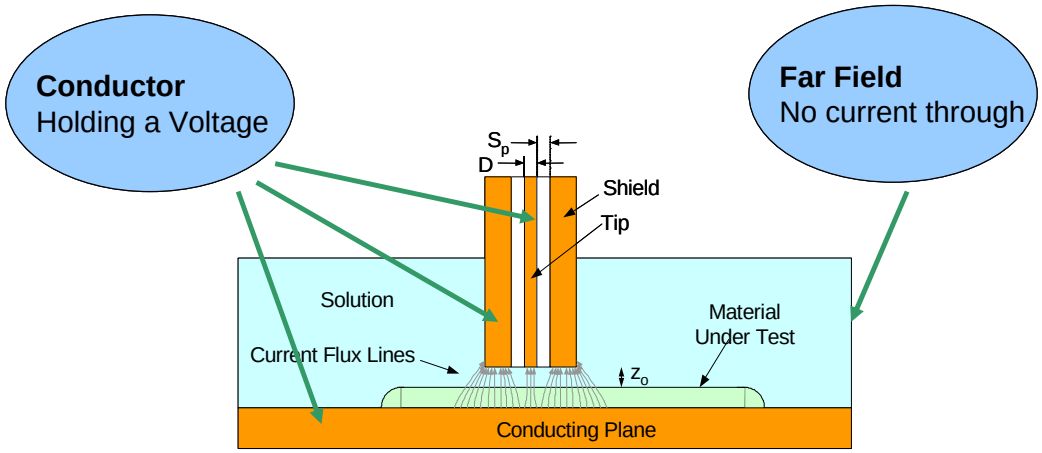

Figure 4.3: Boundary setup for the forward problem in the SII system

plane, the tip and the shield are conductors that can hold a specified voltage on the surface, while everywhere else, the assumption is that the electric field perpendicular to the surface is zero which means no current density through the surface (Neumann boundary condition). The voltages of the shield and the bottom conducting plane are known (Dirichlet boundary condition). However, the main setup with the resistor R shown in Figure 3.4 needs more attention to the boundary condition at the tip end because the voltage is determined by the relationship between the electrostatic field and the voltage drop introduced by R. By vectorizing the three dimensional arrays ϕ and σ, the full equation of this PDE problem is

$$\sum_j A_{ij}\phi_j + Rc_i I = b_i \tag{4.14}$$

where, R is the resistor in Figure 3.3 and I is the current through the central tip,

$$I = \sum_{j\in \text{tip}} \sigma_j^{z^-} \frac{\phi_j^z - \phi_j^{z^-}}{\triangle z} \triangle x \triangle y \doteq \sum_j d_j \phi_j. \tag{4.15}$$

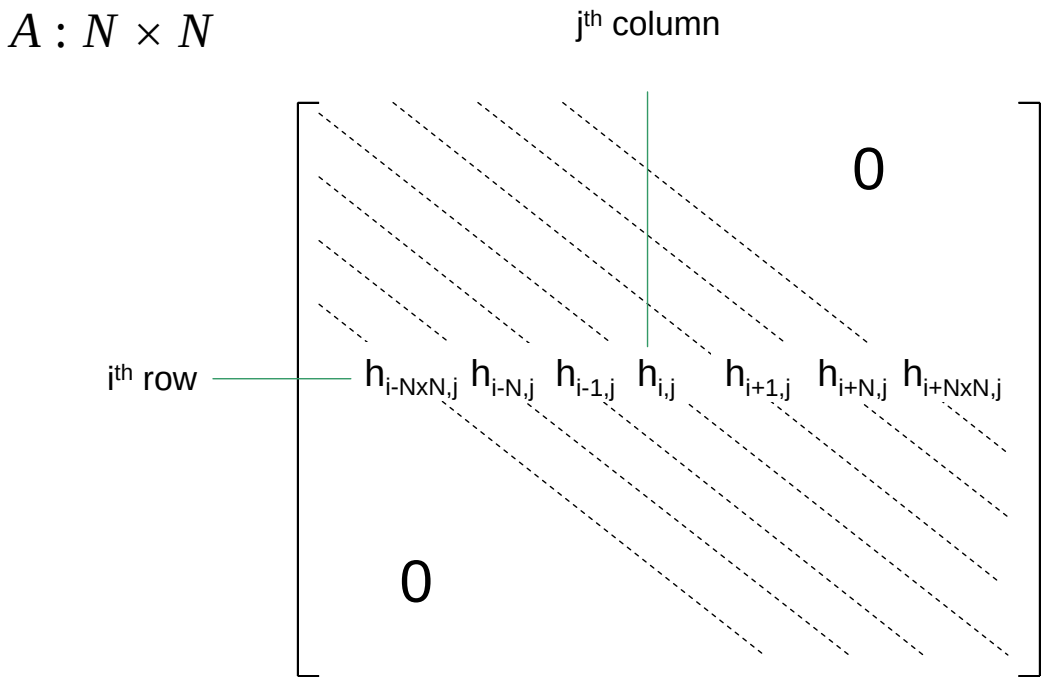

Figure 4.4: Components of the influence matrix A

Further derivations require the introduction of both a selective vector c_i with the definition,

$$c_i = \begin{cases} 1 & i \text{ on the tip} \\ 0 & \text{elsewhere} \end{cases},$$

and an influence matrix A with coefficients A_{ij} so that,

$$\sum_j A_{ij}\phi_j = \begin{cases} \sum_j h_{ij}\phi_j & \text{internal} \\ \frac{\phi_i - \phi_i^{w^-}}{\triangle w} & \text{Neumann condition} \\ \phi_i & \text{Dirichlet condition} \end{cases} \tag{4.16}$$

where $\sum_j h_{ij}\phi_j$ represents the left side of Equation (4.11). The influence matrix A is a huge sparse matrix with only seven diagonal elements, as shown in Figure 4.4. Also, b_i is a vector that describes the boundary condition,

$$b_i = \begin{cases} 0 & \text{internal} \\ 0 & \text{Neumann condition} \\ 0 & \text{bottom plane} \\ V_{\text{shield}} & \text{shield} \\ V_{\text{in}} & \text{tip} \end{cases}, \tag{4.17}$$

where V_{shield} and V_{in} are sources applied to the shield and the resistor R respectively. V_{shield} and V_{in} could be same, especially in experiments. From Equation (4.14) and (4.15), the matrix formulation for the SII system is:

$$\underbrace{\begin{bmatrix} A(\sigma) & Rc \\ d(\sigma)^T & -1 \end{bmatrix}}_{A'} \underbrace{\begin{bmatrix} \phi \\ I \end{bmatrix}}_{\phi'} = \underbrace{\begin{bmatrix} b \\ 0 \end{bmatrix}}_{b'}, \tag{4.18}$$

or

$$A'\phi' = b'. \tag{4.19}$$

Both the potential ϕ at each position and the current through the tip I can be obtained by directly solving Equation (4.18). Since A, c, d, and b are all sparse matrices, A' and b' are sparse too. It becomes the problem of solving a sparse linear system.

For the alternative setup shown in Figure 3.15, the full equation of the electrostatic problem corresponding to Equation (4.14) is

$$\sum_j A_{ij}\phi_j = b_i \tag{4.20}$$

and instead the current through the central tip I is

$$I = \sum_{j \in \text{tip}} \sigma_j^{z^-} \frac{\phi_j^{z^-} - \phi_j^z}{\triangle z} \triangle x \triangle y. \tag{4.21}$$

The influence matrix A is the same as the one of the main setup (Equation (4.16)) that consists of 7 diagonals of non-zero elements. However, b_i, representing the boundary condition is different due to the changes of the driving circuit,

$$b_i = \begin{cases} 0 & \text{internal} \\ 0 & \text{Neumann condition} \\ V_{\text{source}} & \text{bottom plane} \\ 0 & \text{shield} \\ 0 & \text{tip} \end{cases}, \tag{4.22}$$

where V_{source} is the driving voltage applied to the conducting plane. Thus, the matrix formulation for the alternative setup becomes

$$A\phi = b. \tag{4.23}$$

The potential ϕ can be obtained by solving Equation (4.23) and then the current I can be derived through Equation (4.21).

It can be seen that problems of both setups finally require solving a sparse linear equation. There are several iterative methods such as the generalized minimal residual method (GMRES) and the biconjugate gradient stabilized (BICGSTAB) algorithm that can solve these kinds of equations efficiently[80]. These algorithms are

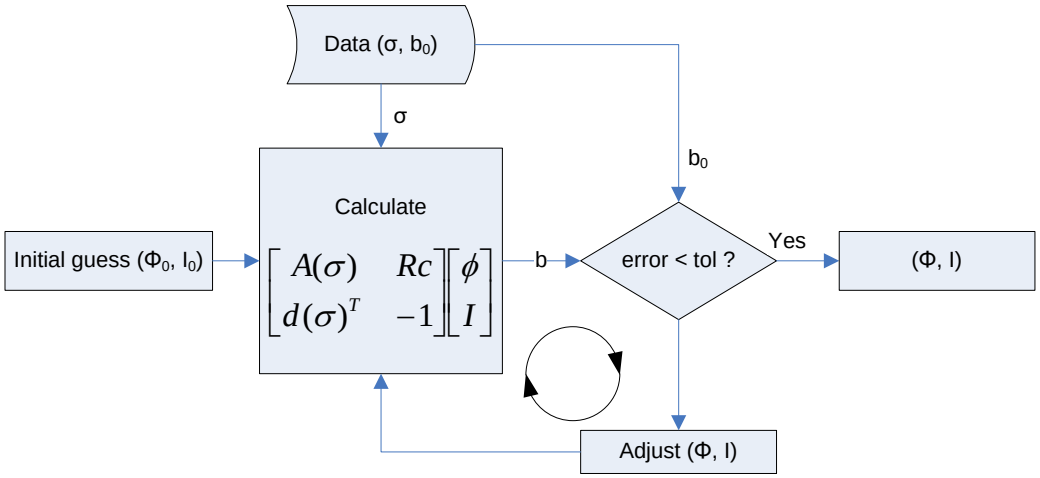

Figure 4.5: The framework of the iterative algorithms solving the forward problem of the SII system

numerical iterative methods and the process is shown in Figure 4.5. In order to save the memory storage, a function is derived to calculate the result of $A'\phi'$ directly rather than constructing A' and then multiplying A' with ϕ'. Since V_{shield}, V_{in} and σ are all complex numbers, complex variations of standard iterative algorithms have been developed to solve Equation(4.18) in the complex domain. It has been tested that both BICGSTAB and GMRES lead to good convergences.

4.3 Model verification

To verify the model, line-scanning experiments were performed using the SII system. In the experiments, the main configuration with the resistor R as shown in Figure 3.3 was used. A 20-μm thick mica slice was immersed in water of 10-kΩ-cm resistivity and used as a test object on a conducting (aluminum wafer) plane. A shielded probe (D=30μm) was used for the tests. The probe is known to be flat at a precision of $\pm$2.5μm A Newmark System Model NLS4-4-16 XYZ was used as

a stage controller to move the probe for scanning at increments down to 10μm. A 2.5-Volt peak-to-peak, 10kHz AC signal was used to drive the current through the probe with a 27-kΩ resistor R. The data was collected using a DSP lock-in amplifier (EG&G Instruments Model 7265). In an ideal impedance image of this test object, there should be an abrupt step-like change at the edge of the insulator. Thus, when the probe is moved from a position directly over the insulator to one directly over the uncovered conducting plane in small scan increments, a line profile of the current through the tip at each increment will be obtained with a large impedance step change at the edge. The slope of the change is a reasonable measure of the resolution of the impedance image.

This configuration was simulated at different frequencies that range from 1 kHz to 1 MHz. The results show that the frequency does not have a significant effect in either the signal-to-noise ratio or the resolution for this configuration. It is not surprising since the conductivity of water is much larger than the permittivity of water. This means that the imaginary parts of the complex numbers used in the equations are much smaller than the real parts even while increasing the frequency. Thus, 10 kHz was picked for the AC signal in the experiments to avoid the disturbance of the driving circuit. Due to the 3D FDM model, the imaginary part is too small under this frequency, even comparable to the tolerance. In order to reduce the time and the storage of simulations, it is common to ignore the small contributions of the imaginary parts and all the results were calculated in real numbers.

Figure 4.6 shows a line profile scanned from the insulator to the conducting plane at the height $Z_0 = 25\mu m$ along with a model fit simulated using the same conditions. The experimental data are currents through the tip calculated from RMS

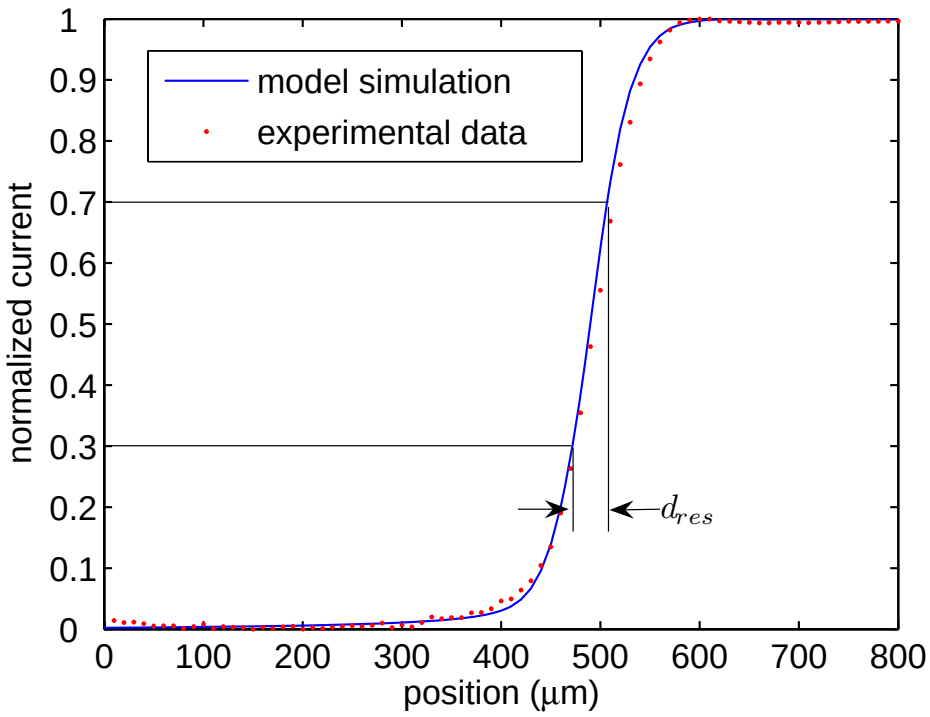

Figure 4.6: Measured results of line scans using a 30μm (tip diameter) probe and a 20μm thick mica slide for an insulator along with simulated results using the model under the same conditions.

voltages of the resistor R. Both curves are linearly scaled to lie between 0 and 1. As expected, current maximums occur when the probe is located over the conducting plane, while minimum values are achieved when the probe is over the insulator. Validation of the simulation model is evident in the excellent fit between the experimental data and the model.

A series of line plots similar to the one represented above were produced at different heights Z_0 using the same experimental setup. The distance, d_{res}, was used to quantify the resolution, as shown in Figure 4.6. Figure 4.7 shows the plot of d_{res} versus probe height Z_0. This provides insight of the relationship between the resolution and the probe height above the insulator. Both model simulation and the experimental data illustrate that the resolution improves when the probe is closer to

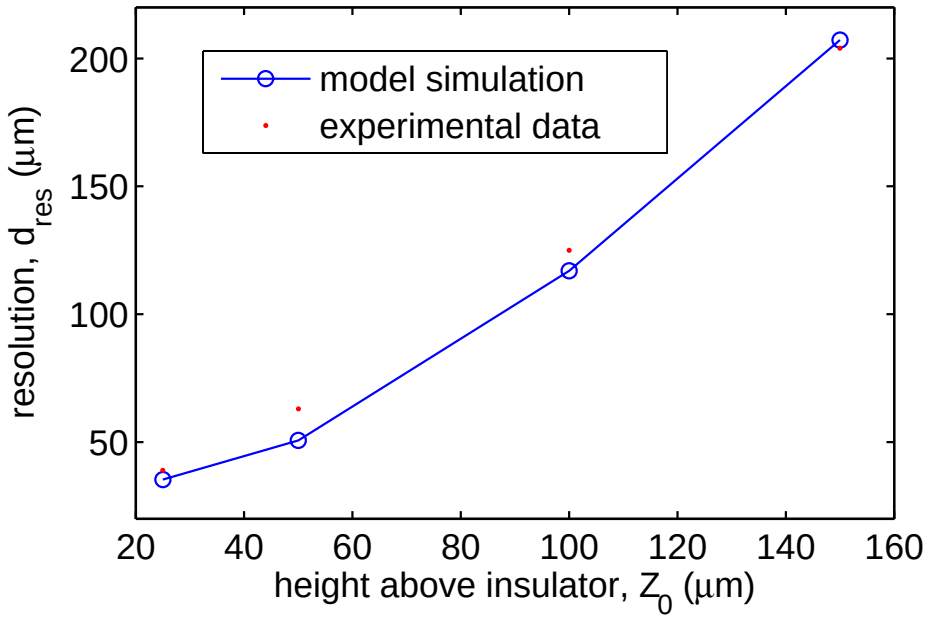

Figure 4.7: The resolution d_{res}, which is defined as the distance between the 30% and 70% of the maximum current difference versus the probe height Z_0 along with simulated results using the model under same conditions.

the insulator. That is not a surprising result because the effective cross-sectional area of the current flow shrinks hyperbolically to the area of the physical tip as the probe gets nearer to the sample. There is also a close fit between the measured data and the model for the trend of the resolution versus the height. The difference between the two curves can be attributed to the noise in the experiments and some quantization error of the numerical model due to grid discretization. These results confirm that scans should be performed with the probe as close as possible to the insulator for the best resolution.

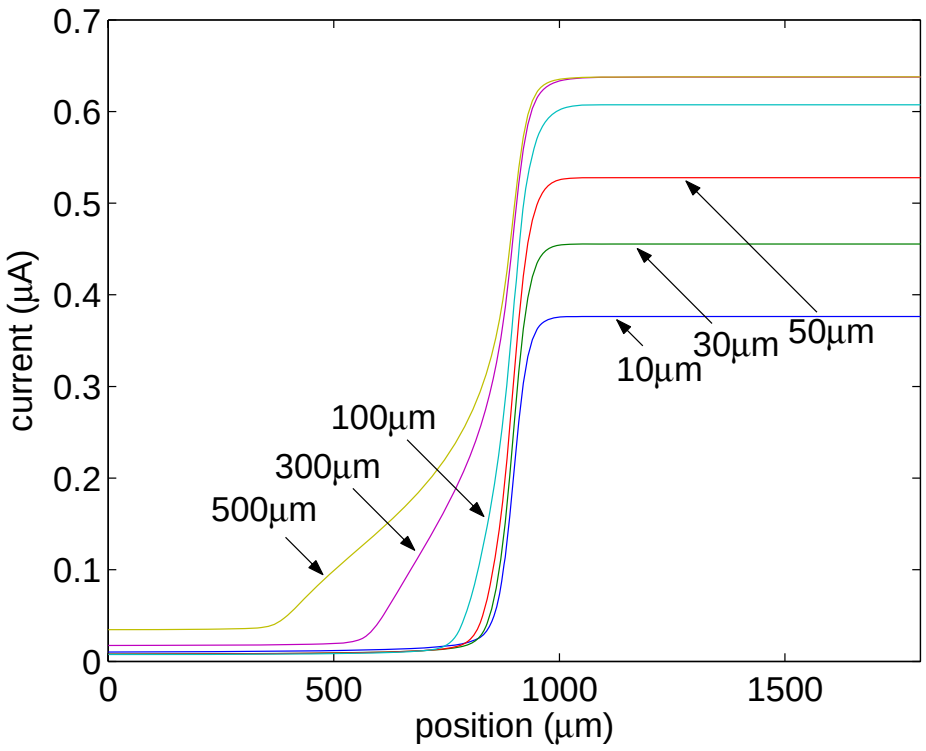

Figure 4.8: Simulated results of line scans for various shield-spacing using a 30μm (tip diameter) probe and a 20μm thick mica slide for an insulator.

4.4 Predictions using the model

Further exploration has also been done using this numerical model. Two important parameters, the spacing between the tip and the shield, S_p and the resistor R, have been analyzed from the model simulations for their effects on both the resolution and the signal-to-noise ratio. According to the simulation results, an optimum probe design can be predicted based on this numerical model.

4.4.1 Shield spacing prediction

Figure 4.8 shows the simulated line scans at different shield spacings (S_P=10μm, 30μm, 50μm, 100μm, 300μm, 500μm). These are the results simulated using a (D=30μm) probe with a fixed 30-μm shield thickness over a 20-μm thick mica slice. A source voltage of 2.5 Volt was applied to the shield directly and to the tip via a 100-kΩ resistor R. It can be seen in Figure 4.8 that the difference between the current maximum and the minimum becomes smaller when the shield spacing is decreased. At a given noise level, the difference between the maximum and the minimum is proportional to the signal-to-noise ratio. Because of the peripheral circuit setup, the voltage of the shield is always higher than the voltage on the tip, therefore, there are counteractive currents from the shield into the tip. The total amount of this counteractive current will be stronger when the shield spacing is smaller, which means the current through the tip will be smaller as well as the voltage across the resistor R.

Further, using the definition of the resolution as the 30%-70% distance, d_{res}, Figure 4.9 shows the simulated resolution d_{res} versus the shield spacing based on the results as shown in Figure 4.8. It can be observed that the resolution becomes better as the shield spacing is decreased. Thus, the effect of the shield on impedance measurements can be considered in two main aspects. One is the counteracting current from shield to tip with the negative effect on the signal-to-noise ratio mentioned above. The other is the concentration of the current flow through the tip that helps improve the resolution. According to the shield spacing results, it is not possible to obtain the best resolution and the best signal-to-noise ratio at same time according to the shield spacing results. Therefore, it is necessary to find a balance between them. The difficulty in fabricating the probe must also be considered. From these results

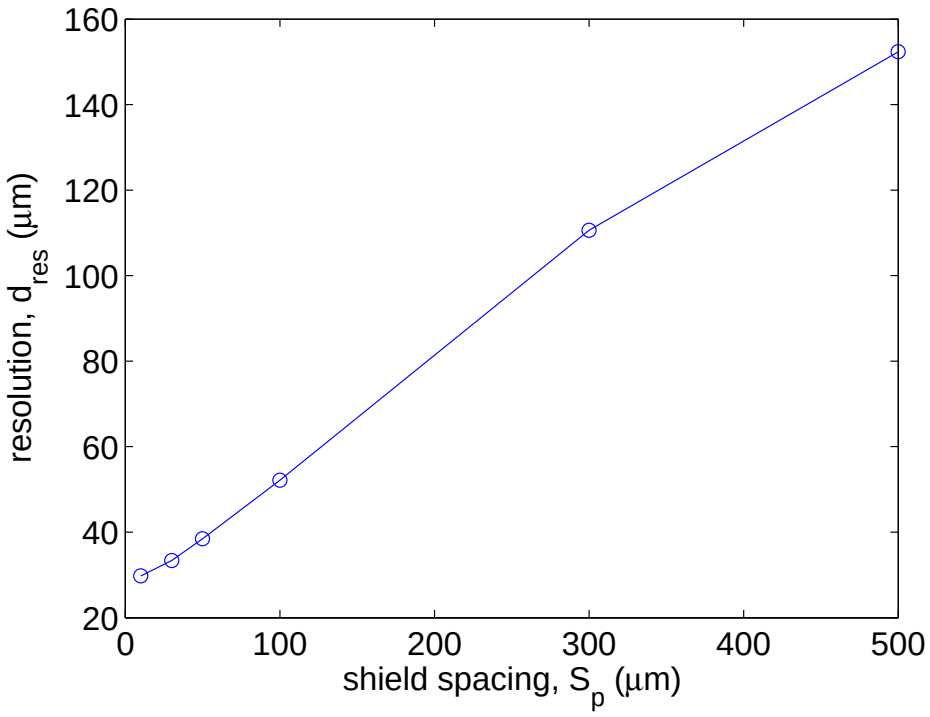

Figure 4.9: Simulated results of the resolution versus the shield-spacing S_p.

and techniques for the probe fabrication, a 100-μm shield spacing represents a probe that can be built consistently with a good trade-off between optimizing resolution and signal-to-noise ratio under this configuration. These simulation results have allowed an improved insight into the function of the shield in this probe design and why it provides better resolution and signal to noise ratios than an unshielded probe that can be imagined as $S_p \rightarrow \infty$.

4.4.2 Resistor R prediction

In addition to shield spacing, the resistor R was also altered with other configuration parameters fixed to investigate its relationship to the resolution and the signal-to-noise ratio. The resistor R was varied logarithmically between 1kΩ and

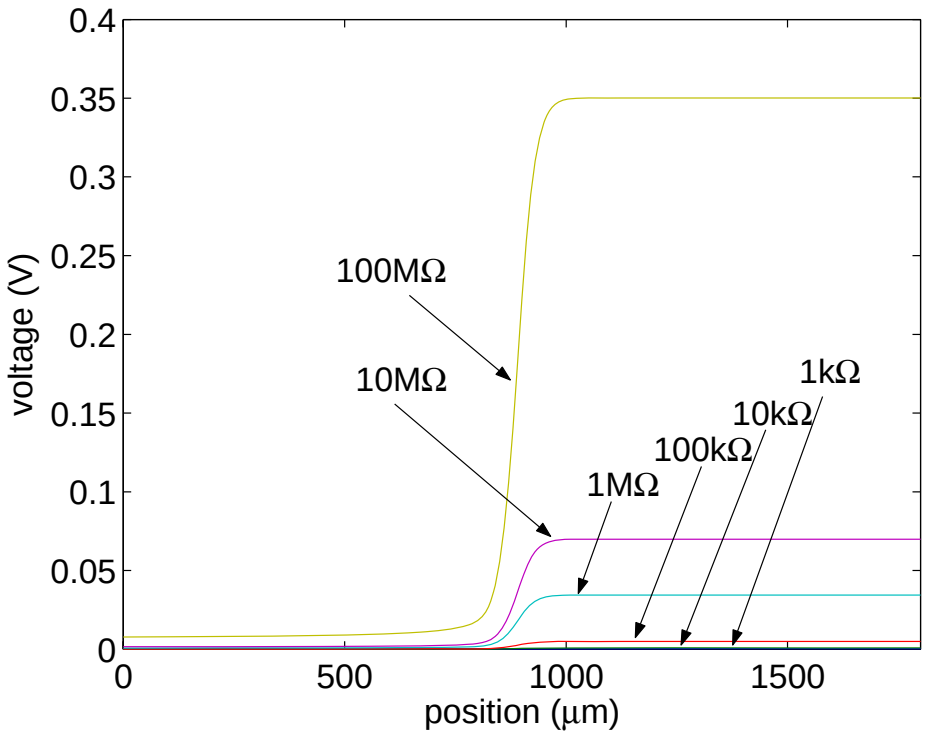

Figure 4.10: Simulated results of line scans for various resistor R using a 30μm (tip diameter) probe and a 20μm thick mica slide for an insulator.

100MΩ. A typical probe (D=30μm, S_p=30μm, 30-μm shield thickness) was used in these simulations and the water conductivity was changed to accelerate the simulations.

Figure 4.10 shows that the maximum of the voltage across the resistor R, which is the signal measured by the lock-in amplifier, is smaller when the resistance is smaller. However, the magnitude of the voltage does not scale linearly with the resistor, so the current through the resistor increases as the resistor gets smaller, even though the voltage decreases. Thus, a small resistor produces both a good signal-to-noise ratio and a low voltage signal difficult for measurement. Table 4.1 summarizes the maximum current for the various R. For each experiment, the resolution was approximately $d_{res} = 30\mu$m. Even though the different resistances vary the voltage

Table 4.1: Maximum current for various R resistors. The resolution obtained remained constant at 30 μm.

Resistor R	Maximum Current
1kΩ	0.2954μA
10kΩ	0.0838μA
100kΩ	0.0488μA
1MΩ	0.0344μA
10MΩ	0.0070μA
100MΩ	0.0035μA

difference between the shield and the tip, these simulations show that this does not have a significant effect on the resolution. Therefore, the optimum value of the resistor depends on the consideration for balancing signal-to-noise ratio and measurement error. Due to the complexity of the measuring environment and the diversity of the measuring objective, one could hardly provide an exact optimum value for all cases, 10kΩ-100kΩ is a good range for R in most cases.

Chapter 5

Impedance quantification using the 3-D FDM model

The 3-D FDM model developed in Chapter 4 provides not only the description of the electromagnetic field in the SII system but also the relationship between the measured current and the impedance distribution. This relationship could be applied to the reconstruction of the impedance distribution from the measured currents. It can be noticed that this reconstruction is a complex inverse problem by recalling the Equation (4.7) and (4.5). There are two facts that need to be considered in this reconstruction.

1. **Value-transform:** (quantitative issue) the value we measured is current that is not directly related to the impedance in the SII system. In other words, the impedance cannot be obtained from the measured current using only the Ohm's Law.

2. **Blurring:** (resolution issue) the measured current integrates the impedance distribution in a small region under the probe, which leads to the "blurring effect" of measured current images.

These two issues interact each other and both are necessary for the reconstruction of impedance images. However, for thin-sample testing experiments, the quantitative issue can be solved separately under some assumptions. In this chapter, with the help of the 3-D FDM model, a simple extraction of exact impedance values could be achieved without solving the full inverse problem of both two issues. This simple extraction is based on the fact of the current confinement introduced by the shielded-probe design. The 3-D FDM model confirms that current flow to the probe is confined within a cylinder directly below the probe. Thus, it is almost true that the blurring effect is limited with the shielded-probe design in the thin-sample testing experiments. When this limitation is valid, the average value of the impedance in the cylinder directly below the probe can be considered as a good estimation of the quantitative value of the impedance at the position of the probe. As mentioned in previous chapters, due to the low frequency source used in the SII system, only resistivity is considered in this section with the trivial capacity ignored. The first part of this chapter describes the probe confinement using numerical modeling based on the 3-D FDM model. The next part describes how resistivity values can be computed from SII measurements given the current confining properties of the probe based on the numerical model. Measurements of known saline solutions are provided to confirm the accuracy of the computed resistivity values. The final part provides quantitative 2-D resistivity scans for three different material systems and also shows the significance and limitations of this method.

The simple extraction shown in this chapter provides the ability to determine the actual resistivity of a sample that enables the comparisons between different samples rather than simply a relative measurement within a single sample. Furthermore, a more quantitative measurement produces useful information for analyzing biologi-

cal samples that exhibit a range of resistivity values rather than simply an interface between conductive and insulating regions. However, as mentioned above, this simple extraction is not a full solution to our problem since it evades the consideration of the blurring issue. A more thorough exploration will be discussed in the next chapter.

All the results in this chapter were obtained using the alternative setup for the SII system as shown in Figure 3.15. This configuration provides knowledge of the voltage of the tip by eliminating the resistor in the original setup that could harm the quantitative process. The instruments used in all the experiments in this chapter are listed as follows,

- Trans-impedance amplifier (Model: Princeton Applied Research 181),
- Fast-Fourier transform spectrum analyzer (Model: Stanford Research 760),
- Linear XYZ stage (Model: Newmark Systems NLS 4-4-16).

Digital filtering in the spectrum analyzer eliminates the need for analog filter stages and results in a higher signal-to-noise ratio compared to data measured using an oscilloscope or voltmeter. As illustrated in Figure 3.15, a sinusoidal voltage is applied across the sample as opposed to a DC voltage. The AC measurement suppresses hydrolysis in the water below the impedance probe. The experimental results presented in this chapter were obtained using a 60 kHz signal of amplitude 1 V peak-to-peak. In practice, it has been determined that resistivity measurements are independent of signal amplitude for a voltage range between 0.1 and 10 V peak-to-peak.

The probe used in the experiments employed the shield design as shown in Figure 3.5. In practice, impedance probes are made by inserting insulated copper

wire into stainless steel syringe needles filled with an insulating epoxy. The tip of the needle is then ground flat and electrical connections are made to the copper wire, which serves as a probe's tip, and to the syringe, which serves as the shield. The measurements shown in this chapter used 38 gauge copper wire and 23 gauge syringe needles to create probes with approximately D=100 μm tip diameter, and S_p=100 μm spacing between the tip and the shield.

5.1 Current confinement using shielded probes

As stated in Chapter 3, the primary motive for the shielded design of the SII impedance probe is the confinement of current within a known volume, which provides a hardware improvement of image resolution. In the alternative configuration of the SII system, the shield is connected to ground and the tip is connected to the virtual ground created at the input of the current amplifier. Using this arrangement, all of the current flowing into the probe's tip is insured to arise only from the electric field applied between the tip and the conducting plane beneath the sample. Using the 3-D FDM model developed in Chapter 4, more details can be provided for the current flow under the probe and are critical in calculating sample resistivity. A simulation was performed using the model and the system was configured as stated above. The result is shown in Figure 5.1. The stream lines were generated by solving for the electric field in the region below a probe and then tracing current flow from the conducting plane below a sample toward either the tip or shield electrodes. This particular simulation assumed there was a sample 100 μm high sitting on the bottom conducting plane, with 100 μm of a conducting solution between the sample and probe as shown in Figure5.2. The sample was assumed to be less conductive than the solution, with a

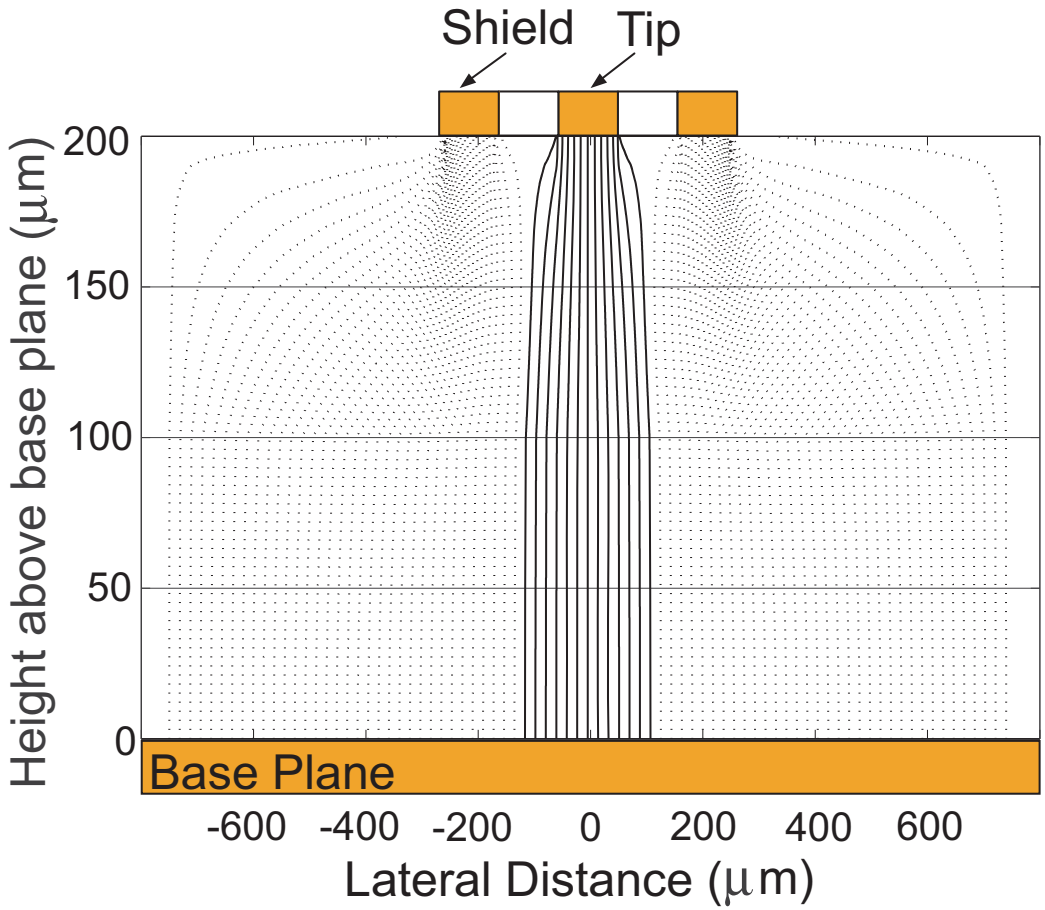

Figure 5.1: Current flow lines from conducting base plane into the tip and shield of an SII probe. This is a 2-D cross section taken from a 3-D simulation. The dark lines represent current flowing into the tip while the light lines represent current flowing into the shield. Simulation represents a high conductivity solution over a 100 μm thick sample. Conductivity ratio for sample to solution is 1:10

conductivity ratio of 1:10. The full simulation is done in three dimensions with Figure 5.1 only showing a 2-D cross section. The dark lines indicate current flowing from the bottom plane toward the tip, while the lighter lines indicate current flowing into the shield electrode. Readily apparent in Figure 5.1 is that the current flowing toward the tip is confined to a cylindrical volume directly below the tip. The diameter of this cylinder is approximately the midway point between the tip and the shield or

$$D_{\text{eff}} = D + S_p, \tag{5.1}$$

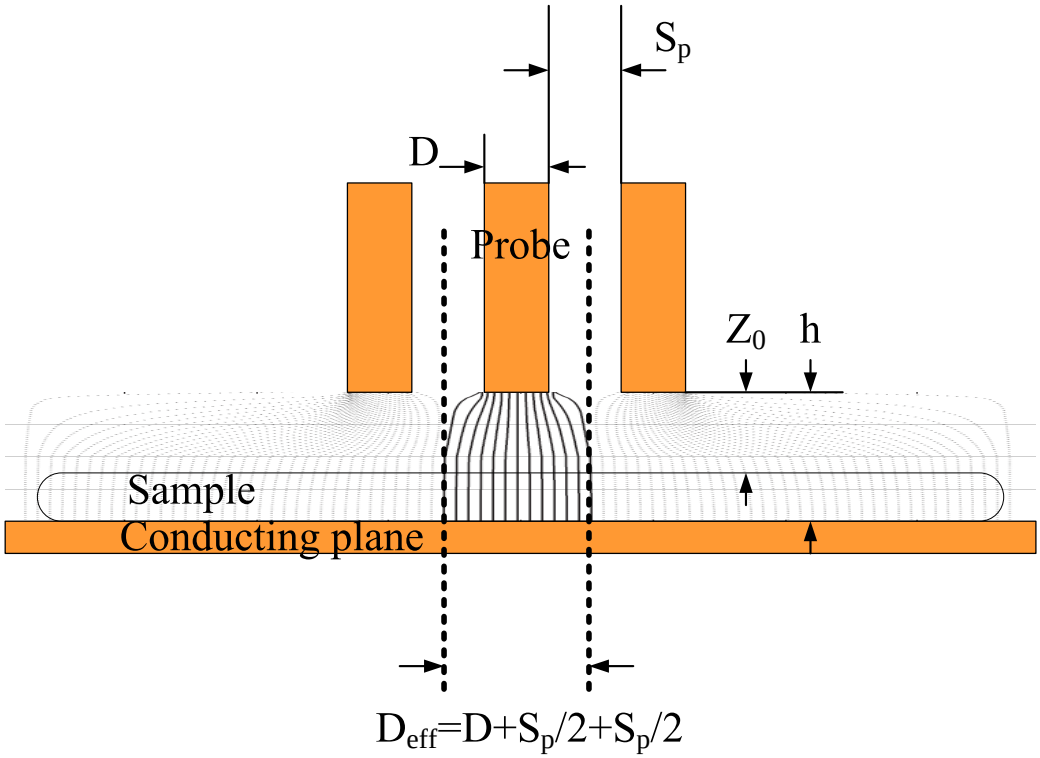

Figure 5.2: Illustration of the current confinement and definitions of D, S_p, Z_0, and h

as shown in Figure 5.2.

Simulations were also run for homogeneous media (corresponding to a situation where only water of a constant conductivity is between the probe and conducting plane) and for other heterogeneous cases (corresponding to water placed over a sample with different conductivity). In each case, the diameter D_{eff} of the current confining cylinder remained approximately equal to the quantity given by Equation (5.1). The implication of this result is very significant. The tip collects current from a confined volume between it and the bottom conductive plane when the shield design is employed.

5.2 Extracting resistivity values

The resistance between the probe and the conducting plane can be obtained from Ohm's Law,

$$R_{\text{meas}} = \frac{1}{G_{\text{meas}}} = \frac{V}{I_{\text{meas}}}, \tag{5.2}$$

where V is the known voltage applied at the bottom conducting plane and I_{meas} is the current that is injected into and then amplified by the transimpedance amplifier. The Ohm's Law does not provide the details of the electromagnetic field inside and only the whole resistance of a certain part of the sample can be obtained using this simple formula. Thus, this quantitative process has no efforts on the image reconstruction. Nonetheless, extracting a good estimation of the resistivity of the sample is still possible from this general start. From the theorectical analysis in the Chapter 4 and the fact of the confinement shown in the previous section, the measured current through the tip, I_{meas} can be written as

$$I_{\text{meas}} = \int_{A_{\text{eff}}} Jds \Big|_{z=0} = \int_{A_{\text{eff}}} \sigma E ds \Big|_{z=0} \tag{5.3}$$

where A_{eff} is the cross-section area of the current confining cylinder and J is the current density near the bottom conducting plane. The diameter of A_{eff} is D_{eff},

$$A_{\text{eff}} = \pi \left(\frac{D_{\text{eff}}}{2} \right)^2 = \pi \left(\frac{D + S_p}{2} \right)^2. \tag{5.4}$$

σ is the conductivity and E is the electric field. Thus, the relationship between the conductivity σ and the measured resistance R_{meas} can be obtained,

$$R_{\text{meas}} = \frac{V}{I_{\text{meas}}} = \frac{V}{\int_{A_{\text{eff}}} \sigma E ds\Big|_{z=0}} \tag{5.5}$$

or

$$G_{\text{meas}} = \frac{1}{V} \int_{A_{\text{eff}}} \sigma E ds\Big|_{z=0}. \tag{5.6}$$

By observing the current flow under the probe, it is possible to make a useful assumption that the electric field is not significantly different from the one of the two infinite plate capacitor with homogeneous media in the middle if the conductivity of the sample does not vary too much. In formula, the assumption is

$$E = \frac{V}{h} \tag{5.7}$$

where h is the distance between the probe end and the bottom conducting plane. As a corollary, the electric field E is uniform in the cylinder. Thus, Equation 5.6 can be written as

$$G_{\text{meas}} = \frac{1}{V} E \int_{A_{\text{eff}}} \sigma ds\Big|_{z=0} = \frac{1}{h} \left(\sigma_{\text{aver}} A_{\text{eff}}\right)$$

where σ_{aver} is the average value of the conductivity near the bottom plane inside the small cylinder, which is the average conductivity of the sample in the cylinder in thin-sample cases. Therefore, quantitative average values of the conductivity distribution can be restored from the measured current or resistence

$$\sigma_{\text{aver}} = \frac{h}{R_{\text{meas}} A_{\text{eff}}}.$$

If the conductivity σ is replaced by the resistivity $\rho = \frac{1}{\sigma}$, then the equation can be written as

$$\rho_{\text{aver}} = \frac{R_{\text{meas}} A_{\text{eff}}}{h}. \tag{5.8}$$

Equation (5.8) shows that an average of the resistivity in a cylinder right under the probe can be obtained if A_{eff} and h are known. The diameter of the cylinder is D_{eff} which is almost twice of the diameter of the tip since the shield spacing and the tip diameter are equal for most probes used in experiments. Thus, every pixel in the image of the average resistivity ρ_{aver} is no larger than a circle area with a diameter of $2 \times D$. Since the cylinder is too small when compared to the sample (the whole image size) and it is comparable to the scanning step size (pixel size), the image can be considered as a good estimated image of the real resistivity of the sample. Although there is no improvement in image resolution when using this simple extraction, the shielded-probe design guarantees that a good image resolution can be expected for the image of resistivity.

To determine the value of the average resistivity ρ_{aver} using Equation (5.8), R_{meas}, A_{eff} and h must be known. R_{meas} can be obtained from the measured current using Equation (5.2). h is the probe height shown in Figure 5.2 which could potentially be measured. A_{eff} is the key value that need further consideration. Although simulations have shown that A_{eff} is invariant in both homogeneous case and other heterogeneous cases, it is possible for A_{eff} to be a function of h, though there is no explicit relationship between them shown in the theoretical analysis. Therefore, simulations were run for the demonstration of this possible relationship and the results are shown in Figure 5.3. The effects of the shield on the probe design are also illustrated in this figure. This figure shows the simulation results using the FDM model

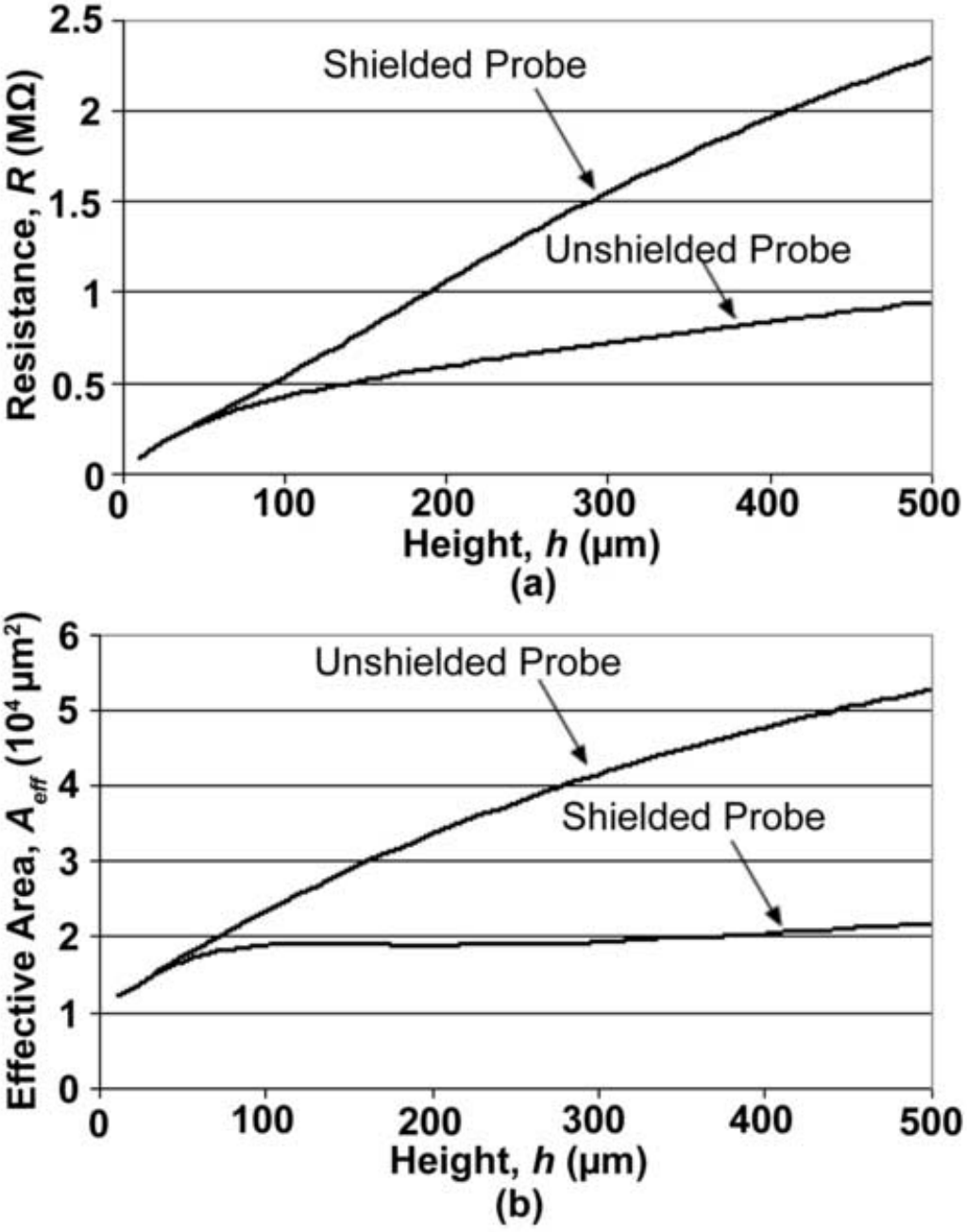

Figure 5.3: (a) Calculated resistance between the tip and the base plane using a shielded and unshielded probe. (b) The effective area, found by dividing the resistivity times sample height by the resistance from part (a)

comparing a shielded probe to an unshielded one. The unshielded case consisting of simply a center electrode surrounded by an insulator (no outer shield electrode).

Figure 5.3 (a) compares the simulated resistance as R_{meas} as a function of probe height h in a homogeneous solution of conductivity σ=0.01 S/m. The probe geometries were D= 100 μm, and S_p= 100 μm. Resistance is determined by dividing the voltage drop across the sample V by the current through the probe tip I_{meas}, as shown in Equation (5.2). Integrating J over the tip surface easily approximates the tip current. It can be seen that the curve for the shielded probe is nearly linear as height above the sample increases. This is due to the fact that the shield limits the effective diameter of the cylindrical volume contributing to tip current and the total resistance increases linearly as the cylinder's volume increases linearly. The unshielded case is nonlinear because the effective probe area increases with height, h.

The effect of the shielded probe is also demonstrated in Figure 5.3 (b). In this figure, the total resistance computed in Figure 5.3 (a) is used together with Equation (5.8) to obtain A_{eff},

$$A_{\text{eff}} = \frac{\rho_{\text{aver}} h}{R_{\text{meas}}}. \tag{5.9}$$

Figure 5.3 (b) plots $\rho_{\text{meas}} h/R$ to determine whether the area A_{eff} remains constant as h increases so that ρ_{aver} can be obtained from Equation (5.8). As shown in the figure, for the unshielded case $\rho_{\text{meas}} h/R$ continues to increase with h, indicating that current is being drawn from a volume with a changing cross-sectional area and Equation (5.4) will not hold for this case. For the shielded case, however, above 80 μm, $\rho_{\text{meas}} h/R$ (area) remains approximately constant, indicting that Equation (5.4) does accurately describe the resistance relationship for this volume.

The simulation results indicate that a shielded probe is able to confine current not only to a confined volume, but specifically to a cylindrical volume with a nearly constant cross sectional area. This allows total resistance to be related to sample resistivity in the simplest possible way using Equation (5.8). Extensions of the model for heights greater than h= 500 μm (for a D= 100 μm and $S_p = 100$ μm probe), show that gradually current confinement begins to break down and the cross sectional area of the confinement volume no longer remains constant. This still provides a large range of heights, h, where the constant area approximation is valid.

5.3 Modification for practical experiments

It would be ideal to relate measurement data to the physical parameter resistivity in order to classify or compare material compositions. The modeling results discussed earlier establish a theoretical basis for using the simple relationship given in Equation (5.8) to relate resisitivity to the probe area given by Equation (5.4), and the sample resistance R_{sample} given in Equation (5.2). For real samples, however, even if the height of the probe above the bottom conducting plane, h, is known, the actual thickness of the sample ($Z_0 - h$) may vary along the samples area (h and Z_0 are defined in Figure). The total resistance R_{sample} will actually consist of a resistance due to the material under test and the water between this material and the probe. Since, the height of the sample will not always necessarily be known, we will report the quantity (resistivity) $\times$ height as a quantitative measure, given by

$$\rho_{\text{aver}} h = R_{\text{sample}} A_{\text{eff}}. \tag{5.10}$$

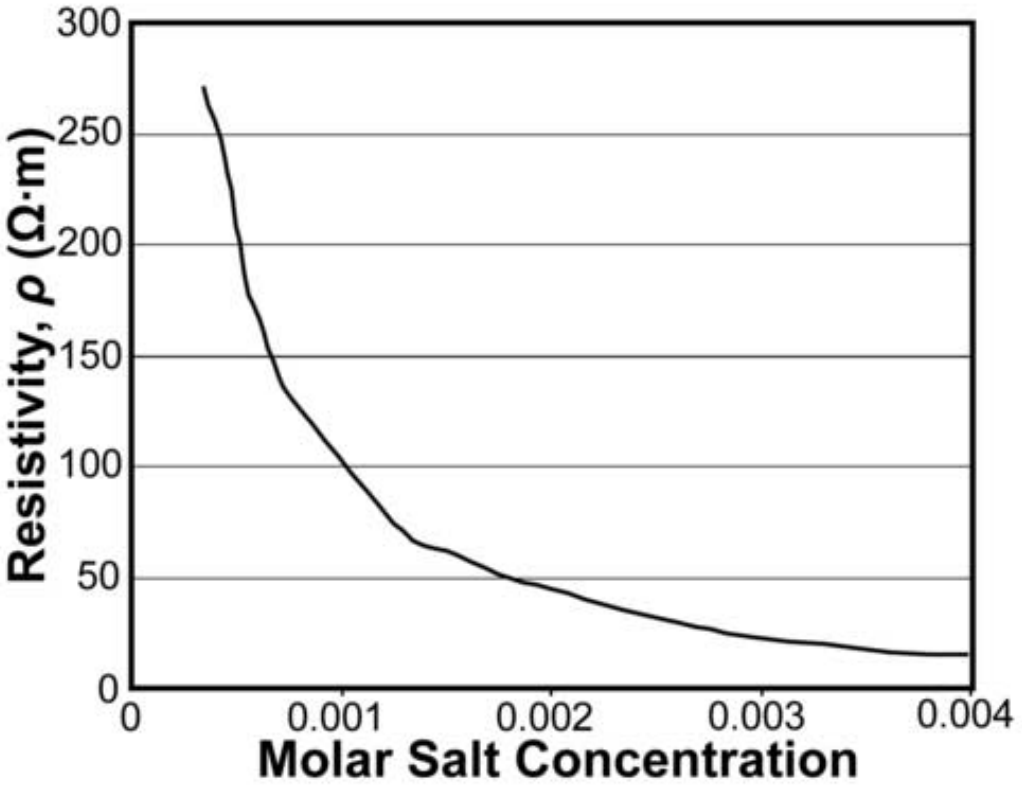

Figure 5.4: Resistivity of saline solution versus molar concentration of NaCl

If sample height is well known, the $\rho_{\text{aver}}h$ quantity can easily be divided by h to yield an absolute material resistivity. This is complicated somewhat by the fact that there is also a conductive water solution between the probe and the sample, but under certain test conditions this can be dealt with as discussed in the next section.

To demonstrate how this $\rho_{\text{aver}}h$ quantity will be used and to experimentally verify the FDM modeling results, a series of scans were performed for the simplest possible test case - homogeneous saline solutions. The experiments in this chapter were performed using the alternative setup of SII with a spectrum analyzer shown in Chapter 3. Resistivity versus NaCl concentration was measured using a commercial resistivity meter with the results shown in Figure 5.4.

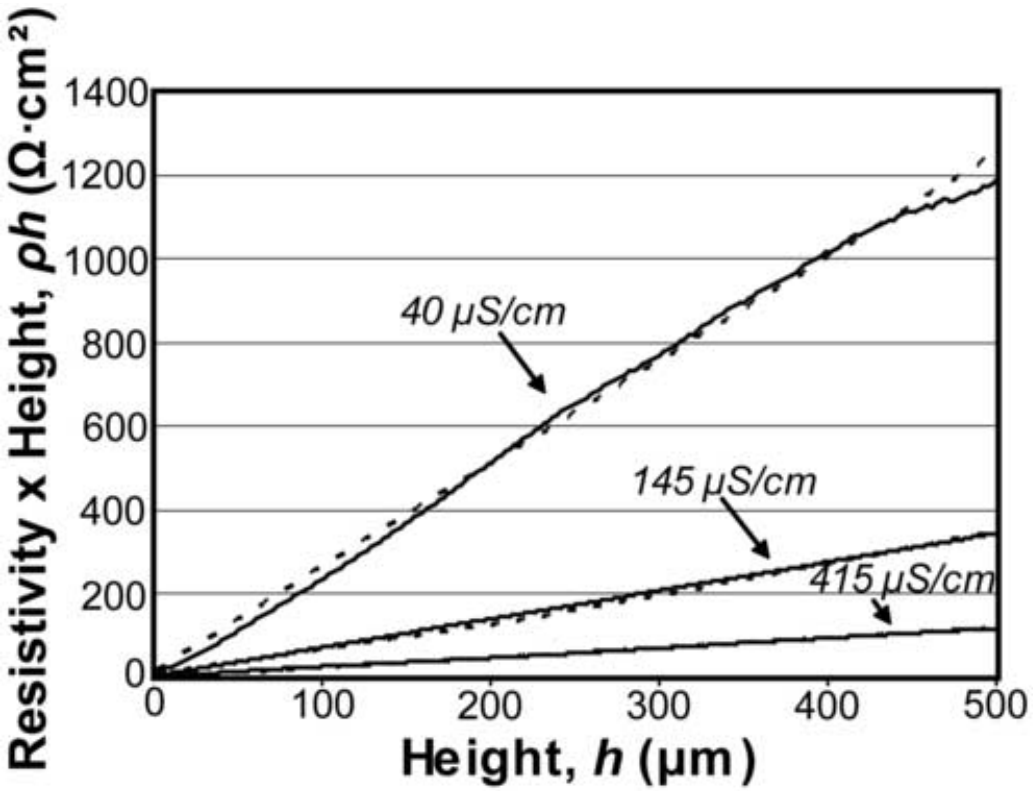

Figure 5.5: Calculated (dashed) and measured (solid) values for ρh for three different saline solutions versus probe height h

R_{meas} was measured as the probe was scanned vertically (increasing h), away from the base plane. The probe size and geometry are described at the beginning of this chapter. It should be noted that 60 kHz was used as the sinusoidal voltage excitation frequency because it allowed for very high signal-to-noise ratios as the spectrum analyzer was able to filter out spurious interference signals at lower frequencies. Capacitance terms were measured for different elements in the system and found to be so low, that at 60 kHz, impedance changes were dominated by resistivity.

Figure 5.5 shows a plot of $\rho_{\text{aver}} h$ (or $R_{\text{meas}} A_{\text{eff}}$) for three different saline solutions versus height h. These results are similar to those found in Figure 5.3 (a) in which there is a linear increase in total resistance versus height. Shown in Figure 5.5 are

direct comparisons of experimental data and computations from the FDM model using different solution conductivities. The measurement data used in this figure was smoothed with a linearly-weighted moving average filter to reduce quantization effects in the spectrum analyzer. The match between model and experiment is excellent, not only in curve shape but in absolute value. This match provides confirmation that the degree of current confinement predicted for the shielded probe is occurring in practice and $\rho_{\text{aver}}h$ will be a reasonable indicator for quantifying resistivity.

5.4 Experimental results

Much more interesting from an application's standpoint is the evaluation of real material samples below a conductive water solution. A first test case was formulated that involved a material with constant resistivity but well controlled sample heights at different areas. The material chosen was SU8 [81] - a photosensitive polymer that can be applied over a conductive surface in controlled thicknesses with an area defined using photolithography. The total R_{meas} in this case will be the combination of resistance due to the water and resistance due to the SU8. Given that these resistances would simply add in series, it was decided that the easiest way to deal with this situation was to make the total water resistance very small by using a high conductivity solution when testing the SU8 samples. In the test cases reported here, water of conductivity of σ=400 μS/cm was used, which turned out to be very high compared to the SU8 conductivity.

Test samples were constructed by first coating a very flat silicon wafer with a 300 nm thick aluminum layer through evaporation based deposition. The aluminum served as the conductive bottom plane for the sample. SU8 was then applied to the

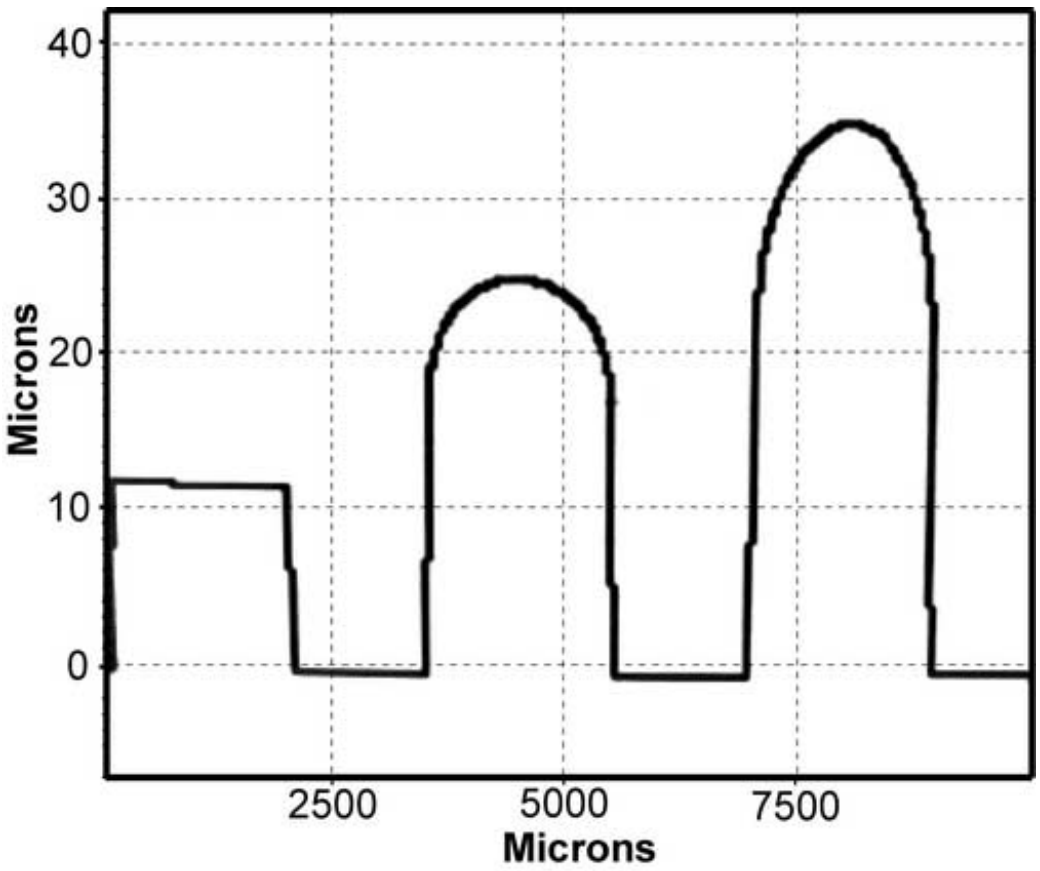

Figure 5.6: Profilometer scan of three SU8 squares indicating their height above a silicon wafer. Squares are approximately 1.5 mm wide

wafer using spin coating and hot plate curing. Using a series of photolithography steps and additional spin coatings, 1.5 mm $\times$ 1.5 mm squares of three different thicknesses were formed on the substrate adjacent to each other. Figure 5.6 shows a surface profile made of the wafer using a thickness profilometer (Tencor Alphastep 200) showing the three different SU8 thicknesses.

Given that the SU8 film has a homogeneous resistivity distribution, and that the water solution used during measurement has a much lower resistivity than the SU8, we would expect the ρh measurement over the different SU8 squares to vary linearly with SU8 height. Figure 5.7 shows the results of an SII scan across the middle

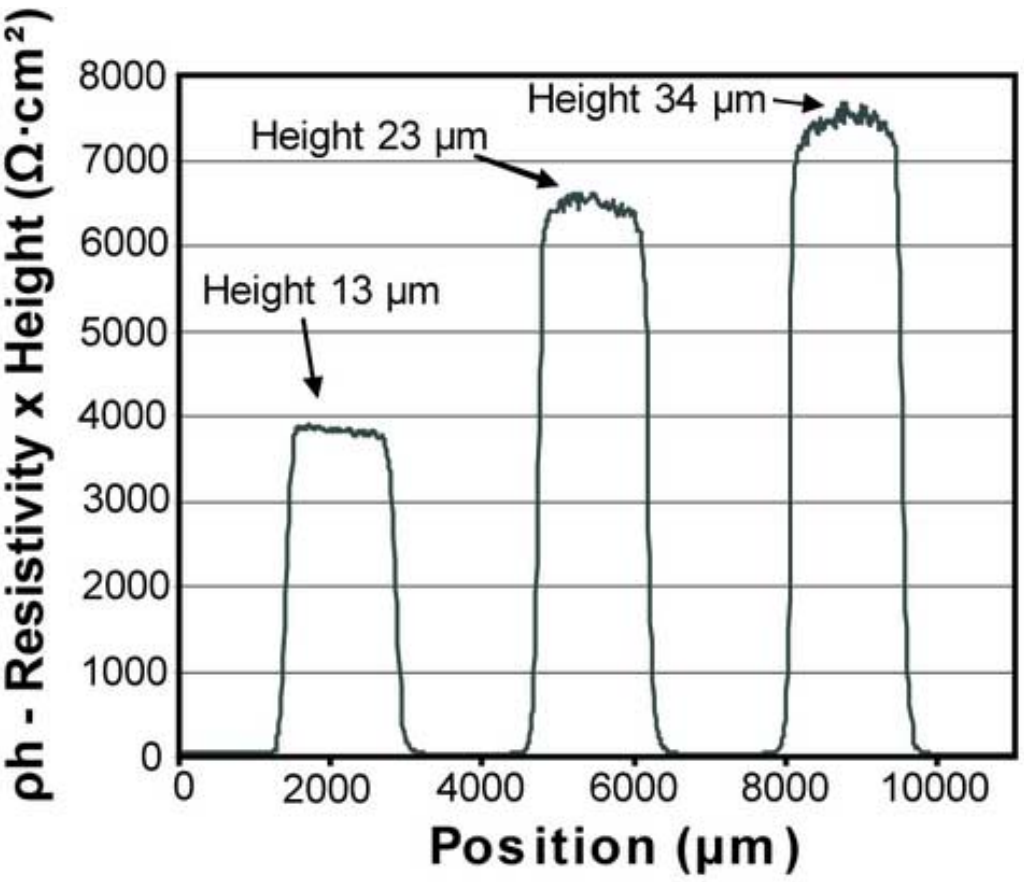

Figure 5.7: SII line scan of the three SU8 squares with results reported as ρh or $(R_{\text{sample}})(A_{\text{eff}})$. The height of the squares as measured using the profilometer is indicated.

of the SU8 squares. The R_{meas} values from the scan have been multiplied by the A_{eff} of the probe to produce ρh values for the sample. Figure 5.7 looks very similar to Figure 5.6 as expected, as they are both are in effect a measure of sample height. Given that we know the actual heights of the SU8 squares from the profilometer measurements, an absolute value of ρ can be reported for SU8, which is $\rho = 3 \times 10^6 \Omega$-cm. There is limited available literature reporting a resistivity value for SU8. In a single case we did find that involved the addition of silver nanoparticles to SU8 to make it more conducting, our reported resistivity value is within an order of magnitude of that projected for pure SU8[82].

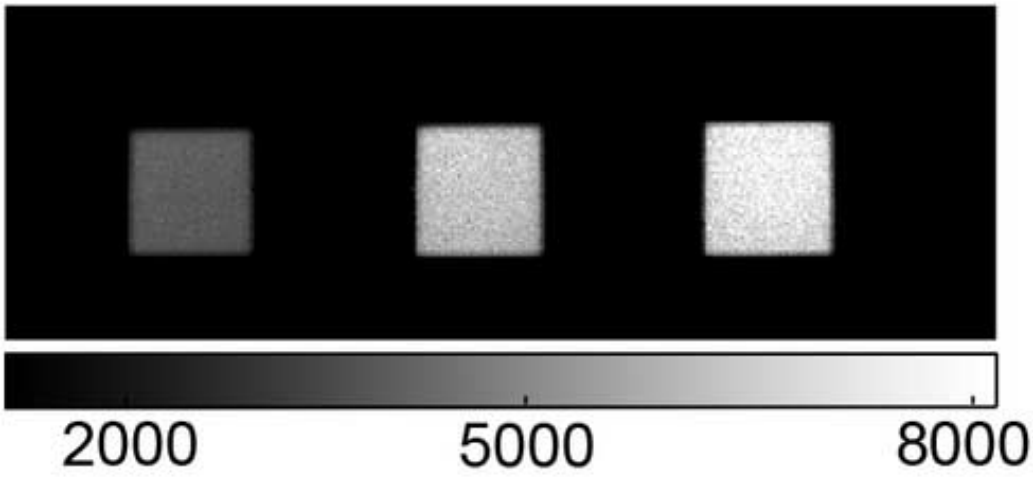

Figure 5.8: 2-D SII scan of SU8 squares. The black and white gradient scale is in terms of ρh, with units of Ω-cm^2, with the shortest square on the left side of the figure.

Figure 5.8 shows a two-dimensional area scan of three SU8 squares of variable height. The scan plots the quantity ρh as intensity on a black/white gradient scale with largest ρh (corresponding to the tallest square) the lightest color. The figure illustrates both the large contrast available for an image scan and the high spatial resolution possible, even using a probe tip with a D=100 μm diameter.

A further demonstration of the power of SII as a quantitative imaging tool is provided in Figure 5.9 for more complex material samples. This figure shows scans made on butterfly wing and on a silicon wafer covered with oxide. The conditions used to obtain these scans was similar to those used to create the SU8 images in Figure 5.7 and 5.8. The top left image in Figure 5.9 is a photograph of structures etched into the thin (300 nm) oxide layer on the silicon wafer. The bottom left image is an SII scan of the same wafer showing the contrast between the oxide coated regions and those free of oxide. The black box drawn in the upper left picture shows the area of the wafer scanned. The top right image is a photograph of a butterfly wing and below it is the same area scanned using the SII system. Prominent in the resistivity

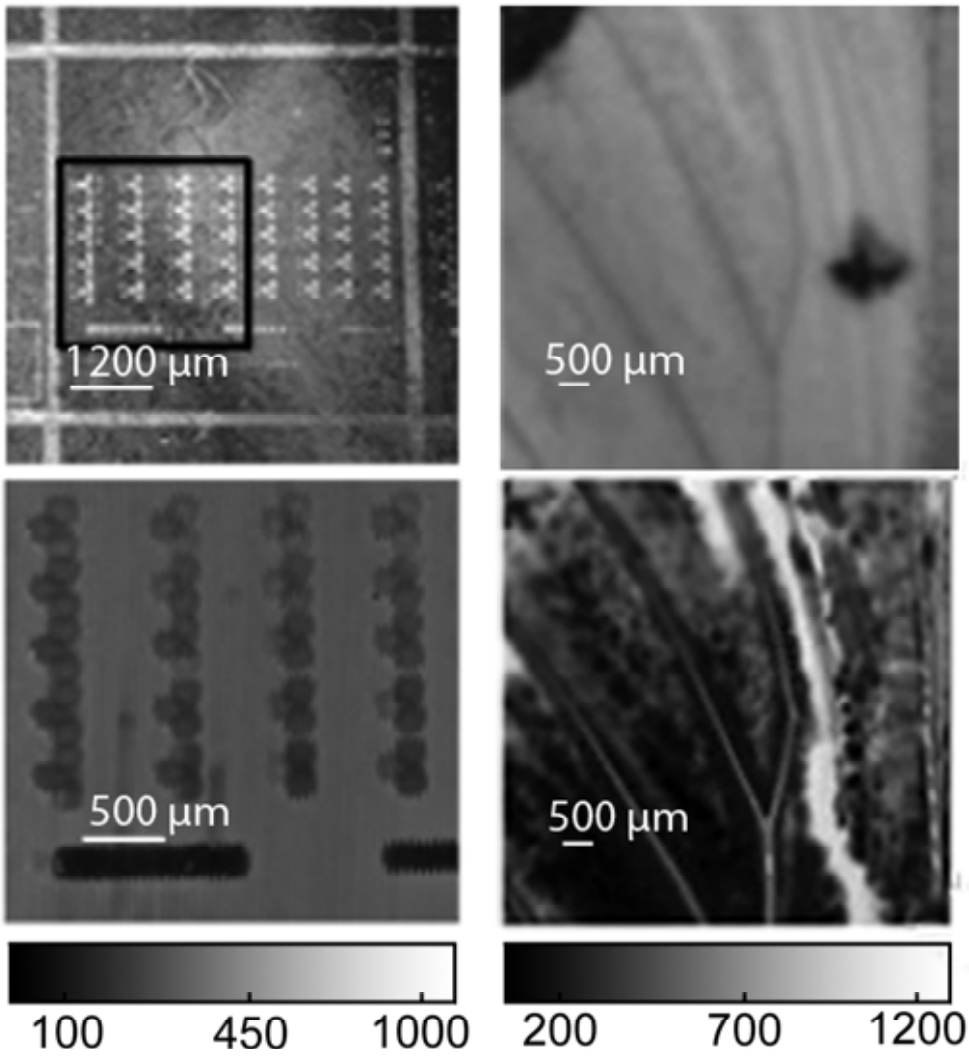

Figure 5.9: 2-D SII scans and optical pictures for oxide coated silicon wafter on left and butterfly wing on the right. The top images are optical photographs. The bottom images are SII scans reported in terms of ρh

scan are the veins in the wing and high resistivity regions that could not be obviously predicted from the optical photograph. In both of the images shown in Figure 5.9, the gradient scales are for ρh values (units of Ω-cm^2).

5.5 Significance and limitations

The method developed in this chapter seeks to quantify the resistivity of samples based on the fact of the current confinement introduced by the shielded-probe design. Simulations using the FDM model developed in Chapter 4 have shown that a shielded probe confines the current flowing into the center electrode to be a cylindrical volume with both homogeneous and heterogeneous resistivity distributions. Further, the cross-section area of the current confining cylinder (the effective area A_{eff}) holds an invariant value with its diameter $D_{\text{eff}} = D + S_p$. This allows for the determination of resistivity within this volume using a simple average value ρ_{aver} because of the small size of the cylinder. Given that sample height may be an unknown for a given material sample, the quantity $\rho_{\text{aver}}h$ is a natural way to report resistivity in SII scans.

This quantification provides the ability to quantify resistivity with the SII system as a new tool for classifying material properties and imaging a variety of samples. There is great significance based on this resistivity quantification. Three important contributions are listed as following,

- Quantitative Images: The contrast values in images obtained using this simple method are resistivity or resistivity timing with height. Both are more meaningful than the original images of the measured current. In other words, the method provides more physical meanings for the result images.

- Material Classification: The material composition of a sample can be analyzed with known resistivity values. Even for the measurement of $\rho_{\text{aver}}h$, the sample can be classified if the measurements of the same material were produced before.

- Comparison of Images: Images produced from different scans can be comparable so that different samples can be measured with correspondent result images.

Although this simple quantification allows for the value extraction of the resistivity, it contributes nothing to the improvement of resolution that is harmed by the blurring effect. The value $\rho_{\text{aver}}h$ examined in this simple method is an average value of a whole cylinder under the probe. Further, the A_{eff} would depends on the probe height h when h is small as shown in Figure 5.3 (b) ($h \leq 80\mu$m). Small h means that the probe is close to the sample. However, simulations in Chapter 4 have shown that best resolution is achieved when the probe is closest to the sample. All these issues indicate that this simple method is not a perfect solution if both the value and resolution are critical. This results in the requirement of a full solution with image reconstruction techniques applied. In next chapter, several methods of image reconstruction for the SII system will be proposed and implemented.

Chapter 6

Fast approximate models and image reconstruction for SII

The SII system seeks to produce 2-D images or 3-D volumes of impedance distribution for different samples at very high resolution as described in Chapter 3. However, the 3-D volume reconstruction could hardly be achieved due to the configuration with the probe along z direction. The signal picked up by the probe integrates the information along z direction which means the probe measures a path integral of the current density along z direction. This results in a lower sensitivity in z direction comparing to x and y direction. Due to this specialty of z direction, the SII system mainly focuses on 2-D image scans at this time. Unlike other medical imaging modalities such as MRI, CT, EIT and etc, the data set obtained by a typical SII system is the current map of a particular layer of the sample. This current map relates to the impedance image roughly pixel to pixel. Thus, SII can be considered as a 'direct-mapping' imaging method. However, The current at each position represents the whole effect of the impedance in a small region surrounding this position, which can be considered as a kind of image blurring. The measurements take into account everything (no approximations, all field perturbations, noise, etc.) but do not provide detail on the causes of image blurring. Chapter 4 derives the electrostatic theory and

the numerical FDM model for a SII system. The analysis and the results have shown that this blurring effect is not a simple blurring generated by convolution. No explicitly precise expression can be obtained at this point for the blurring function that represents the relationship between the current through the tip and the impedance distribution. This problem becomes a challenging inverse problem. One critical task here is to solve this problem to provide an approach that can obtain the impedance image from the measured current map. Thus, the SII modality can be described as a two step process. The first step is the construction of an appropriate instrument that can take sufficient measurements. The next step in the process is the image reconstruction of the impedance distribution from the data improving the resolution and signal-to-noise ratio.

Conventional methods for the inverse problem in the electrical impedance imaging focus on nonlinear inverse methods using a true 3-D numerical solver based on the finite difference method (FDM) or the finite element method (FEM). Based on the 3-D numerical FDM model introduced in Chapter 4, a framework of image reconstruction for the SII modality can be developed similarly to image reconstructions of other imaging modalities as shown in Figure 6.1. Here, a nonlinear parameter identification method is used to produce the impedance image. This algorithm must be initialized with a first guess of the impedance distribution, usually taken as uniform. Next, a computer model simulates the measuring process. By comparing the simulated currents to the data, the impedance estimation is updated until they agree under some assumptions. Also, regularization must be applied to this process due to the ill-posedness. These general optimization methods can obtain the results based on the theoretical analysis, however, they are limited by the computational ability of computers. These methods are usually CPU time intensive since there is a need to

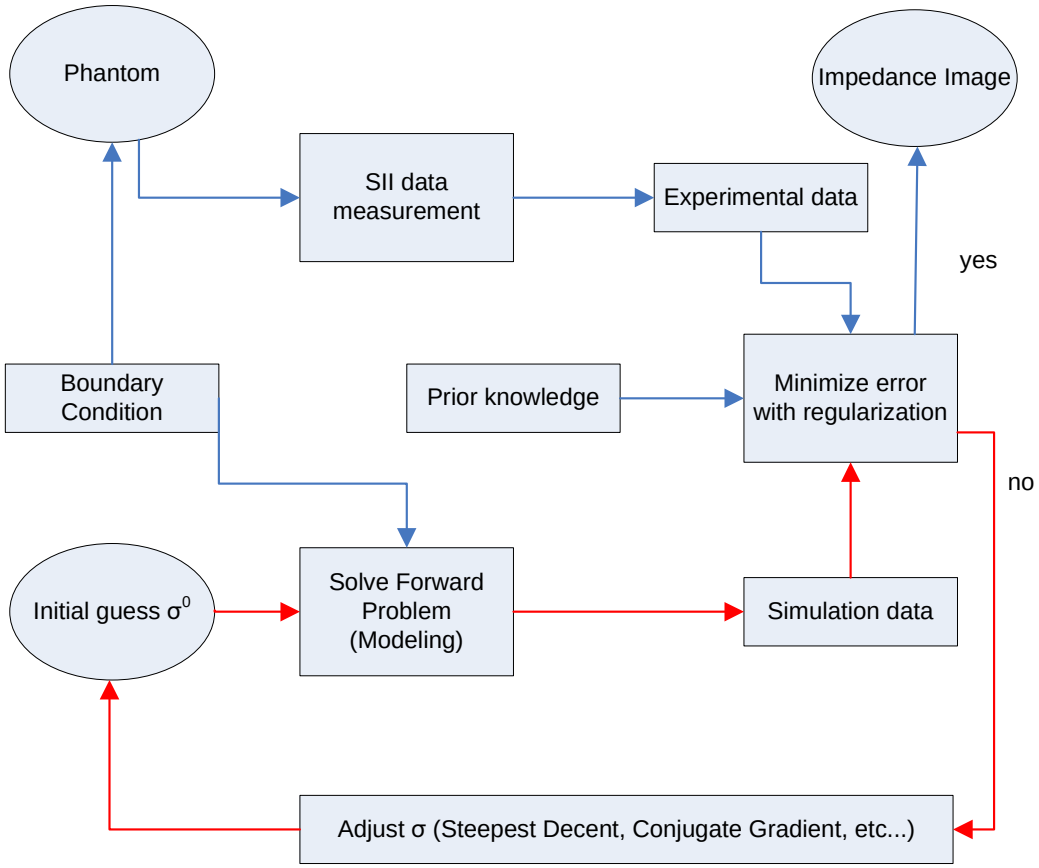

Figure 6.1: The main framework of image reconstruction for the SII system

solve the forward problems repeatedly during inverse iterations. For SII, the situation could be worse. As mentioned in Chapter 4, the forward problem of SII simulates the measuring process. It can be considered as a system with an impedance image as input and the output is a current image. For each pixel of the current image, the forward solver has to solve the PDE equation mentioned in Chapter 4 following the steps as shown in Figure 4.5. It can be noticed that solving this PDE is also an iterative process. Thus, the forward problem requires iterative solutions of the PDE for every pixel. This leads to huge computational cost. Further, in each iteration of the inverse problem, the forward problem need to be solved at least once. It can be imagined that image reconstruction of SII could hardly be achieved practically using

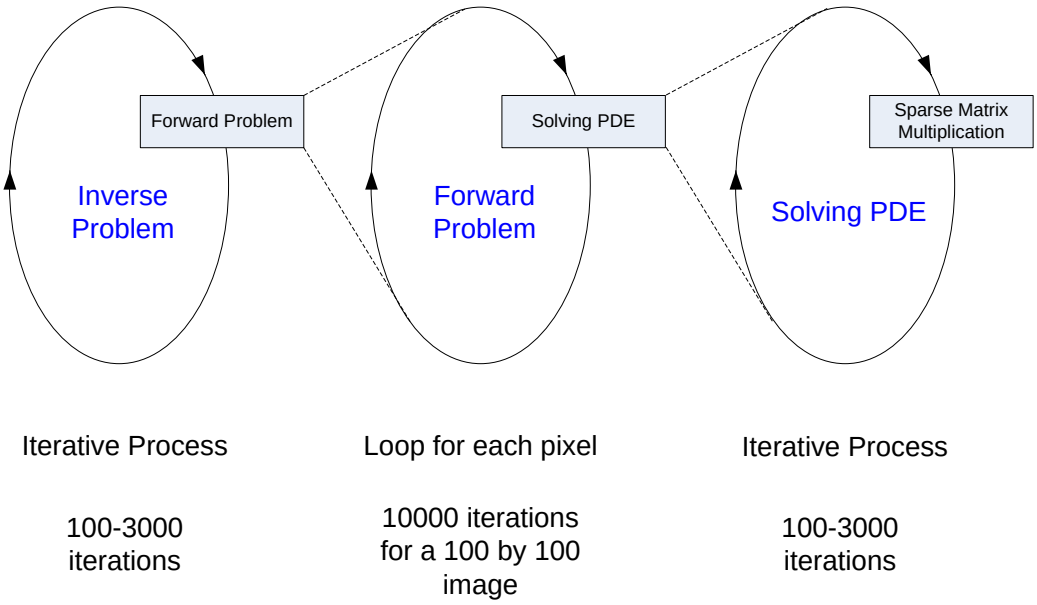

Figure 6.2: The computational cost of conventional methods using the numerical FDM model for image reconstruction of SII

this approach. Also, the computational cost raises up dramatically when the image size increases. Figure 6.2 shows this situation clearly.

In this chapter, fast approximate models are developed to produce the solution of the forward problem with much less computational time and memory occupation compared to the numerical FDM model. Fast image reconstruction methods are derived based on these models. These models can be classified to two major groups according to their assumptions. The first group is developed using charge theory and homogeneous assumption. The second one is based on the reciprocity principle[83]. Among them, the Modified Linear Approximation (MLA) demonstrates the best performance. With the help of MLA, fast image reconstruction can be achieved by avoiding the true 3-D numerical forward solver during the inverse iterations. Total variation regularization is applied. The determination of parameters is also analyzed.

As mentioned above, due to lack of independent measurements in z direction, Only 2-D image measurements are considered here. All the experimental results in this chapter are in 2-D images with the assumption the impedance in z direction is uniform.

6.1 Simple model I: Simplified Linear (SL) model

6.1.1 Model formula for the unshielded case

Consider the current through a conducting tip placed a distance h above a conducting ground plane. If the tip is not surrounded by a shield as an unshielded case, the current through the ground plane should be the same as the current through the tip. Therefore, the current through the tip is

$$I = \int_{xy} \sigma \frac{\partial V}{\partial z} dxdy \Big|_{z=0}. \tag{6.1}$$

From the electrostatic analysis in Chapter 4, V can be calculated from the potential, ϕ, which can be obtained by using the true FDM model. Besides this numerical approach, exact solution of V can hardly be achieved. However, some simple solution could approximate V reasonably well under assumptions. Here, three assumptions are introduced to simplify this complicated relationship significantly. These assumptions are justified only under specific conditions which are admittedly not always met during all scanning impedance experiments. Therefore, the theory can be improved upon in the future. However, making these assumptions provides a tractable linear theory that can be compared against simulations and (most impor-

tantly) experimental data. This linear model can then be used to develop a simple, linear reconstruction algorithm for 2-D conductivity from 2-D current measurements. Here are the three assumptions:

- **Assumption I:** The current is the same as it would be in an infinite material. From experiences in solving the numerical FDM model, this assumption should be valid for scan points near the center of the experiment since the potential field decreases dramatically from the scanning point. Towards the boundaries of the experiment, the potential field would be tolerated by the boundary conditions. If the lateral boundaries in the experiment are moved out to places where the potential field is vanishingly small, the errors associated with this assumption could be minimized. Thus, with some effort of making proper boundaries in the experiment, this assumption could be valid everywhere in the region of interest.

- **Assumption II:** $\partial V/\partial z$ is independent of σ and, therefore, the same as it would be for a medium of homogeneous (background) conductivity. This is the key to linearizing the relationship between I and σ. This assumption can be compared to the Born approximation made in inverse scattering. In biological samples, this assumption should be fairly mild as conductivity is supposed to vary moderately from a background value. Admittedly, however, this could not be hold for large variations in conductivity, for instance, the boundary between different materials. For biological samples, these situations can be avoided in most cases. Another issue is that this assumption could harm the resolution as it considers no sharp changes. Thus, the results would not be perfectly deblurred. However, it could help to eliminate most of the blurring effect.

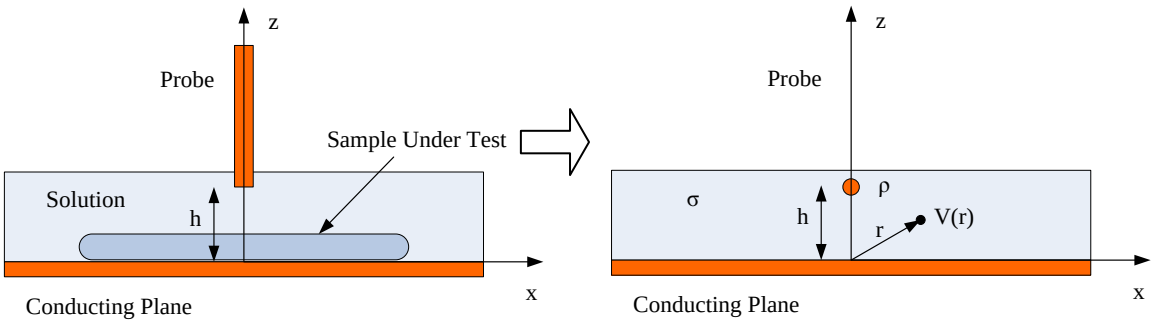

Figure 6.3: The idea of the simple linear (SL) model for the SII system. V(**r**) is the voltage at position **r**. The probe is considered as an infinitesimal charge above the conducting plane. The variation of the conductivity of the sample is small enough to be replaced with the conductivity of the background.

- **Assumption III:** The potential distribution due to the conductive tip (from which $\partial V/\partial z$ is independent of σ can be calculated) is the same as it would be by placing an infinitesimal point charge at (or near) the location of the center of the tip. Simulations show that away from the center of a small tip, the potential is distributed almost same way of the infinitesimal charge. In the SII system, where the diameter of the tip is comparable to the distance between the tip end and the plane, this simplifying assumption actually explains much of the observed potential variation. This is not unreasonable since an exact formula could be obtained by placing the correct surface charge distribution on the tip and integrating. At some distance away from the tip, the precise surface charge distribution is inconsequential and the true distribution can reasonably be replaced with a constant charge integrated over the tip area, which-at this distance-is equivalent to a point charge placed at the center of the tip. Thus, "'the distance"' may not be the exact distance between the tip end and the plane. This number becomes a parameter for this model in most cases.

With the help of these three assumptions, a simple linear model can be derived from the electrostatic analysis as shown in Figure 6.3. The potential (voltage) can be obtained by placing a charge at the center of the tip and using the method of images to account for the ground conducting plane. The formula is

$$V(\mathbf{r}) = \frac{q}{4\pi\epsilon}\left[\frac{1}{|\mathbf{r} - h\hat{\mathbf{z}}|} - \frac{1}{|\mathbf{r} + h\hat{\mathbf{z}}|}\right] \tag{6.2}$$

where q is the equivalent charge at the center of the tip and $\mathbf{r}$ is the position vector

$$\mathbf{r} = x\hat{\mathbf{x}} + y\hat{\mathbf{y}} + z\hat{\mathbf{z}}. \tag{6.3}$$

On the ground plane, it can be observed

$$\left.\frac{\partial V}{\partial z}\right|_{z=0} = \frac{q}{4\pi\epsilon}\left[\frac{2h}{(x^2 + y^2 + z^2)^{3/2}}\right]. \tag{6.4}$$

The assumption of an infinite domain implies shift invariance of the model. The formula would also be valid when the probe is moved to the position (x', y'). Thus, Equation (6.1) becomes

$$I(x', y') = \int_{xy} \sigma(x, y) \cdot \frac{q}{4\pi\epsilon}\left[\frac{2h}{((x' - x)^2 + (y' - y)^2 + z^2)^{3/2}}\right] dxdy. \tag{6.5}$$

It can be noticed that the relationship between I and σ turns out to be a convolution with a kernel K_h. The subscript h of K_h represents that the kernel is depend on the distance between the tip end and the plane. From Equation (6.5), a thin-sample, 2-D,

linear shift-invariant model can be obtained:

$$I = \frac{q}{2\pi\epsilon h^2} K_h * \sigma \tag{6.6}$$

where $*$ represents 2-D convolution. K_h is given by

$$K_h(x, y) = \frac{h^3}{(x^2 + y^2 + h^2)^{3/2}}. \tag{6.7}$$

This kernel function is normalized and symmetric. It is the impulse response of this model.

This model is valid only if the conductivity does not vary significantly over the sample and if h is large enough so that the ground plane can be considered distant from the tip. Under those circumstances, h represents the exact height between the tip end and the conducting plane and q is the integrated charge density on the tip end during measurement. If one of these assumptions could not be hold, h and q would lose their physical meaning. However, experiments have shown that this model could be useful if h and q are considered as model parameters. These parameters need to be determined by fitting the model to the experimental data. In either case, q could hardly be known priorly. Thus, only relative value of conductivity can be obtained from the current measurements by inverting this model. This results in a relative-valued image reconstruction of SII using this model.

While somewhat crude, the simplified linear model suggests that measured current values collected into an image will provide a blurred image of relative conductivity. Simple deblurring models could provide high-resolution images proportional to conductivity, σ. The model also suggests that height above the ground plane is

the dominant cause of blurring while q only affects the absolute value. Thus, if the samples are thin-enough and the probe is positioned near enough, high-resolution images of relative conductivity can be obtained as expected.

Since most of the probes used in the experiments for SII are shielded, this model need to be explored in the shielded case. This expansion is the main significance of the model of the unshielded probe.

6.1.2 Model formula for the shielded case

The structure of the shielded probe is shown in Figure 3.5. The central tip is surrounded by an insulator and then surrounded by a metal shield. The first two assumptions: 1) an infinite region, 2) small variation in voltage when comparing the case of inhomogeneous media to the homogeneous one, are still valid for this case. For the third assumption: constant (infinitesimal) charge distribution, a modification is necessary due to the special structure of the shielded probe. The tip is still considered as an infinitesimal charge, however, the shield is much bigger and the cylinderal structure of the shield could not be ignored. Thus, for the model of the shielded case, the tip end is still an infinitesimal charge q, but the shield is a collection of N point-charges totaling $q_1$with N is large enough. The shield ring is assumed to be a distance b from the center of the tip. Using the method of images again, the voltage can be obtained in the region of interest as

$$\begin{aligned} V(\mathrm{r}) &= \frac{q}{4\pi\epsilon}\left[\frac{1}{|\mathrm{r}-h\hat{z}|}-\frac{1}{|\mathrm{r}+h\hat{z}|}\right] \\ &\quad +\frac{q_1}{4\pi N\epsilon}\sum_{n=0}^{N-1}\left[\frac{1}{|\mathrm{u}_n(\mathrm{r})-h\hat{z}|}-\frac{1}{|\mathrm{u}_n(\mathrm{r})+h\hat{z}|}\right] \end{aligned}$$

where

$$\mathrm{u}_n(\mathrm{r}) = \mathrm{r} - b\cos(2\pi\frac{n}{N})\hat{\mathrm{x}} - b\sin(2\pi\frac{n}{N})\hat{\mathrm{y}}.$$

Simplifying, this equation becomes

$$\begin{aligned} V(\mathrm{r}) &= \frac{q}{4\pi\epsilon}\left[\frac{1}{\sqrt{\rho^2+(z-h)^2}} - \frac{1}{\sqrt{\rho^2+(z+h)^2}}\right] \\ &\quad + \frac{q_1}{4\pi N\epsilon}\sum_{n=0}^{N-1}\left[\frac{1}{\sqrt{\rho_n^2(x,y)+(z-h)^2}} - \frac{1}{\sqrt{\rho_n^2(x,y)+(z+h)^2}}\right] \end{aligned}$$

where

$$\rho_n^2(x,y,b) = (x - b\cos(2\pi\frac{n}{N}))^2 + (y - b\sin(2\pi\frac{n}{N}))^2$$

and

$$\rho^2 = \rho_n^2(x,y,0).$$

In the limit as $N \to \infty$, by defining $\xi = q_1/q$, and using cylindrical coordinates:

$$\begin{aligned} x &= \rho\cos\theta \\ y &= \rho\sin\theta, \end{aligned}$$

a simplifier formula can be obtained,

$$\begin{aligned} V(\mathrm{r}) &= \frac{q}{4\pi\epsilon}\left[\frac{1}{\sqrt{\rho^2+(z-h)^2}} - \frac{1}{\sqrt{\rho^2+(z+h)^2}}\right. \\ &\quad \left. + \frac{\xi}{\sqrt{(\rho-b)^2+(z-h)^2}} - \frac{\xi}{\sqrt{(\rho-b)^2+(z+h)^2}}\right]. \end{aligned}$$

Therefore,

$$\left.\frac{\partial V}{\partial z}\right|_{z=0} = \frac{q}{2\pi\epsilon h^2}\left[\frac{h^3}{(\rho^2+h^2)^{3/2}} + \frac{\xi h^3}{[(\rho-b)^2+h^2]^{3/2}}\right].$$

Now, however the current through the tip is not the current through the ground conductor. Instead, the current through the tip must be some fraction of the current through the ground plane:

$$I = \beta(h) \int_{xy} \sigma \frac{\partial V}{\partial z} dxdy \Big|_{z=0}.$$

Thus,

$$K^{\text{shield}}_{h,b,\xi}(\rho) = \beta(h) \left[\frac{h^3}{(\rho^2 + h^2)^{3/2}} + \frac{\xi h^3}{[(\rho - b)^2 + h^2]^{3/2}} \right]$$

is the kernel of the simple linear model for the shielded case where $\beta(h)$ is a proportionality constant assumed to be independent of σ (a linearization assumption). Numerical simulations in homogeneous materials suggests that $\beta(h)$ is power-law dependent on h:

$$\beta(h) = c_0 h^{\gamma}.$$

It can be seen that this kernel is dependent on three parameters: h, b, ξ in which h and b depends on the system configuration and the probe dimension while ξ is hard to determine. However, the parameters can be calculated by fitting to experimental data. Further, it can be seen that the model for the shielded case is not significantly different from that of the unshielded case. The second term involving $(\rho-b)^2+h^2$in the denominator is nearly identical to the first term when $b/h \ll 1$. Typically, in order to use the simplified model, this condition $b/h \ll 1$ has to be assumed anyway so that the tip can be approximated as a point charge. As a result, even in the shielded case, the unshielded blurring function is a useful model to be applied to results. Furthermore, as mentioned above, more unknown parameters and more difficult Fourier transform

lead to higher complexity of the shielded model which makes it less useful than the unshielded one.

6.2 Simple model II: Reciprocity Principle (RP) models

The SL model can hardly represent the detail of the geometry of the probe, which leads to a lack of accuracy for the shielded case. Further, since the value of the charge is hard to determine, the SL model is a relative model without the ability of quantification of the impedance distribution. Among the three assumptions proposed above, the charge assumption is too strong. Thus, other approaches are explored to avoid this assumption so that the detail of the shielded-probe design can be modeled.

In this section, the reciprocity principle is applied to the SII system. The analysis based on it provides another series of models that reveal the relationship between the impedance distribution and the current through the tip with the consideration of the shielded-probe design. These models are based on weaker assumptions.

6.2.1 Reciprocity Principle in SII

Unshielded case

The region of interest in a typical SII system consists of the sample and the conducting solution. Due to the low-frequency signals used in the SII system, it can be noticed that the electromagnetic field out of the region of interest is trivial. Thus, the current density is zero through the surface everywhere except for the end of the tip (and the shield) and the conducting plane. Figure 6.4 shows this idea clearly. The

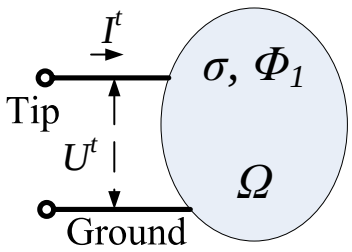

Figure 6.4: Conducting region Ω with conductivity σ. (a) A voltage U^t applied to the tip and the ground leads to a potential distribution ϕ. The current through the tip I^t can be measured.

ellipse represents the region of interest in the SII system as a conducting domain Ω with conductivity σ. This domain has two ports with current through: one represents the tip and one is the conducting plane as shown in the figure. Here, the conducting plane is considered as the ground with zero potential. A voltage U^t is applied to the tip and the conducting plane, which excites an electromagnetic field inside the region Ω. As the model in Chapter 4, when the wavelength of electromagnetic field is much longer than the dimensions of the experimental setup such as the SII system, it is common to ignore the small contribution from the magnetic field and write $E = -\bigtriangledown\phi$ where ϕ is the electric scalar potential in Ω. I^t is the current through the tip and $-I^t$ is though the ground port. From Ohm's Law, the current density J in Ω satisfies the following formula,

$$J = -\sigma E = -\sigma \bigtriangledown \phi, \tag{6.8}$$

where E is the electric field in the domain Ω. Multiply the electric potential ϕ on both sides and integrate the equation over the boundary $\partial\Omega$,

$$\int_{\partial\Omega} J\phi \cdot ds = -\int_{\partial\Omega} \phi\sigma \bigtriangledown \phi \cdot ds. \tag{6.9}$$

The normal component of J is zero everywhere on the boundary $\partial\Omega$ except for on the two ports (the tip and the conducting plane) in Figure 6.4. The potential ϕ is zero on the conducting plane (ground) and is U^t on the tip. Thus, the left-hand side of Equation (6.9) simplifies to $U^t I^t$. Applying Gauss' theorem to the right-hand side, Equation (6.9) can be rewritten as

$$U^t I^t = -\int_\Omega \bigtriangledown \cdot (\phi\sigma \bigtriangledown \phi) d\Omega. \tag{6.10}$$

To simply the right-hand side, notice that

$$\bigtriangledown \cdot(\phi\sigma \bigtriangledown \phi) = \sigma \bigtriangledown \phi \cdot \bigtriangledown\phi + \phi \bigtriangledown \cdot(\sigma \bigtriangledown \phi), \tag{6.11}$$

and because $\bigtriangledown \cdot (\sigma \bigtriangledown \phi) = 0$ for all the points in the domain, Equation(6.10) simplifies to

$$I^t = -\frac{1}{U^t}\int_\Omega \sigma \bigtriangledown \phi \cdot \bigtriangledown\phi d\Omega. \tag{6.12}$$

Shielded case

For the shielded case, similar formulas could be developed. The difference between the unshielded case and the shielded case is that there is one more port that represents the shield as shown in Figure 6.5. Consider the region of interest Ω in the shielded case with conductivity σ. It can be noticed that the current through the shield I^s is also unknown. Thus, it demands two setups with different boundary conditions so that two independent equations can be established to solve I^t and I^s. U_1^t is the voltage applied to the tip while another voltage U_1^s drives the shield, which leads to an electric scalar potential distribution ϕ_1. Hence, a current through the tip

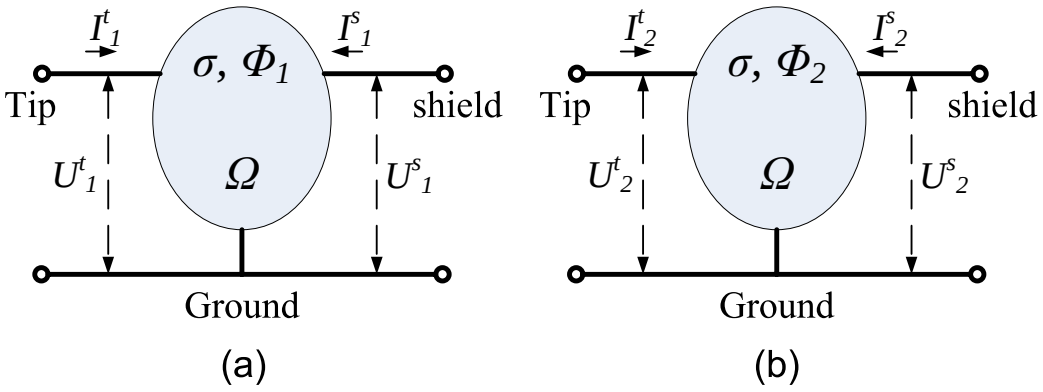

Figure 6.5: Conducting region Ω with conductivity σ. (a) A voltage U_1^t applied to the tip and another voltage U_1^s applied to the shield lead to a potential distribution ϕ_1. The current through the tip I_1^t and the current through the shield I_1^s can be measured. (b) Changing the voltage on the shield to zero results in a different potential distribution ϕ_2 with different currents I_2^t, I_2^s.

I_1^t and a current through the shield I_1^s can be measured. On the other hand, U_2^t and U_2^s excites ϕ_2 in the region Ω and I_2^t and I_2^s are the corresponding currents.

For the first case, Ohm's law is

$$J_1 = -\sigma \bigtriangledown \phi_1, \tag{6.13}$$

where J_1 is the current density in the domain Ω. Multiply the potential obtained in the second case, ϕ_2, on both sides and integrate the equation over the boundary $\partial\Omega$:

$$\int_{\partial\Omega} J_1\phi_2 \cdot ds = -\int_{\partial\Omega} \phi_2\sigma \bigtriangledown \phi_1 \cdot ds. \tag{6.14}$$

The normal component of J_1 is zero everywhere on the boundary except for on the conducting plane, the tip, and the shield. The voltage, ϕ_2 is zero on the conducting plane and is U_2^t on the tip, U_2^s on the shield. The current through the shield in the first case is I_1^s and the current through the tip is I_1^t. Thus, the left-hand side of the

previous equation simplifies to $U_2^t I_1^t + U_2^s I_1^s$. Similar to the unshielded case, (6.14) becomes

$$U_2^t I_1^t + U_2^s I_1^s = -\int_\Omega \bigtriangledown \cdot (\phi_2 \sigma \bigtriangledown \phi_1)\, d\Omega. \tag{6.15}$$

Then, for the second case, let the shield connected to the ground and the voltage applied to the tip same as the one in the first case. Thus, the first case simulates the experimental configuration and the second case shorts the shield to the ground,

$$U_2^t = U_1^t = U^t \text{ and } U_2^s = 0. \tag{6.16}$$

Also notice that

$$\bigtriangledown \cdot (\phi_2 \sigma \bigtriangledown \phi_1) = \sigma \bigtriangledown \phi_2 \cdot \bigtriangledown \phi_1 + \phi_2 \underbrace{\bigtriangledown \cdot (\sigma \bigtriangledown \phi_1)}_{=0}. \tag{6.17}$$

Equation (6.15) simplifies to

$$I^t = I_1^t = -\frac{1}{U^t} \int_\Omega \sigma \bigtriangledown \phi_2 \cdot \bigtriangledown \phi_1 d\Omega. \tag{6.18}$$

6.2.2 Reciprocity Principle (RP) model

Equation (6.12) and Equation (6.18) establish explicit relationships between the current through the tip and the conductivity distribution in the region Ω for both the unshielded and the shielded cases. Two assumptions were used in the development of these two formulas. However, these two formulas are still complicated because the ϕ, ϕ_2 and ϕ_1 potential distributions are themselves dependent on σ. Another two

assumptions are introduced to simply these relationships significantly. To be clear, all the four assumptions are listed here.

- **Assumption I:** The current through the surface is zero everywhere except for the tip (and the shield) and the conducting plane. The low-frequency environment allows this assumption to be valid. No notable radiation can be observed in experiments. With the help of this assumption, the region of interest in a SII system can be simply represented as a conducting domain with ports on it as shown in Figure 6.4 and Figure 6.5.

- **Assumption II:** The contribution of the magnetic field is trivial that can be ignored. Usually, at low frequency, the vector potential is so small that the electric field is mainly dependent on the scalar potential ϕ as $E = \sigma \bigtriangledown \phi$. The validation of this assumption is critical for the electrical impedance imaging. In this imaging modality, the electrical properties including σ and ϵ are the contrast of the images without the consideration of the permutability.

- **Assumption III** (same as Assumption I in the SL model)**:** The current is same as it would be in an infinite material. Far from the boundaries of the sample, the linear operator can be considered shift-invariant (at least in two-dimensions).

- **Assumption IV** (similar as Assumption II in the SL model)**:** ϕ, ϕ_2 and ϕ_1 are independent of σ, therefore, the same as they would be for a medium of homogeneous conductivity. This is the key to linearizing the relationship between I and σ. In biological samples, the conductivity varies moderately from a background value, therefore, this assumption could be hold in most experiments.

The first two assumptions are also used in the FDM model. They are valid with few limitations. The third one is same as the one in the SL model and they have same reasons and validations. The fourth one is similar to the one in the SL model, however, assumes approximate electrical potential distributions rather than $\partial V/\partial z$ that is correspondent to the electric field. When the linear and shift-invariant approximations are valid, (6.12) and (6.18) can be seen as convolutions,

$$I(\mathbf{x}') = \int \sigma(\mathbf{x}) K(\mathbf{x}' - \mathbf{x}) \, d\mathbf{x}, \tag{6.19}$$

where

$$K(\mathbf{x}) = \begin{cases} -\frac{1}{U} \bigtriangledown \phi(-\mathbf{x}) \cdot \bigtriangledown \phi(-\mathbf{x}) & \text{unshielded case} \\ -\frac{1}{U} \bigtriangledown \phi_2(-\mathbf{x}) \cdot \bigtriangledown \phi_1(-\mathbf{x}) & \text{shielded case} \end{cases}. \tag{6.20}$$

The SII system only takes 2-D data, and it is more difficult to justify shift-invariance in the third dimension. Thus, the linear equation more appropriate for SII assumes that the conductivity in the z-direction is its average so that

$$I(x, y) = \sigma(x, y) \star k(x, y), \tag{6.21}$$

where $\star$ represents two-dimensional convolution, $\sigma(x, y) = \int \sigma(\mathbf{x}) \, dz$, and

$$k(x, y) = \int K(\mathbf{x}) \, dz. \tag{6.22}$$

This two-dimensional model is called the Reciprocity Principle (RP) model.

6.2.3 Modified Linear Approximation (MLA)

The linear assumption (Assumption IV) made previously is not always true, especially when abrupt changes of conductivity occur. For example, Figure 6.7(c) shows that the RP model almost fits the data from a true 3-d simulation except for on the low-valued end of the abrupt change in σ. In order to create a model that fits experimental data, an approximation has been developed combining two linear kernels, the RP kernel and a Gaussian kernel with a weighting that is dependent on the value of conductivity at a given location. In particular,

$$I(x,y) = w(\sigma) \cdot (\sigma * k) + (1 - w(\sigma)) \cdot (\sigma * k_l). \tag{6.23}$$

The Gaussian kernel, k_l, has a width chosen to match the width of the RP kernel and a height chosen so that the Gaussian kernel and the RP kernel both have the same integral. In addition, $w(\sigma)$ is a weight coefficient linearly-dependent on σ and chosen so that the Gaussian kernel is weighted more heavily when σ is small and weighted less heavily when σ is near the background value of σ_b. Specifically,

$$w(\sigma) = \begin{cases} \gamma_1 & \sigma = 0, \\ \frac{\sigma}{\sigma_b}(\gamma_2 - \gamma_1) + \gamma_1 & 0 < \sigma < \sigma_b, \\ \gamma_2 & \sigma \geq \sigma_b. \end{cases}$$

The values of γ_1 and γ_2 are chosen based on simulations and are assumed constant for a given geometry and driving voltage. Because of the simulation match to the RP kernel when $\sigma \approx \sigma_b$, $\gamma_2 \approx 1$ is usually selected. Then, γ_1 is chosen by matching the MLA-predicted curve with the full 3-D model for a step function in conductivity. Values

less than 0.5 (such as 0.15 or 0.2) for γ_1 are typical for the experiments described in this paper. The value of γ_1 determines how much of the Gaussian kernel is used for low values of σ. By weighting two linear convolution kernels with a conductivity-dependent weight, we have produced a simple non-linear model that can be exposed more clearly by writing (6.23) as

$$I = \sigma * k_1 + \sigma \cdot (\sigma * k_2)\,, \tag{6.24}$$

where I and σ are 2-D images, $\cdot$ is element-by-element multiplication,

$$k_1 = \gamma_1 k + (1 - \gamma_1)\, k_l$$

and

$$k_2 = \frac{\gamma_2 - \gamma_1}{\sigma_b} k - \frac{\gamma_2 - \gamma_1}{\sigma_b} k_l.$$

It can be seen that only two 2-D convolutions and one 2-D element-multiplication are necessary in the calculation of I. As long as this is sufficiently accurate, there is no need for the 3-D numerical solution of the PDE in Equation (4.5) at multiple scan positions in the forward solver. Thus, the modified model can be computed much faster than the true 3-D FDM model and makes possible quick image reconstruction.

6.3 Kernel evaluation

As stated above, the kernel of the SL model can be obtained from Equation (6.7) for both unshielded and shielded cases. The key is to determine the value of h which can be considered as an optimization parameter during the kernel fitting

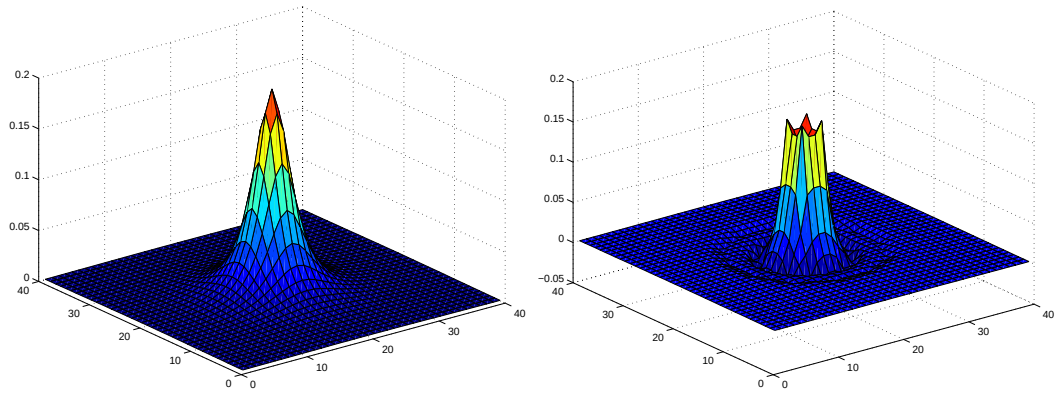

Figure 6.6: The shaded surface plot of two-dimensional kernel function. (a) the kernel of the SL model $h = 35\mu$m, (b) the kernel of the RP model for a ($D = 30\mu$m, $S_p = 30\mu$m, 30-μm shield thickness) probe, $V_t = 2.3$V and $V_s = 2.5$V

process. In practice, it is not hard to provide an estimated value for h based on previous experience.

The kernel of the RP model can be obtained from Equation (6.20) and (6.22). The critical step in the kernel evaluation is the determination of the potential ϕ for different boundary conditions. For a given homogeneous σ, ϕ can be solved using the FDM method proposed in Chapter 4. After determination of ϕ, the gradient of ϕ can be approximated using central differences. In the practical case of an inhomogeneous medium, one important issue is that the voltage of the tip varies during the scanning procedure. Thus, there is no fixed value for the voltage of tip that can be used in the kernel calculation. One possible solution is to treat the voltage of the tip V_t as a parameter of the kernel and tweak V_t for the best fit. Since the modified model is a calibrated model for the SII system, V_t can be determined from the known conductivity of the background medium and the corresponding current through the tip.

Figure 6.6 shows the shaded surface plots of two-dimensional kernels of both the SL model and the RP model for the shielded case. For the SL model, the height parameter h is 35μm. For the RP model, the tip diameter and the shield thickness are both 30 μm while the gap spacing between the shield and the tip is also 30 μm wide. The potential ϕ_1 is simulated with a 2.3V voltage applied to the tip and a 2.5V voltage applied to the shield. Then, we obtain ϕ_2 by repeating the same process except using zero voltage on the shield. It can be observed that the kernel function of the RP model has a sharper edge and represents more details of the probe structure than the kernel of the SL model. The sharper edge shows that the RP model might be able to reveal the shield function better than the SL model since the shield helps to shrink the average cross-section area of current flow through the sample.

6.4 Evaluation for simple models

To demonstrate all the simple models to SII, line scans were modeled and compared to the simulated measurements. These line-profiles were taken from 3-d simulations such as those reported on in Figure 6.8 and Figure 6.9. A shielded probe was used with $D = 30\mu$m, $S_p = 30\mu$m and 30-μm shield thickness. The simulated measurements were generated using the true 3-D FDM forward solver proposed in Chapter 4.

Figure 6.7(b), Figure 6.7(c) and Figure 6.7(d) show 1-d line-scans of the 3-D FDM model and the simple models simulated based on the conductivity profile shown in Figure 6.7 (a) with an abrupt change in the middle along the scanning direction. Confidence in the simple models can be built by comparing its predictions to the true 3-D FDM model in simulations. Very good correspondence can be observed between

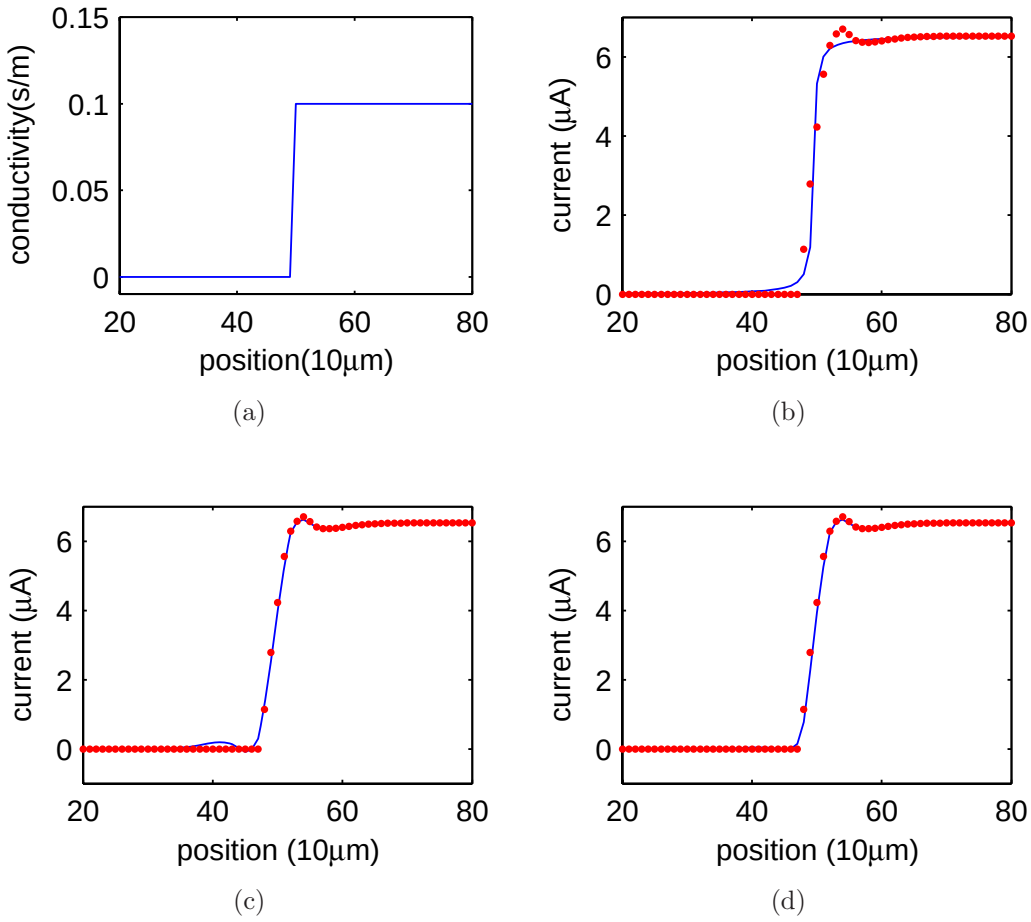

Figure 6.7: (a) is the conductivity profile along the direction; (b), (c), (d) are simulations using the simplified linear, RP, and MLA models respectively (solid curves), compared to the 3-D FDM model (points).

the simple models and the more exact numerical solution. While these models give reasonable qualitative fits to the rising edge of the data, it is clear that the MLA method is the only simplified model that fits well to both ends of the abrupt change. The ability to fit such an abrupt change in conductivity gives confidence in the use of the MLA model for the forward calculation step in real SII inverse problem. In the following sections, the image reconstruction based on the MLA model will be discussed.

6.5 Image reconstruction for SII using MLA

As mentioned above, the SL model is a relative-valued model for SII while the RP and MLA models are calibrated ones. Also notice the best correspondence of MLA method shown above. The left part of this chapter will focus on the image reconstruction for SII using MLA method only. Notice that the MLA method is a nonlinear approximation of the solution for the forward problem of SII. Therefore, the nonlinear conjugate gradient method is employed to solve this complex inverse problem and the discretization is also involved.

6.5.1 Equations for inverse problem and regularization

In the inverse problem, the current through the tip is measured at every scan position; the conductivity distribution is unknown and must be determined. The framework is same as shown in Figure 6.1 except for solving the forward problem using MLA. It is necessary to define a cost functional. In our case, we define the cost functional with a regularization term of total variation as

$$J(\sigma) = ||I(\sigma) - I_{\text{meas}}||^2 + \lambda TV(\sigma) \tag{6.25}$$

where $I(\sigma)$ is the calculated current from the current guess of σ, I_{meas} is the measured current and

$$TV(\sigma) = \int_{\Omega} \sqrt{|\bigtriangledown \sigma|^2 + \zeta^2} dxdy. \tag{6.26}$$

The first term in the cost functional corresponds to the energy norm of the mismatch between the measured currents and the predicted ones, while the second term is the

regularization term of total variation (modified to be differentiable at $\sigma = 0$ by a small constant ζ) with λ selected as a regularization parameter. The solution of the inverse process is to minimize the above cost functional:

$$\hat{\sigma} = \min_{\sigma} J(\sigma). \tag{6.27}$$

The major minimization in the inverse problem is a nonlinear optimization problem. The non-linear conjugate-gradient method is a good choice since it does not require storage of a Hessian matrix which is large. The Polak-Ribiére variant of conjugate-gradient method was used to solve this problem, as it accomplishes the transition to further iterations more gracefully than the conventional conjugate-gradient method. The iterates σ_k, $k \geq 0$ in the conjugate gradient method satisfy the recurrence,

$$\sigma_{k+1} = \sigma_k + \alpha_k d_k$$

where the step-size α_k is positive, and the direction d_k is generated by the rule,

$$d_{k+1} = -g_{k+1} + \beta_k d_k$$

with

$$d_0 = -g_0$$

where $g = \nabla J$, and

$$\beta_k = \frac{\langle g_{k+1} - g_k, g_k \rangle}{||g_k||^2}.$$

Hence, the key part of the inverse process is the evaluation of the function $J(\sigma)$ and the gradient $\nabla J(\sigma)$.

After discretization, $J(\sigma)$ can be calculated as

$$J(\sigma) = \underbrace{\sum_i \left(I_i(\sigma) - I_{\text{meas},i}\right)^2}_{J_I(\sigma)} + \lambda \underbrace{\sum_i \sqrt{|\bigtriangledown \sigma_i|^2 + \zeta^2}}_{J_\sigma(\sigma)}. \tag{6.28}$$

Also, $g(\sigma)$ is the gradient of $J(\sigma)$:

$$\begin{aligned} g(\sigma) &= \frac{\partial J(\sigma)}{\partial \sigma} \\ &= \frac{\partial J_I(\sigma)}{\partial \sigma} + \frac{\partial J_\sigma(\sigma)}{\partial \sigma} \\ &= \sum_i 2\left(I_i(\sigma) - I_{\text{meas},i}\right) \frac{\partial I_i(\sigma)}{\partial \sigma} - \lambda \bigtriangledown \cdot \left(\frac{\bigtriangledown \sigma}{|\bigtriangledown \sigma|}\right). \end{aligned}$$

An expression of I can be derived from Equation (6.24) ,

$$I_i = \sum_h t_{ih}^{k_1} \sigma_h + \sigma_i \sum_h t_{ih}^{k_2} \sigma_h,$$

where $t_{ih}^{k_1}$ and $t_{ih}^{k_2}$ are the $(i,h)^{\text{th}}$ elements of the Toeplitz matrices which implement the convolutions by k_1 and k_2, respectively. Then,

$$\frac{\partial I_i}{\partial \sigma_j} = t_{ij}^{k_1} + \sigma_i t_{ij}^{k_2} + \delta_{ij} \sum_h t_{ih}^{k_2} \sigma_h.$$

Thus, the first term of $g(\sigma)$ in the matrix form becomes

$$\begin{aligned} \frac{\partial J_I(\sigma)}{\partial \sigma} &= 2\frac{\partial I}{\partial \sigma}\left(I(\sigma) - I\right) \\ &= 2\left(T_{k_1}^H + T_{k_2}^H D(\sigma)^* + D\left(T_{k_2}\sigma\right)^*\right)\left(I(\sigma) - I\right). \end{aligned}$$

Meanwhile, $J_\sigma(\sigma)$ is discretized in two dimensional space as follows,

$$J_\sigma(\sigma) = \frac{1}{2}\sum_i\sum_j \Theta\left(\left(D^x_{ij}\sigma\right)^2 + \left(D^y_{ij}\sigma\right)^2\right) \tag{6.29}$$

where $D^x_{ij}\sigma = \frac{f_{ij}-f_{i-1,j}}{\triangle x}$, $D^y_{ij}\sigma = \frac{f_{ij}-f_{i,j-1}}{\triangle y}$ and $\Theta(t) = 2\sqrt{t+\beta^2}$. The gradient of Equation (6.29) is computed as,

$$\frac{\partial J_\sigma(\sigma)}{\partial\sigma} = \sum_i\sum_j \left(D^x_{ij}\left(\Theta'_{ij}D^x_{ij}\sigma\right) + D^y_{ij}\left(\Theta'_{ij}D^y_{ij}\sigma\right)\right)$$

where

$$\begin{aligned}\Theta'_{ij} &= \Theta'\left(\left(D^x_{ij}\sigma\right)^2 + \left(D^y_{ij}\sigma\right)^2\right)\\ &= \frac{1}{\sqrt{\left(D^x_{ij}\sigma\right)^2 + \left(D^y_{ij}\sigma\right)^2 + \beta^2}}.\end{aligned}$$

In matrix form,

$$\frac{\partial J_\sigma(\sigma)}{\partial\sigma} = D_x^T D(\Theta') D_x\sigma + D_y^T D(\Theta') D_y\sigma.$$

Therefore,

$$g(\sigma) = 2\left(T^H_{k_1} + T^H_{k_2}D(\sigma)^* + D(T_{k_2}\sigma)^*\right)(I(\sigma) - I) + \lambda D_x^T D(\Theta') D_x\sigma + D_y^T D(\Theta') D_y\sigma. \tag{6.30}$$

At each iteration, $J(\sigma)$ and $g(\sigma)$ are calculated once and only convolutions and element-multiplication are involved. This results in a huge savings in both CPU time and memory. In addition, because the RP kernel has limited practical spatial support, it can be calculated using a small number of elements in the true FDM model. Then, this convolution kernel can be used to simulate the results from a much larger problem

Table 6.1: Conductivity values of the five circles in the noise-free case. Both mean and standard deviation are shown for each circle.

5 circles (noise free) \ conductivity (S/m)	mean	std
background	0.0998	2.9342e-4
c1 (largest)	0.0069	1.3106e-4
c2	0.0069	3.9025e-5
c3	0.0067	2.1472e-6
c4	0.0069	1.8119e-18
c5 (smallest)	0.0124	0

— one in which the true FDM model may not even be usable due to the size of the problem.

6.5.2 Simulations for 2D image reconstruction

To demonstrate the MLA method and its application to SII, several simulations were performed and analyzed for different configurations. This section starts with two simulations, the first is designed to understand the impact of the reconstruction algorithm on object size, while the second is designed to understand the impact of the reconstruction algorithm on object contrast. In all of the following simulations, the shielded probe is assumed to have a 30 μm tip diameter, a 30 μm gap spacing, and a shield thickness of 30 μm. In addition, the conductivity of the background medium in all simulations is 100 mS/m (close to the conductivity of nutrient solutions). The simulated measurements were generated using the true 3-D FDM model, and the phantoms were homogeneous in the z direction.

Figure 6.8 shows five circles with different sizes in a background medium. The image is scaled so that black corresponds to 0 and white to 110 mS/m. The conductivity of each circle is 6.67 mS/m. There are some obvious blurring effects

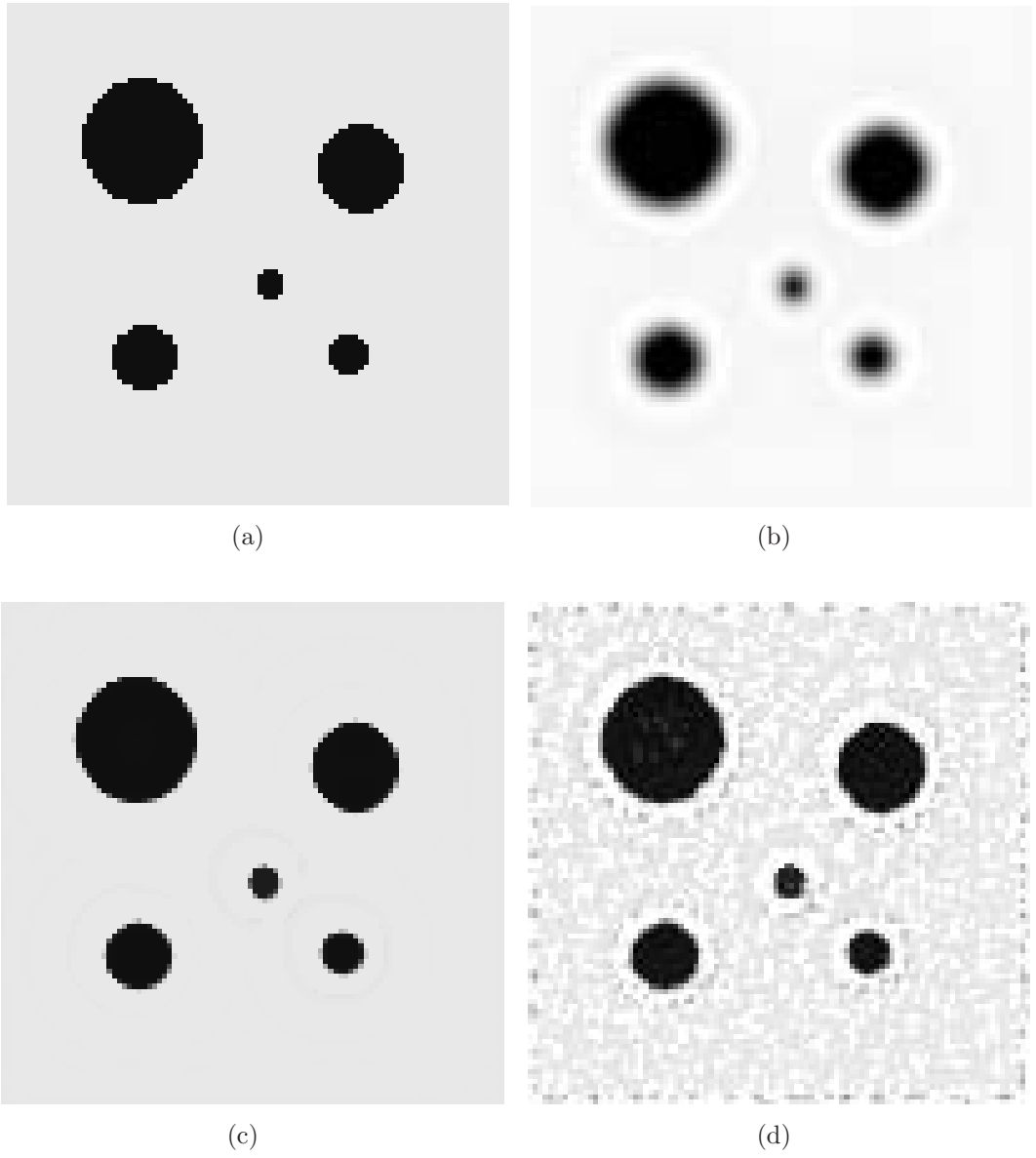

Figure 6.8: Five circles with different sizes in the background medium, pixel size 10μm$\times 10\mu$m, image size 100×100; (a) the conductivity phantom, (b) the simulated measurements using the 3D FDM method, (c) noise-free reconstructed image using the MLA method, (d) MLA-reconstructed image with Gaussian noise (6% of maximum or 24dB SNR).

Table 6.2: Conductivity values of the five circles in the noisy case. Both mean and standard deviation are shown for each circle.

5 circles (noisy) \ conductivity (S/m)	mean	std
background	0.1034	0.0073
c1 (largest)	0.0089	0.0036
c2	0.0083	0.0012
c3	0.0089	9.1716e-4
c4	0.0093	9.4799e-4
c5(smallest)	0.0235	0.0155

in the simulated current measurements shown in Figure 6.8(b). The reconstructed conductivity image shown in Figure 6.8(c) was obtained after 25 iterations of the non-linear conjugate gradient method, using the MLA method for the forward calculation with $\gamma_1 = 0.15$ and $\gamma_2 = 1$. Table 6.1 shows the corresponding conductivity values in both mean and standard deviation. This noise-free result looks almost the same as the original phantom in both value and shape. It shows much clearer edges than the raw data. Clearly, the MLA method is approximating the forward kernel sufficiently to recover additional edge information from the raw data. To see the impact of noise on the reconstruction process, Gaussian noise (with a standard deviation of 6% of the background current value for an SNR of 24dB) was added to the simulated measurements. Figure 6.8(d) shows the reconstruction from these noisy data and Table 6.2 shows the corresponding conductivity values. Despite the high-level of noise, the reconstruction of the five circles is quite good, preserving both the shape and size of the circles. The reconstructed values of the circles and the background medium are also preserved except for artifacts that are likely caused by the total variation algorithm trying to preserve flat regions.

The next simulation experiment is designed to show how using the MLA method affects the recovery of the conductivity values themselves. Figure 6.9(a)

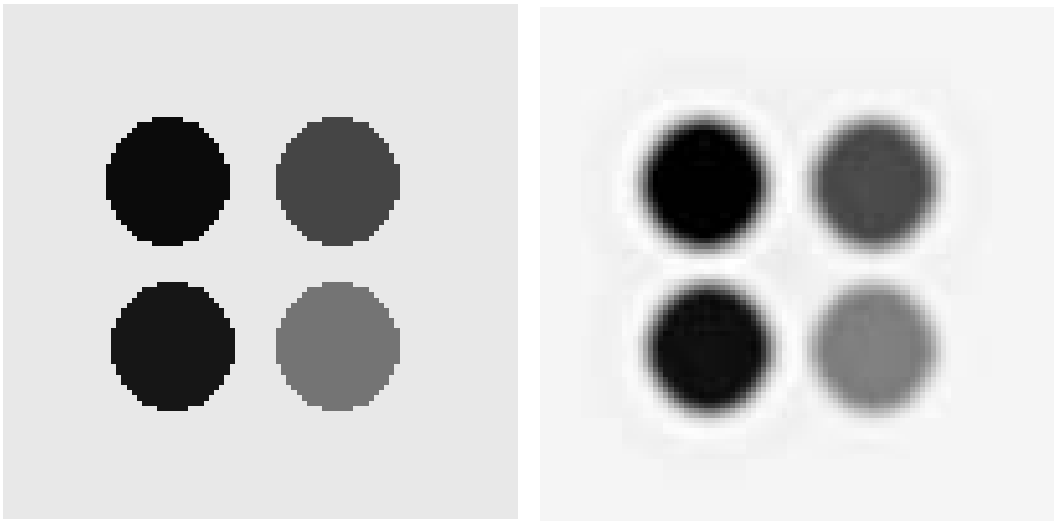

(a)

(b)

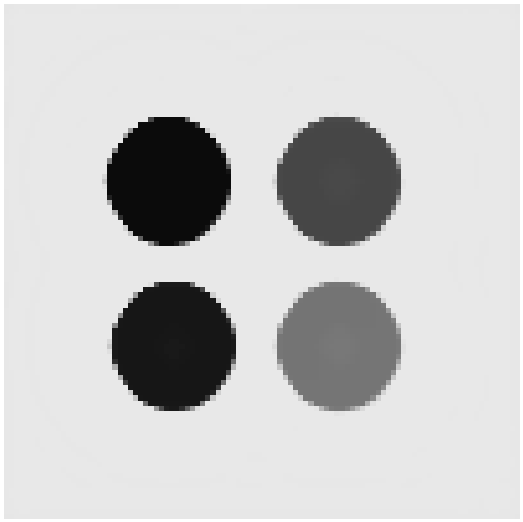

(c)

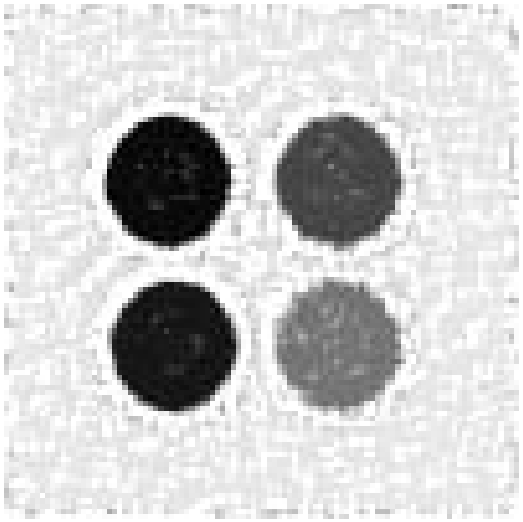

(d)

Figure 6.9: Four circles with different conductivities in the background medium, pixel size 10μm$\times 10\mu$m, image size 100×100; (a) the conductivity phantom, (b) the measured current map, (c) the reconstructed image using the MLA method, (d) the reconstructed image using the MLA method with Gaussian noise (6% of maximum or 24dB SNR).

Table 6.3: Conductivity values of the four circles in the noise-free case. Both mean and standard deviation are shown for each circle.

4 circles (noise free) \ conductivity (S/m)	mean	std
background	0.998	1.8973e-4
c1 (lowest)	0.0052	1.2263e-4
c2	0.0103	2.2096e-4
c3	0.0306	4.5191e-4
c4 (highest)	0.0505	5.1585e-4

Table 6.4: Conductivity values of the four circles in the noisy case. Both mean and standard deviation are shown for each circle.

4 circles (noisy) \ conductivity (S/m)	mean	std
background	0.1033	0.0070
c1 (lowest)	0.0075	0.0051
c2	0.0118	0.0042
c3	0.0323	0.0043
c4 (highest)	0.0532	0.0054

shows four circles with different conductivities (5, 10, 30, and 50 mS/m) were embedded in a background of 100 mS/m. The current "measurements" simulated using the full 3-D FDM model are shown in Figure 6.9(b). The reconstructed conductivity images using the MLA-method for the forward problem with $\gamma_1 = 0.15$ and $\gamma_2 = 1$ are shown in Figures 6.9(c) and 6.9(d) for noise-free and noisy (24dB) data respectively while Tables 6.3 and 6.4 show the corresponding conductivity values. The results show that in both shape and value, both reconstructed images are nearly the same as the original phantom. The noisy reconstructions do show artifacts due to the noise and the total-variation method of regularization. Of central significance, however, is the ability of the inverse problem to converge to a resolution-enhanced solution in 2-3 minutes because of the use of the fast non-linear MLA method in the forward problem.

6.5.3 Experimental data reconstruction

Given the success on simulated data, the MLA method was applied to the inverse problem of recovering conductivity of biological samples from current measurements. Two experiments with biological tissues were performed using the SII system. The system is described in Chapter 3 and is specified here. A Newmark System Model NLS4-4-16 XYZ was used as a stage controller to move the probe for scanning horizontally at increments of 10μm. A 2.5 Volt peak to peak, 10kHz AC signal generated by a programmable frequency generators (Agilent 3520A) was applied to the shield directly and drove the tip through a 27kΩ resistor. A DSP lock-in amplifier (EG&G Instruments Model 7265) or a FFT spectrum analyzer (Stanford Research Systems Model SR760) collected the voltage across the resistor, which is proportional to the current through the tip. The experiments of the breast-cancer cells and the first butterfly wing shown in Figure 6.11 (a) were performed using the main setup of SII with the resistor R while the second butterfly wing shown in Figure 6.11 (b) was measured using the alternative setup with the spectrum analyzer.

The breast-cancer cells were immersed in a cell nutrient solution that had a higher conductivity than the cells. The conducting plane was an aluminum wafer. A shielded probe (D =30 μm, S_p =30 μm, 30 μm shield thickness) was suspended approximately 100 μm above the wafer. The cells were precipitated for a couple of hours so that they touched the conducting plane. A scan was performed to generate a 2-D image of the voltage across the resistor, from which a current map was obtained. The scanning step-size was 10μm, and the image size was 100×100. Similarly, the butterfly wings as shown in Figure 6.11 were taped down to the conducting plane which was also an aluminum wafer. A shielded probe (D =100μm, S_p =100μm, 100

μm shield thickness) was suspended as close to the sample as possible. 2-D images with 25.4 μm scanning step-size were obtained. The image sizes of the butterfly wings shown in Figure 6.11 (a) and (b) are 200×200 and 300×300 respectively.

Figure 6.10, 6.12 and 6.13 show the experimental measurements along with the reconstructed images using the MLA method with $\gamma_1 = 0.15$ and $\gamma_2 = 0.8$ for the breast-cancer cell groups and the pieces of butterfly wings. By comparing the reconstructed images to the original measurements, it can be observed that more details are revealed and the image resolution is improved in the reconstructed images. In both reconstructed images, high frequency components are very clear and edges are much sharper. There is also evidence of artifact, however, in the reconstructed images such as the "halos" around the cell groups and the artistic-appearance of the reconstructed butterfly wings. These experiments confirm that the MLA method can be used to explain the data reasonably well for real biological samples.

6.5.4 Convergence and algorithm evaluation

All the kernel evaluations of the above simulations and experiments were obtained by a FORTRAN program running on an IBM 1350 Linux cluster. The reconstruction algorithm was coded in MATLAB running on a P4 2.8 GHz desktop computer. Figure 6.14 shows the values of the cost functional vs. the number of iterations for image reconstruction in all the simulations and experiments. Fast convergence can be observed in all four cases and the slowest convergence occurs in the butterfly wing cases. This could be due to the large image sizes of the butterfly wings. For both the CPU time and memory, the reconstruction of the butterfly wing images also result in the most computational cost for the same reason. Comparing to the

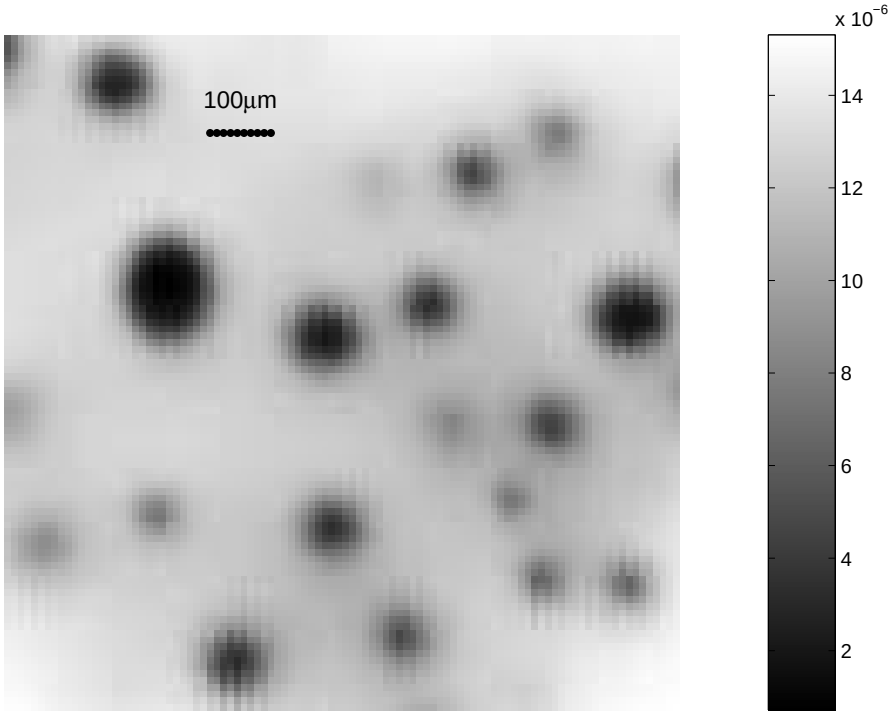

(a)

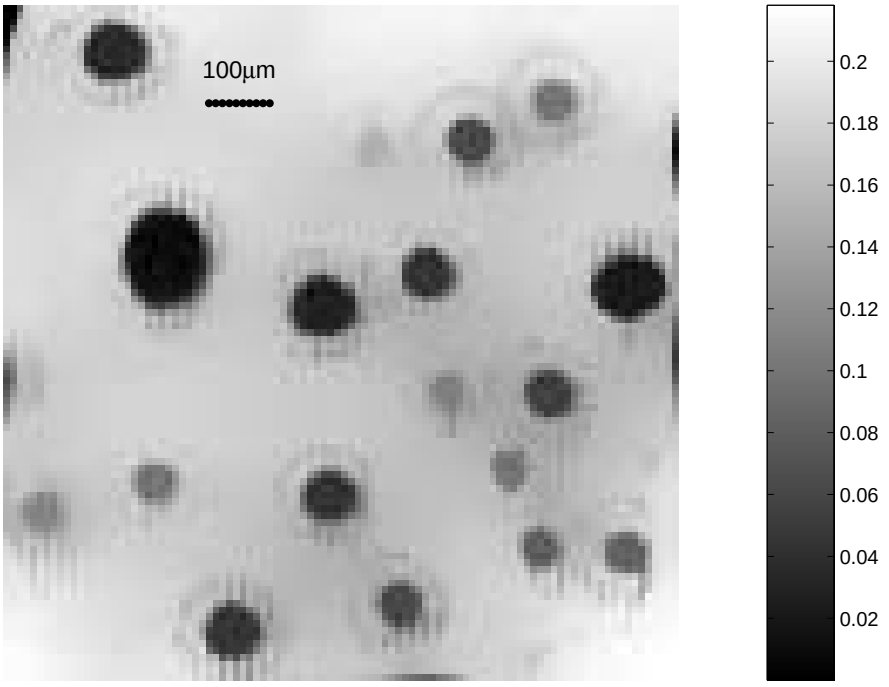

(b)

Figure 6.10: Breast cancer cells, pixel size 10μm$\times 10\mu$m, image size 1.0mm$\times$1.0mm. (a), the measured current map; (b), the reconstructed images

Figure 6.11: digital photos of two pieces of different butterfly wings

conventional inverse method using a true 3-D forward model, the MLA method is much faster and therefore capable of processing a large image in a reasonable amount of time.

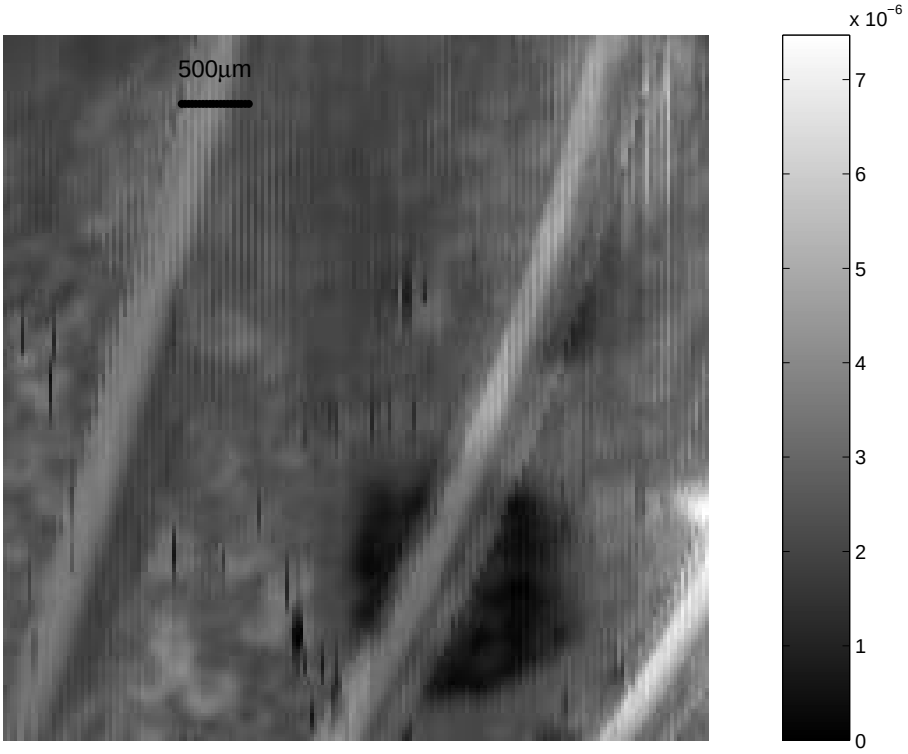

(a)

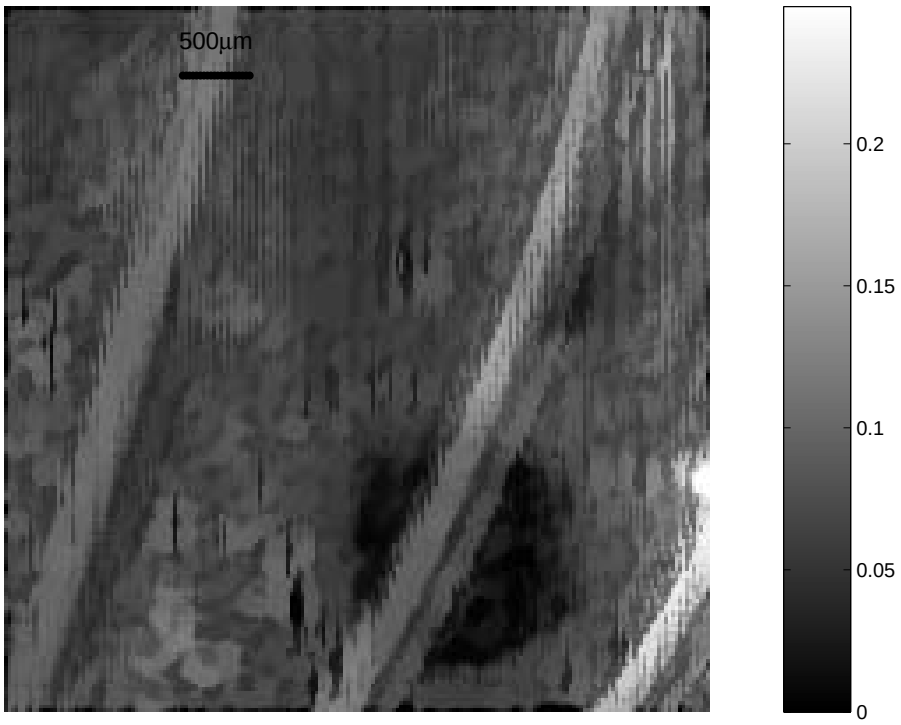

(b)

Figure 6.12: A piece of the butterfly wing shown in Figure 6.11 (a), pixel size 25.4μm$\times 25.4\mu$m, image size 5.08mm$\times$5.08mm. (a), the measured current map; (b), the reconstructed conductivity images

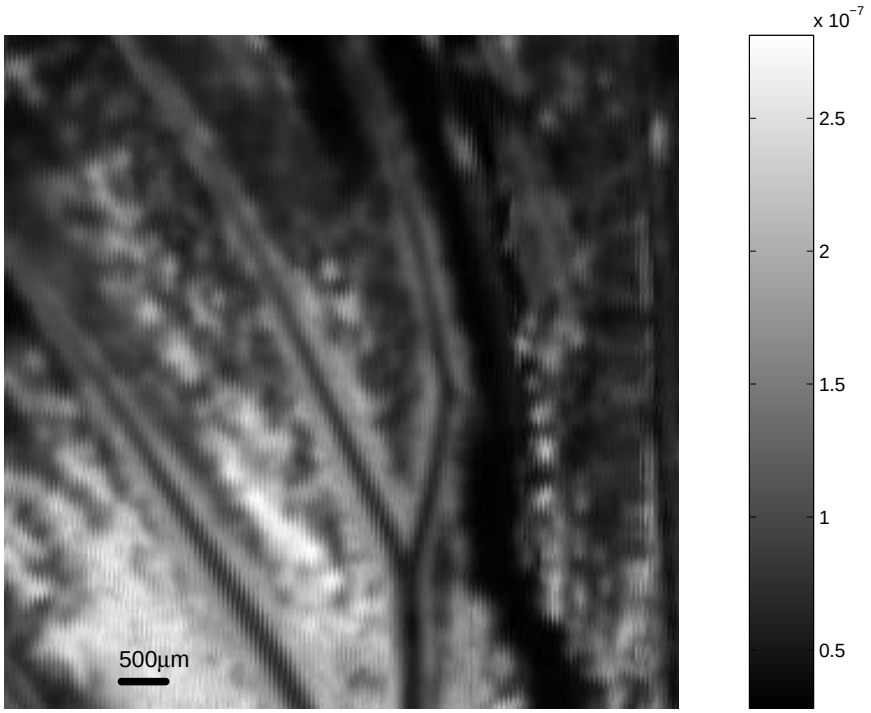

(a)

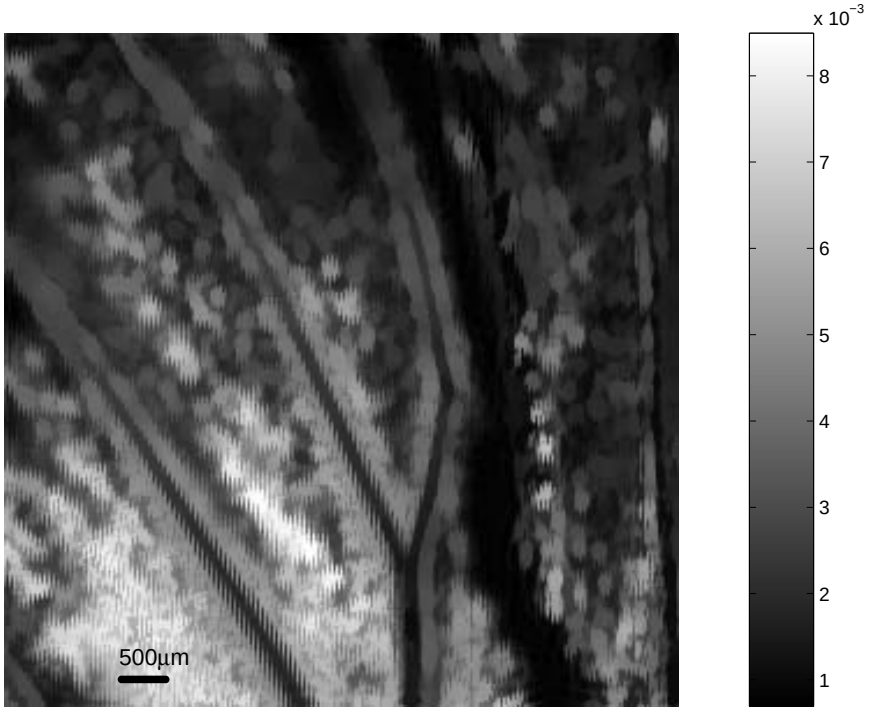

(b)

Figure 6.13: A piece of the butterfly wing shown in Figure 6.11 (b), pixel size 25.4μm$\times 25.4\mu$m, image size 7.62mm$\times$7.62mm. (a), the measured current map; (b), the reconstructed conductivity images

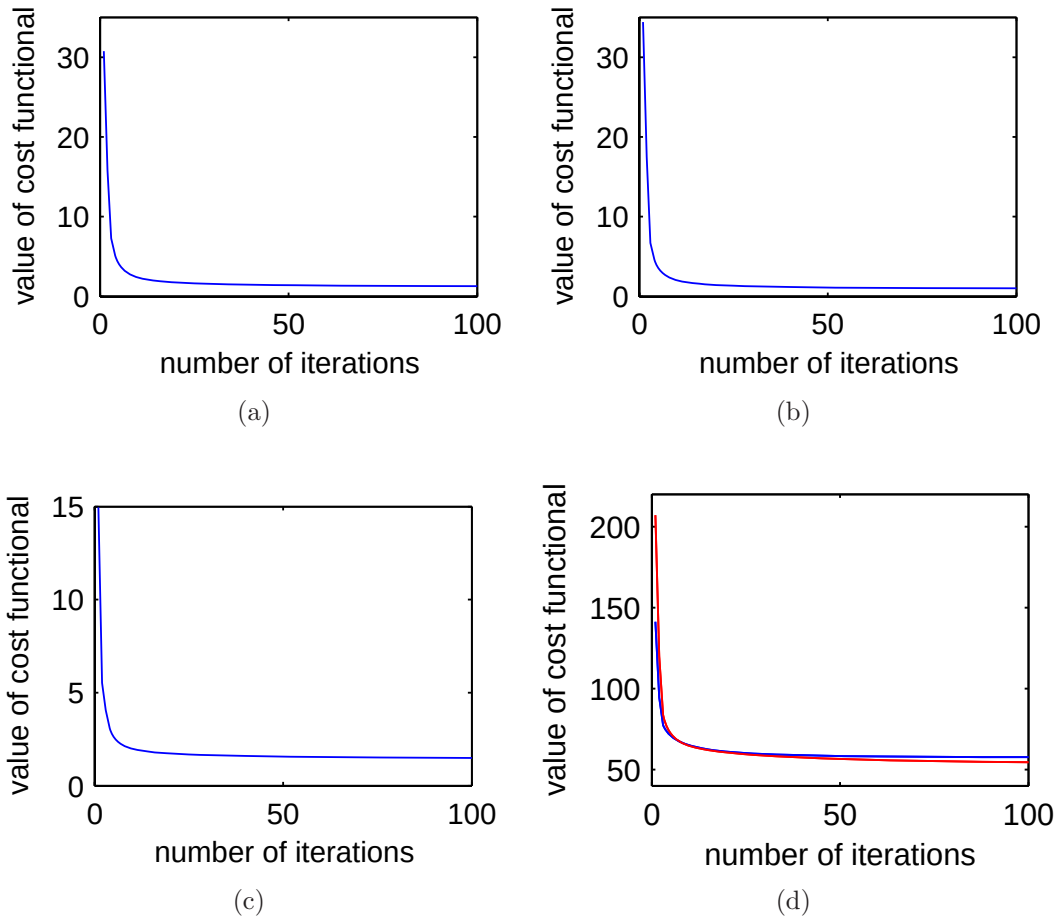

Figure 6.14: Cost functional value vs. number of iterations for (a) five circles; (b) four circles; (c) breast-cancer cells; (d) blue curve for the butterfly wing (a) and red curve for the butterfly wing (b).

6.6 Summary

In this chapter, fast linear and non-linear models based on reasonable assumptions have been developed to approximate the solution of the forward problem in scanning impedance imaging. The approaches use simple explicit formula to approximate the complicated relationship between measured current and conductivity. The models can accurately predict the relationship between conductivity and current so that the inverse problem of conductivity recovery from current does not require the

use of a true 3-D forward numerical solver in the inverse iterations. The savings in computational cost is significant and allows an inverse problem that would normally take about 5 months to be completed in 5 minutes. Among them, the MLA model has demonstrate the best correspondence under same conditions. The image reconstruction based on the MLA model was verified for accuracy and speed on simulated data and then used to reconstruct conductivity images of biological tissues. The results indicated that the MLA method can help improve the resolution and provide a calibrated image of the conductivity distribution. The broader significance of this work is showing how a scanning approach can be used to increase the number of measurements (instead of increasing the number of probes) without losing the ability to recover conductivity. It would potentially be significant to extend this principle to additional scanning geometries such as those that may be encountered in standard electrical impedance tomography.

Chapter 7

Conclusions

7.1 Discussion

The objective of this thesis was to provide a systematic and practical approach that can image the electrical impedance information of small and thin biological slices. A feasible method that could potentially be applied to cellular level measurements called scanning impedance imaging (SII) was developed and implemented. This novel method improves the low resolution of electrical impedance imaging by using high resolution scanning techniques. The aqueous solution used in this method provides a way of indirect contact that both eliminates the complex contact impedance and allows non-destructive measurements under scanning. The new shielded design of the probe eliminates both the effects of the current flux from the region not directly under the end of the probe and the noise generated by the entire conducting plane therefore resulting in higher resolution and higher signal-to-noise ratio. Two hardware setups were designed and implemented. Efforts in scaling down the probe size have also been shown.

A numerical model for the SII system based on a finite difference method has been developed on supercomputer. Important parameters of the hardware configuration: height Z_0, shield spacing S_p and resistor R, have been considered and simulated using this model. The corresponding system performances, including the resolution and the signal-to-noise ratio, have been analyzed. The results have demonstrated that this model can explain experimental data at different probe heights. These results also indicate that the best image resolutions can be achieved when the probe is as close as possible to the sample. Useful predictions have also been obtained using this model. The resistor, R, does not affect the resolution and the shield spacing controls the trade-off between the resolution and the signal-to-noise ratio. This model is useful for understanding the physics of SII and is critical to the development of fast image reconstruction.

The significance of SII is the high resolution achieved by using a scanning technique. Conventional electrical impedance imaging, especially EIT, is limited by the low resolution. In order to increase the resolution, the most common approach is to increase the number of independent measurements. Conventional methods focus on increasing the number of electrodes which has limitations due to the fabrication of electrodes and the interference noise between electrodes. On the other hand, SII uses motion (scanning) to increase the number of measurements instead of increasing the number of electrodes. There are at least two major advantages: a much more accurate and complicated probe (electrode) can be built because only one probe is used, and many more measurements can be achieved without consideration of size and interference of electrodes. However, one drawback is also obvious. The boundary conditions change each time the probe moves. Hence, for one configuration of boundary condition only one measurement can be obtained. The forward problem

of image reconstruction requires many solutions of the numerical FDM model. Thus, image reconstruction for SII is a much more complicated inverse problem.

Two approaches have been developed in this thesis to solve this very complicated inverse problem. The first one focused on quantifying the electrical impedance value from the measurements and ignoring the blurring effects occurred in SII due to the fact that the shield design confines the current flux. A combined value ρh was used to report the resistivity in SII scans. Scans of SU8 test structures showed ρh values that scale with heights as expected. Two other scans were also shown of oxide structures on silicon and a butterfly wing. The ability to quantify resistivity with this system provides a new tool for classifying material properties and imaging a variety of samples.

The second approach considered this complicated inverse problem in another way. Not only the quantification but also the blurring effect were solved under some reasonable assumptions. Two groups of approximation models were developed to replace the true numerical FDM model used as the forward solver in the inverse problem. When the assumptions are valid, these models could approximate the complex relationship between measured current and conductivity using simple explicit formulas. Model verification has been achieved by comparing a simulated line-scan with the true 3-D forward model under same conditions with a known conductivity distribution for all models. Among them, MLA has shown the best fit to the true numerical model and experimental data. An approach of image reconstruction for SII was developed using the MLA model as the forward solver. Due to the non-linearity of MLA, the non-linear conjugate gradient method was employed in the image reconstruction. Simulation results demonstrate the efficiency and the accuracy of this

inverse method for the SII system. Two-dimensional images of butterfly wings and cells were also obtained using the SII system and reconstructed using the MLA image reconstruction. The results showed that the MLA image reconstruction could help improve the resolution and calibrate the conductivity value from the measurements. The savings in computational costs including CPU time and memory are significant. The CPU time reduces from 5 months to 5 minutes and larger images can be processed due to the small memory occupation.

It is significant because these two approaches provide a practical way for image reconstruction of SII. The broader significance of this work is the feasibility of improving resolution using motion. The idea and method in this thesis could be applied to EIT and other modalities.

7.2 Future work

The ultimate goal of SII is to seek high resolution image of electrical impedance of cells or a single cell. The current experimental setup is not capable of this demand and future work is needed. The bottleneck of the current work is the resolution of hardware. The numerical FDM model and the MLA image reconstruction have shown that the reconstructed image resolution is limited by the size of the probe and the scanning step size. One possibility for future work is to fabricate the whole system on a chip and improve the micro-probe introduced in Chapter 3. A higher resolution scanning control system would then be needed. Thus, the whole system would be shrunk down to cellular size which then has the capability of imaging cellular impedance. The successful expansion of SII to cellular imaging would lead to a new imaging tool that would greatly expand the information scientists can obtain

about cellular structure and function. By providing rapid two-dimensional information regarding the conductivity and permittivity of cell samples, greatly improved understanding of cellular processes could be obtained. For example, a high-resolution conductivity image could show the direction and orientation of nano-tubes used for intra-cellular trafficking as well as average activity of ion channels in the cell membrane.

Another improvement of SII in the future could be the reconstruction of a 3D conductivity distribution rather than 2D-only. In this thesis, the sample under measurement has to be thin and flat. If more measurements could be obtained for the z direction, 3D reconstruction of the conductivity distribution could be possible. The system design involved in this thesis may not be suitable for 3D scanning, and the fast image reconstruction ignores changes of conductivity in the z direction. Thus, the system design and the image reconstruction must be expanded.

Another possibility for future work is to increase the frequency. In high frequency range, the effects of the permittivity of the sample could be comparable to the conductivity. This could be especially significant for imaging cells. Much more information of proteins and ion concentrations could be revealed and could be vital to understanding the cell function. For example, an image of permittivity could show protein folding activity as well as reveal the average rotational mobility of water molecules in different regions of the cell during different physiological processes.

In addition, future work in using motion to increase the number of measurements could focus on expanding the idea of the fast image reconstruction in this thesis to other imaging modalities. For example, current EIT uses a ring of electrodes to increase the number of measurements and then improve the image resolution. One

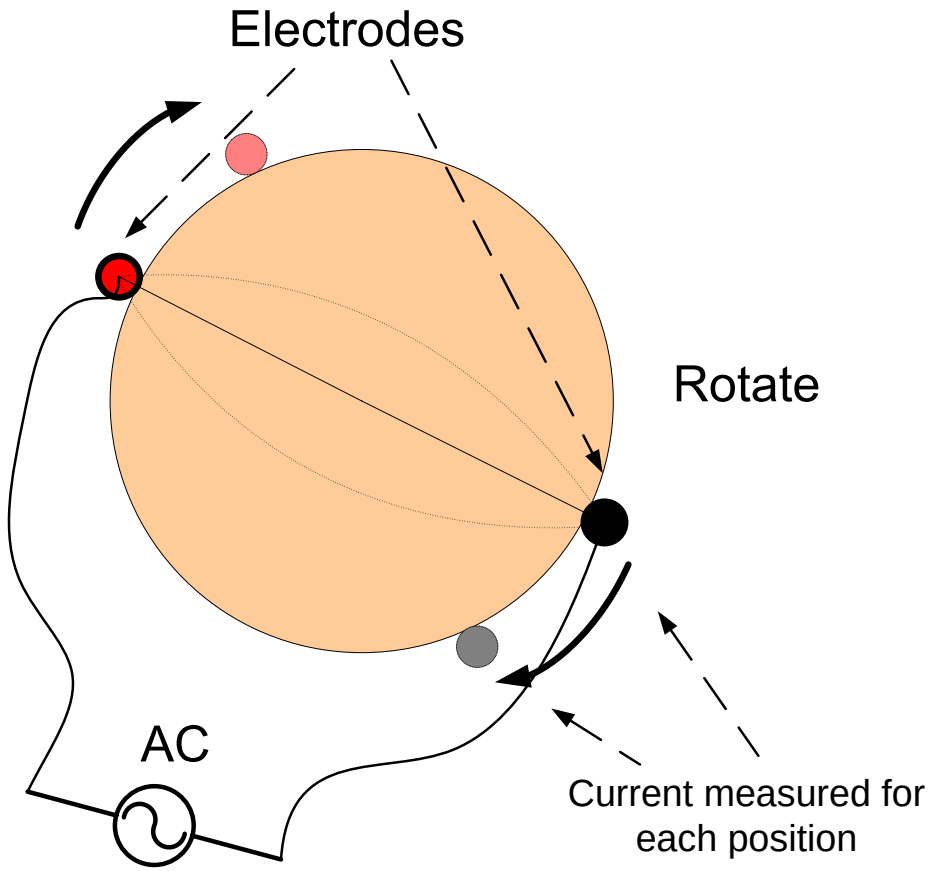

Figure 7.1: Diagram of an improved EIT system. It uses rotation to replace most of the electrodes.

possible solution is to use only two electrodes and rotate them along the surface of the sample. Figure 7.1 shows this idea clearly. A pair of probes is placed opposite each other with a sample at the center. A conductive medium surrounds the probes and the sample. A voltage is applied to the pair of probes and the current through them is measured. The distinction of this innovative design is the rotation of the probes that can produce rings of measurements similar to the classical EIT system. This idea demonstrates at least two advantages. First, there are only two probes instead of 32 or 128 probes, which dramatically reduces the difficulty of the instrumental construction so that micro-scale measurements can be taken. Second, the amount of measurements only depends on the rotation speed and the sampling rate. Thus,

adequate measurements can be obtained by decelerating the rotate speed, increasing the sampling rate, or both. The idea of the MLA image reconstruction can be applied to this rotation system though the motion involved is different from that in SII. Due to the rotation, convolution is not applicable, however, circular convolution could be useful in this case. If a fast image reconstruction based on an idea similar to MLA in SII could be developed for this system, the low resolution of current EIT system could be improved dramatically. A similar idea could also be applied in other imaging modalities.

Bibliography

[1] F. Lacy, M. Kadima-Nzuji, F. J. Malveaux, and E. L. Carter, "Distinguishing between activated and non-activated eosinophils by ac impedance measurements," *IEEE Transactions on Biomedical Engineering*, vol. 43, no. 2, February 1996.

[2] A. R. Hawkins, H. Liu, T. E. Oliphant, and S. M. Shultz, "Non-contact scanning impedance imaging in an aqueous solution," *Applied Physics Letters*, vol. 85, no. 5, pp. 1080–1082, August 2004.

[3] H. Liu, A. R. Hawkins, S. M. Shultz, and T. E. Oliphant, "Non-contact scanning electrical impedance imaging," *Proceedings of the 26th Annual International Conference of the IEEE Engineering in Medicine and Biology Society*, September 2004.

[4] B. C. Green, T. Shang, J. C. Morine, H. Liu, S. M. Shultz, T. E. Oliphant, and A. R. Hawkins, "Resolution scaling in noncontact scanning impedance imaging," *Review of Scientific Instruments*, vol. 75, pp. 4610–4614, 2004.

[5] H. Liu, A. Hawkins, S. M. Shultz, and T. E. Oliphant, "Microscopic impedance imaging of small tissues," *Proceedings of the 2006 IEEE International Symposium on Biomedical Imaging: From Nano to Macro*, April 2006.

[6] T. E. Oliphant, H. Liu, A. R. Hawkins, and S. M. Shultz, "Simple linear models of scanning impedance imaging for image reconstruction of relative conductivity of biological samples," *IEEE Transactions on Biomedical Engineering*, vol. 53, pp. 2323–2332, 2006.

[7] H. Liu, A. R. Hawkins, S. Shultz, and T. E. Oliphant, "Modelling for scanning impedance imaging," *Proceedings of the 27th Annual International Conference of the IEEE Engineering in Medicine and Biology Society*, September 2005.

[8] H. Liu, A. R. Hawkins, S. M. Shultz, and T. E. Oliphant, "Verification and application of a finite-difference model for quasi-electrostatic scanning impedance imaging," *Journal of Electrostatics*, 2006.

[9] B. G. Buss, D. N. Evans, H. Liu, T. Shang, T. E. Oliphant, S. M. Shultz, and A. R. Hawkins, "Quantifying resistivity using scanning impedance imaging," *Sensors and Actuators: A. Physical*, 2007.

[10] H. Liu, A. Hawkins, S. Shultz, and T. E. Oliphant, "A fast linear reconstruction method for scanning impedance imaging," *Proceedings of the 28th Annual International Conference of the IEEE Engineering in Medicine and Biology Society*, September 2006.

[11] H. Liu, A. R. Hawkins, S. M. Shultz, and T. E. Oliphant, "Fast non-linear image reconstruction for scanning impedance imaging," *IEEE Transactions on Biomedical Engineering*, 2007.

[12] G. G. Matthews, *Cellular Physiology of Nerve and Muscle*, 2nd ed. Blackwell Scientific, 1994.

[13] M. J. Allen, "Atomic force microscopy: A new way to look at chromatin," *IEEE Engineering in Medicine and Biology Magazine*, vol. 16, pp. 34–41, 1997.

[14] L. Udpa, V. M. Ayres, Y. Fan, Q. Chen, and S. A. Kumar, "Deconvolution of atomic force microscopy data for cellular and molecular imaging," *IEEE Signal Processing Magazine*, vol. 23, pp. 73–83, 2006.

[15] G. Galeotti, "Uber die elektrische leitfahigkeit der tierschen gewebe," *Z. Biol.*, vol. 43, pp. 289–340, 1902.

[16] L. A. Geddes and L. E. Baker, "The specific resistance of biological material – a compendium of data for the biomedical engineer and physilogist," *Med. and biol. Engng.*, vol. 5, pp. 271–293, 1967.

[17] A. J. Surowiec, S. S. Stuchly, and et al., "Dielectric properties of breast carcinoma and the surrounding tissues," *IEEE Transactions on Biomedical Engineering*, vol. 35, pp. 257–263, 1988.

[18] F. C. Grant, "Localisation of brain tumours by determination of the electrical resistance of the growth," *Journal of the American Medical Association*, vol. 81, pp. 2166–2169, 1923.

[19] L. L. Hause, T. A. Komorowski, and F. Gayon, "Electrode and electrolyte impedance in the detection of bacterial growth," *IEEE Transaction on Biomedical Engineering*, vol. 28, pp. 403–410, 1981.

[20] I. Giaever and C. R. Keese, "Monitoring fibroblast behavior in tissue culture with and applied electrc field," *Proc. Natl. Acad. Sci.*, vol. 81, pp. 3761–3764, 1984.

[21] P. Mitra, C. R. Keese, and I. Giaever, "Electrical measurements can be used to monitor the attachment and spreading of cells in tissue culture," *Biotechniques*, vol. 11, pp. 504–510, 1991.

[22] I. Giaever and C. R. Keese, "Micromotion of mammalian cells measured electrically," *Proc. Natl. Acad. Sci.*, vol. 88, pp. 7896–7900, 1991.

[23] R. Hagedorn, L. Z. Konstanze, E. Richter, J. Hornung, and A. Voigt, "Characterization of cell movement by impedance measurements on fibroblasts grown on perforated si-membranes," *Biochemica et Biophysica Acta - Molecular Cell Research*, vol. 1269, pp. 221–232, 1995.

[24] J. Wegener, M. Sieber, and H. J. Galla, "Impedance analysis of epithelial and endothelial cell monolayers cultured on gold surfaces," *J. Biochem. Biophys. Methods*, vol. 32, pp. 151–170, 1996.

[25] R. Ehret, W. Baumann, M. Brischwein, A. Schwinde, K. Stegbauer, and B. Wolf, "Monitoring of cellular behaviour by impedance measurements on iterdigitated electrode structures," *Biosensors and Bioelectronics*, vol. 12, pp. 29–41, 1997.

[26] R. P. Henderson and J. G. Webster, "An impedance camera for spatially specific measurements of the thorax," *IEEE Transactions on Biomedical Engineering*, vol. 25, no. 3, 1978.

[27] D. C. Barber, B. Brown, and I. L. Freeston, "Imaging spatial distribution of resistivity using applied potential tomography," *Electronic Letters*, vol. 19, pp. 933–935, 1983.

[28] B. H. Brown and A. D. Seagar, "The sheffield data collection system," *Clinical Physi. Physiol. Meas.*, vol. 8, pp. A:9 1–97, 1987.

[29] D. G. Gisser, D. Isaacson, and J. C. Newell, "Theory and performance of an adaptive current tomography system," *Clinical Physi. Physiol. Meas.*, vol. 9, pp. 35–41, 1988.

[30] R. D. Cook, G. J. Saulnier, D. G. Gisser, J. C. Goble, J. C. Newell, and D. Isaacson, "Act3: A high-speed, high-precision electrical impedance tomography," *IEEE Trans. Biomed. Eng.*, vol. 41, pp. 713–722, 1994.

[31] D. Isaacson, "Distinguishability of conductivity by electric current computed tomography," *IEEE Trans. Med. Imaging*, vol. 5, pp. 91–95, 1986.

[32] M. Chency and D. Isaacson, "Distingushability in impedance imaging," *IEEE Trans. Biomed. Eng.*, vol. 39, pp. 852–860, 1992.

[33] K. S. Cheng, D. Isaacson, J. C. Newell, and D. G. Gisser, "Electrode models for electric current computed tomography," *IEEE Trans. Biomed. Eng.*, vol. 36, pp. 918–924, 1989.

[34] Y. Z. Ider and O. Birgul, "Use of the magnetic field generated by the internal distribution of injected currents for electrical impedance tomography (mr-eit)," *ELEKTRIK*, vol. 6, no. 3, pp. 215–225, 1998.

[35] O. Kwon, E. J. Woo, J. R. Yoon, and J. K. Seo, "Magnetic resonance electrical impedance tomography (mreit): Simulation study of the j-subsitution algorithm," *IEEE Transactions on Biomedical Engineering*, vol. 49, pp. 160–167, 2002.

[36] S. Al-Zeibak and N. H. Saunders, "A feasiblity study of in vivo electromagnetic imaging," *Phys. Med. Biol.*, vol. 38, pp. 151–60, 1993.

[37] R. Shao, S. V. Kalinin, and D. A. Bonnell, "Local impedance imaging using spectroscopy of polycrystalline zno using contact atomic force microscopy," *Applied Physics Letters*, vol. 82, no. 12, pp. 1869–1871, March 2003.

[38] A. D. Seagar, D. C. Barber, and B. H. Brown, "Theoretical limits to sensitivity and resolution in impedance imaging," *Clinical Physics and Physiological Measurement*, vol. 8, pp. A13–A31, 1987.

[39] J. G. Webster, *Electrical Impedance Tomography*, Bistol, England: Adam Hilger, 1990.

[40] A. V. Korjenevsky, V. N. Kornienko, M. Y. Kultiansov, and V. A. Cherepenin, "Electrical impedance computerized tomography for medical applications," *Instruments and Experimental Techniques*, vol. 40, pp. 415–421, 1997.

[41] M. Bertero and P. Boccacci, *Introduction to inverse problem in imaging.* London: Institute of Physics Publishing, 1998.

[42] P. C. Hansen, *Rank-Deficient and Discrete Ill-posed Problems: Numerical Aspects of Linear Inversion.* SIAM Pub, 1998.

[43] L. I. Rudin, S. Osher, and E. Fatemi, "Nonlinear total variation based noise removal algorithms," *Proceeding of the 11th Annual International Conference of the center for Nonlinear Studies, Physica D*, vol. 60, pp. 259–268, 1992.

[44] D. Barber, "A review of image reconstruction for electrical impedance tomography," *Med. Phys.*, vol. 16, pp. 162–169, 1989.

[45] J. L. Mueller, S. Siltanen, and D. Isaacson, "A direct reconstruction algorithm for electrical impedance tomograhpy," *IEEE Transaction on Medical Imaging*, vol. 21, pp. 555–559, 2002.

[46] R. P. Henderson, J. G. Webster, and D. K. Swanson, "A thoracic electrical impedance camera," *Proc. Annul. Conf. Engineering in Medicine and Biology*, vol. 18, p. 322, 1976.

[47] J. Jossinet, E. Marry, and A. Montalibet, "Electrical impedance endotomograhpy: imaging tissue from inside," *IEEE Trans. on Med. Imaging*, vol. 21, no. 6, 2002.

[48] D. C. Barber, B. H. Brown, and N. J. Avis, "Image reconstruction in electrical impedance tomography using filtered back projection," *Proc. Annu. Int. Conf. IEEE Engineering in Medicne and Biology Soc.*, pp. 1691–1692, 1992.

[49] F. Santosa and M. Vogelius, "A backprojection algorithm for electrical impedance imaging," *SIAM J. Appl. Math.*, vol. 50, pp. 216–243, 1990.

[50] G. Beylkin, "The inversion problem and applications of the generalized radon transform," *Commun. Pure Appl. Math*, vol. 37, pp. 580–599, 1984.

[51] C. A. Berenstein and T. E. Casadio, "Integral geometry in hyperbolic spaces and electrical impedance tomography," *SIAM J. Appl. Math.*, vol. 56, pp. 755–764, 1996.

[52] M. Cheney and D. Isaacson, "A layer stripping algorithm for impedance imaging," *IEEE-EMBS*, vol. 13, pp. 3–4, 1991.

[53] A. Grunbaum and J. P. Zubelli, "Diffuse tomography: computational aspects o fth eisotropic case," *Inverse Problems*, vol. 8, pp. 421–433, 1992.

[54] J. Sylvester, "A convergent layer stripping algorithm for radially symmetric impedance tomography problem," *Commun. Partial Diff. Eqns*, vol. 17, pp. 1955–1994, 1992.

[55] L. Borcea, "Electrical impedance tomography," *Inverse problems*, vol. 18, pp. 99–136, 2002.

[56] M. Ikehata and S. Siltanen, "Numerical method for finding the convex hull of an inclusion in conductivity from boundary measurements," *Inverse problems*, vol. 16, pp. 1043–1052, 2000.

[57] A. Kirsch, "Characterization of the shape of the scattering obstacle using the spectral data of the far field operator," *Inverse problems*, vol. 14, pp. 1489–1512, 1998.

[58] R. O. Schmidt, "Multiple emitter location and signal parameter estimation," *IEEE Trans. Antennas*, vol. 34, pp. 276–280, 1986.

[59] L. A. Hanoch and A. J. Devaney, "The time reversal technique re-interpreted: sbuspace based signal processing for multi-static target location," *IEEE Sensor Array and Multichannel Signal Processing Workshop*, pp. 509–513, 2000.

[60] D. Cheney, "The linear sampling method and the music algorithm," *Inverse problems*, vol. 17, pp. 591–595, 2001.

[61] O. Dorn, E. L. Miller, and C. M. Rappaport, "A shape reconstruction method for electromagnetic tomography using adjoint fields and level sets," *Inverse problems*, vol. 16, pp. 1118–1156, 2000.

[62] K. Ito, K. Kunisch, and Z. Li, "Level-set function approach to an inverse interface problem," *Inverse problems*, vol. 17, pp. 1225–1242, 2001.

[63] S. J. Osher and F. Santosa, "Level set methods for optimization problems involving geometry and constraints. i. frequencies of a two-density inhomogeneous drum," *J. Comput. Phys.*, vol. 171, pp. 272–288, 2001.

[64] F. Santosa, "A level-set approach for inverse problems involving obstacles," *ESAIM Control Optim. Calc. Var.*, vol. 1, pp. 17–33, 1996.

[65] L. Borcea, "A nonlinear multigrid for imaging electrical conductivity and permittivity at low frequency," *Inverse Problems*, vol. 17, pp. 329–359, 2001.

[66] K. A. Dines and R. J. Lytle, "Analysis of electrical conductivity imaging," *Geophysics*, vol. 46, pp. 1025–1036, 1981.

[67] D. C. Dobson, "Convergence of a reconstruction method for the inverse conductivity problem," *SIAM J. Appl. Math.*, vol. 52, pp. 442–458, 1992.

[68] M. Hanke, "Regularizing properties of a truncated newton-cg algorithm for nonlinear inverse problems," *Numer. Funct. Anal. Optim.*, vol. 18, pp. 971–993, 1997.

[69] T. Murai and Y. Kawaga, "Electrical impedance computed tomography based on a finite element model," *IEEE Transactions on Biomedical Engineering*, vol. 32, pp. 177–184, 1985.

[70] M. Cheney, D. Isaacson, J. Newell, S. Simske, and J. Goble, "Noser: An algorithm for solving the inverse conductivity problem," *International Journal of Imaging Systems and Technology*, vol. 2, pp. 66–75, 1990.

[71] P. M. Edic, G. J. Saulnier, J. C. Newell, and D. Isaacson, "A real-time electrical impedance tomography," *IEEE Trans. Biomed. Eng.*, vol. 42, pp. 849–858, 1995.

[72] J. E. Dennis and R. B. Schnabel, *Numerical Methods for Unconstrained Optimization and Nonlinear Equations*. Philadelphia, PA: SIAM, 1996.

[73] Y. K. et al, "Electrical impedance imaging of the thorax," *Journal of Microwave Power*, vol. 18, pp. 245–257, 1983.

[74] Y. et al, "Comparing reconstruction algorithms for electrical impedance tomography," *IEEE Trans. Biomed. Eng.*, vol. 34, pp. 843–852, 1987.

[75] K. Levenberg, "A method for the solution of certain non-linear problems in least squares," *Quart. Appl. Math.*, vol. 2, pp. 164–168, 1944.

[76] D. Marquardt, "An algorithm for the least squares estimation of nonlinear parameters," *Journal of the Society for Industrial and Applied Mathematics*, vol. 11, pp. 431–441, 1963.

[77] D. Isaacson and P. M. Edic, "An algorithm for impedance imaging," *Proceedings of Annual International Conference of IEEE Engineering in Medicine and Biology Society*, p. 1693, 1992.

[78] A. Wexler, B. Fry, and M. Neumann, "Impedance tomography algorithm and system," *Appl. Optics*, vol. 24, pp. 3985–3992, 1985.

[79] K. Paulson, W. Breckon, and M. Pidcock, "Optimal measurements in electrical impedance tomography," *IEEE-EMBS*, vol. 14, pp. 1730–1731, 1992.

[80] Y. Saad, *Iterative Methods for Sparse Linear Systems*, 2nd ed. Philadelphia: Society for Industrial and Applied Mathematics, 2003, chapter 6-7.

[81] N. LaBianca and J. Delorme, "High aspect ratio resist for thick film applications," 1995.

[82] S. Jiguet, A. Bertsch, H. Hofmann, and P. Renaud, "Conductive su8 photoresist for microfabrication," *Adv. Funct. Mat.*, vol. 15, pp. 1511–1516, 2005.

[83] B. Brandstatter, "Jacobian calculation for electrical impedance tomography based on the reciprocity principle," *Ieee Transactions on Magnetics*, vol. 39, no. 3, May 2003.